1415 N CHERRY AVE
CHICAGO, IL 60642
(312) 281-6900
DMDII.ORG
DMDII@UILABS.ORG

DMDII
a UI LABS Collaboration
DIGITIZING AMERICAN MANUFACTURING

DMDII FINAL PROJECT REPORT

PROJECT TITLE	
Principle Investigator / Email Address	Jian Cao jcao@northwestern.edu
Project Team Lead	Northwestern University
Project Designation	15-07-07-Virtually Guided Certification
UI LABS Contract Number	0220160021
Project Participants	Northern Illinois University, PDA LLC, QuesTek, Siemens
DMDII Funding Value	$1,049, 403.00
Project Team Cost Share	$ 1,097,228.00
Award Date	31 August 2016
Completion Date	31 May 2018

SPONSORSHIP DISCLAIMER STATEMENT: This project was completed under the Cooperative Agreement W31P4Q-14-2-0001, between U.S. Army - Army Contracting Command - Redstone and UI LABS on behalf of the Digital Manufacturing and Design Innovation Institute. Any opinions, findings, and conclusions or recommendations expressed in this material are those of the author(s) and do not necessarily reflect the views of the Department of the Army.

DISTRIBUTION STATEMENT A. Approved for public release; distribution unlimited.

TABLE OF CONTENTS

Page(s)	Section
8	I. Executive Summary (1-2 pages)
9-10	II. Project Overview
10	III. KPI's & Metrics
11-91	IV. Technology Outcomes
92	V. Accessing the Technology
92-93	VI. Industry Impact & Potential
93-94	VII. Tech Transition Plan & Commercialization
94-95	VIII. Workforce Development
95-96	IX. Conclusions/Recommendations
96	X. Lessons Learned
96-108	XI. Appendices

List of Figures

Figure	Page
Figure 1: Foundation of the Verification Framework	9
Figure 2: Digital flow chart for tensile yield strength prediction	12
Figure 3: Submicron corundum oxide particles in the as-deposited LENS PH48S	13
Figure 4: Step diagram of PH48S with the composition Fe-10.9Cr-8.67Ni-7.31Co-1.59Mo-0.61Ti-0.35Al-0.009C-0.013O (in wt.%)	13
Figure 5: The simulated thermal profile (a) for the top center point in the PH48S bar as indicated by the red dot (b).	14
Figure 6: Temperature-dependent interfacial energy between corundum and liquid Fe	14
Figure 7: A comparison of (a) predicted oxide evolution by PrecipiCalc simulation and (b) experimental characterization of as-deposited size.	15
Figure 8: Evolution of prior austenite grain structure during 1200 °C isothermal heat treatment for (a) 1 hour, (b) 2 hours, (c) 12 hours and (d) 24 hours with (e) quantitative	16

analysis.	
Figure 9: The linear relationship between the prior austenite grain size (in the equiaxed regime) and oxide size distribution with the Z value calibrated to be 1.53.	17
Figure 10: Relationship between the prior austenite grain size and the packet size in quenched martensite in the Fe–0.2C and the Fe–0.2C–2Mn alloys [7].	18
Figure 11: Evolution of η phase and B2 phase during ageing at 520 oC in terms of (a) average particle radius, (b) volume fraction and (c) strengthening effect.	20
Figure 12: The tensile yield strength of LENS PH48S tensile bar: (a) predicted; (b) measured.	22
Figure 13: Interpolation of simulated temperature field from unstructured finite element method (FEM) mesh to the voxel structure for the cruciform build.	23
Figure 14: Octree refinement for the cruciform geometry.	24
Figure 15: Temperature field for step-plate at three levels of voxel.	24
Figure 16: overlaying a structured voxel grid on the mesh, tagging the voxel to the FEM element that encompasses it, interpolating the properties based on nodal values.	25
Figure 17: parallelization of the voxel code reduces the computational time.	26
Figure 18: Schematic of work flow of old version of GAMMA preprocessor.	26
Figure 19: Schematic showing inactive element method.	27
Figure 20: Workflow linking GAMMA thermal simulation through ICME software to predict material microstructure and properties.	29
Figure 21: comparison of GAMMA and experimental results for a probe point before calibration.	30
Figure 22: high sensitivity of results toward water convection coefficient, the image on the right shows the relative position of the thermocouples on the substrate.	31
Figure 23: Response surface of the calibration cost function J.	31
Figure 24: Comparing experimental and simulation results for one thermocouple after calibration.	32
Figure 25: Simulation result by assuming that the ambient temperature ramps up.	33
Figure 26: Measured variable ambient temperature during experiment by NIU.	33
Figure 27: Comparing GAMMA results before and after including radiation from side.	34

Figure 28: Front thermocouple temperature history with constant and varying ambient temperatures (GAMMA vs Experiment).	34
Figure 29: Close thermocouple temperature history with constant and varying ambient temperatures (GAMMA vs Experiment).	35
Figure 30: Comparing simulation (red) with experiment (blue) in cruciform experiment.	35
Figure 31: General flow of the process-structure-property relationship.	36
Figure 32: Visualization of DoE samples generated by OLHS in 2D (a) and 3D (b) for the casting process metamodel.	37
Figure 33: Metal investment casting of step plates, provided by PDA.	38
Figure 34: Automatic extraction of solidification cooling rate from casting process simulation data.	39
Figure 35: Locations and labels of the 12 thermocouples on the step plate.	39
Figure 36: MAGMAsoft thermal simulation of the step plate.	40
Figure 37: Selected response surfaces of the casting process metamodels. The response plotted on the Z-axis is the solidification cooling rate (SCR).	41
Figure 38: Sobol indices (y-axis) of four locations on the step plate.	42
Figure 39: Selected response surfaces of the casting homogenization metamodel. The titles show the values of the inputs that were held constant. (X1: secondary dendrite arm spacing; X2: wt%(Ni); X3: wt%(Co); X4: homogenization temperature).	43
Figure 40: As-cast grain structure for step plate (SDAS).	44
Figure 41: Homogenization time prediction using metamodeling and analytical SDAS calculation, directly from MAGMAsoft thermal history results.	44
Figure 42: Predicted solidification cooling rates and required homogenization times for the optimized process conditions.	45
Figure 43: Selected response surfaces of the precipitation strengthening metamodel. The title shows the values of the inputs that were held constant. Please refer to Table 33 for the physics-based names of X1 through X8.	46
Figure 44: Selected response surfaces of the solid solution strengthening metamodel. The title shows the values of the inputs that were held constant. Please refer to Table 33 for the physics-based names of X1 through X8.	47
Figure 45: The final structure-property metamodeling flow to obtain tensile yield strength.	48

Figure 46: Image processing procedure.	49
Figure 47: Image with ring artifacts (a), with voids due to porosity shown in red (b). The image after ring artifacts removal (c).	50
Figure 48: Virtual certification workflow - Training Mode.	53
Figure 49: Virtual certification workflow - Rapid Mode.	54
Figure 50: Process Certification add-on ribbon in NX.	54
Figure 51: Open existing process certification project.	55
Figure 52: Create new process certification project.	55
Figure 53: Step plate test part with base plate.	56
Figure 54: Visualization of additive manufacturing toolpath in NX.	57
Figure 55: Dialog box for toolpath conversion to DMC an example output format.	57
Figure 56: Dialog box for toolpath conversion to GAMMA compatible format.	58
Figure 57: GAMMA compatible mesh generated using NX.	59
Figure 58: Dialog box to collect user input needed to run GAMMA.	60
Figure 59: Dialog box to perform a GAMMA simulation.	61
Figure 60: Options to import GAMMA results.	62
Figure 61: Visualization and exploration of GAMMA results.	62
Figure 62: Dialog box to export thermal data for ICMD computation.	63
Figure 63: Example of thermal history plot for a single location.	64
Figure 64: Dialog box to generate and visualize the OLHS.	65
Figure 65: Native output of the OLHS executable.	65
Figure 66: Example of 2D (left) and 3D (right) visualization of the OLHS results.	66
Figure 67: Dialog box to gather input for the Gaussian Process Model fitting.	66
Figure 68: Native output of the Gaussian Process Modeling executable.	67
Figure 69: Example of visualization of a surrogate model that predicts the logarithm of mean particle radius as a function of the logarithm of the solidification/cooling rate and of the interfacial energy.	67

Figure 70: NX Nastran simulation model with load and constraints.	68
Figure 71: Dialog box to trigger the as-designed simulation.	68
Figure 72: Visualization of the as-designed simulation results.	69
Figure 73: Dialog box to perform the as-manufactured simulation.	70
Figure 74: Example of comparison between as-designed and as-manufactured simulation results.	70
Figure 75: Steps to retrieve the Mesh Collector ID.	71
Figure 76: Sketch of “cruciform” build that will be used for Task 5 for validation and verification all dimensions are in inches	72
Figure 77: View of cruciform build height was ~2” and it took 10 hrs. to build	73
Figure 78: (Top) schematic of “cruciform” and areas section for analysis. (Bottom) representative microstructure from left to right (left) section C-C top curve portion of cruciform, (middle) section B-B straight bottom portion of cruciform, (right) Half Charpy from previous work done in [2].	74
Figure 79: Plot of the input power (W) vs the powder flow/Travel speed ratio as detailed in [2]	75
Figure 80: plot of total build height of 10 layers (bead size ~ 1mm) vs. hatch spacing	76
Figure 81: Multilayer builds (measurements in mm)	77
Figure 82: View of cross sectional area (A-A from Figure 79) of samples in which three regions for measurements were selected (top, middle and bottom) and the locations of each individual reading	77
Figure 83: representative microstructure of 316L with larger bead from left to right (left) bottom of multilayered sample, (middle) middle portion of multilayered sample, (right) top of multilayered sample.	78
Figure 84: Schematic of LENS set up with AE sensor for powder flow and power measurement calorimetric system (PMCS) utilized to monitor net heat input among other things. Deposition head moves in X and Y and build plate moves in Z. Top right is the output data from the power measurement calorimetric system (PMCS) which provides the integrated energy (kJ) as the sample is being built. This information provides a metric for future process control.	79
Figure 85: Calorimeter outputs from (Left) Table 1 process parameters (Right) Table 2 process parameters	80
Figure 86: Powder flow analysis of 316L and PH48S utilizing AE sensor described in [3]	80

Figure 87: representative microstructure on the top of the multilayered sample with PH48S.	81
Figure 88: New cruciform builds (left) 0.25” build, (right) 2” build, notice bottom of cruciform where excess powder was sitting and fused to the sample	82
Figure 89: top view of cruciform showing where analysis was performed	83
Figure 90: view of cruciform arm that was cut into sections for metallurgical and microstructural analysis	83
Figure 91: microstructure of bottom regions in cruciform, (left) 10 and (right) 11 showing porosity	84
Figure 92: microstructure of curved regions in cruciform, (left) 4 and (right) 12 showing little porosity	85
Figure 93: calorimeter output obtained for multilayered sample using Table 4 process parameters	86
Figure 94: (left) view of build chamber with thermocouple placement, (right) top view schematic of chamber	86
Figure 95: view of build and locations of thermocouples	87
Figure 96: Thermal data from left to right of Thermocouples 1-3	88
Figure 97: Ambient thermal data	88
Figure 98: (left) schematic of location of thermocouple for additional test (right) Thermal data from experiment showing similar results from previous test. It should be noted that bottom left detached and the data was removed	88
Figure 99: (left) screen capture from IR video (middle) the 9 regions were temp data was extracted over time (right) plot of the data extraction from the 9 regions over time.	89
Figure 100: (right) close up view of the thermal profile shown left (box region) that indicates each layer and the breaks in between as the thermal profile changes.	89
Figure 101: (left) full cruciform build done in 8 hours which is a drastic improvement from the initial 20 hours (right) location and position of thermocouple for final build	91
Figure 102: thermal profile of the cruciform build over the 8 hour period (glitch seen at 0.6 sec. (left) TC#1, (center) TC#2, (right) TC#3.	91
Figure 103: Additive manufacturing market share globally.	93
Figure 104: Market values of metal casting and additive manufacturing from 2013 to predicted marked value in 2020.	93

List of Tables

Table	Page
Table 1: KPI'S & METRICS	10
Table 2: Nominal composition (in wt.%) of Ferrium® PH48S maraging stainless steel	11
Table 3: In/Post-AM process thermal history for PH48S	11
Table 4: Solid solution strengthening coefficient in α-Fe (MPa)	21
Table 5: Calibration results	31
Table 6: Experimental values for cylindrical casting samples	43
Table 7: Optimized casting process conditions for minimum homogenization time	45
Table 8: Inputs of the precipitation and solid solution strengthening metamodels	46
Table 9: Processing parameters utilized for first "cruciform" build based on data from [2]	72
Table 10: optimized process parameters for larger beads	75
Table 11: Single Bead characteristics with new process parameters	75
Table 12: updated process parameters for PH48S builds	81
Table 13: Vickers hardness values from PH48S multilayered samples	81
Table 14: Vickers hardness for the regions shown in Figure 90	84
Table 15: Powder flow and spread for 316L and PH48S respectively	85
Table 16: position of all thermocouples used for thermal profile collection	87
Table 17: full data set of cruciform arm for final parameter settings	90
Table 18: final process parameters for repeatable PH48S cruciform build	90

I. EXECUTIVE SUMMARY

The market value of one-of-a-kind or low-volume metallic parts easily exceeds multi-billion dollars each year, considering new and legacy parts in aerospace or defense applications, tooling for mass-production, functional prototyping parts for new or legend cars, or patient-specific parts. Flexible manufacturing processes, such as additive manufacturing processes or incremental forming processes, provide exciting and promising means for high value-added manufacturing. One critical challenge however, is to be able to certify the process for a specific production; how one knows whether the just-made, one-of-a-kind part can perform the desired structural or other functional requirements.

This team developed a virtually guided certification framework of metallic manufacturing processes using physics-based simulation tools and real-time sensors integrated by the efficient Bayesian update method. It was achieved through a collaborative work among academia (Northwestern & Northern Illinois University), corporation (Siemens), and small businesses (QuesTek and PDA) with multi-dimensional technical background in manufacturing processes, materials, computational science, computer science, and software distribution.

This project builds on several core innovations developed over the past decade in virtual engineering achievements and instrumentation, and chooses additive manufacturing as a test bed to demonstrate the evolution of TRL 3-4 technologies to TRL 4-5. A voxel-based model using the octree storage data structure is used to embed material microstructure in a geometrical model economically and effectively. This is made possible, in part, by our ongoing comer stone achievement in a 900 times acceleration for simulating additive manufacturing processes through work funded by NIST measurement science for additive manufacturing. Thus, the digital manufacturing predictive model is linked from initial materials to process to mechanical properties. Another key to success was the application of the efficient Bayesian updating framework using surrogate models computed in fractions of a second, such that material input parameters are updated in the process based on the dynamic observation of the process obtained by in situ sensors to compensate input perturbations and uncertainties in modeling and processes.

The deliverables for virtual certification consist of (1) a materials and process data structure, (2) a Bayesian updating framework, and (3) user friendly commercial software integration. This foundation is applicable to manufacturing processes in general but demonstrated with additive manufacturing (AM). The structure and the experts involved in this team have developed an open material data structure and process data structure elastic to accommodate future process developments (e.g., subtractive (machining), volume-constant (forming, casting) and additive manufacturing.

Software developed in this project is embedded within Siemens NX to virtually build parts. Northwestern and QuesTek Innovations LLC integrated different models from process to microstructure with the prediction of mechanical properties. This comprehensive virtual manufacturing toolkit provides linkage among process, structure and properties. This module quantifies the quality of the manufactured part in terms of geometric fidelity and predicted mechanical property based on chosen build head path and other AM variables. This virtual certification tool is of particular value for small and medium enterprises, with limited resources for developing process insensitive efficient approaches to meet OEM requirements.

User manual and tutorials were developed for workforce development and tested at DMDII's beta site, EIGERlab. This work is further leveraged through the Chicago-regional NIST-funded CHiMaD (Center for Hierarchical Materials Design) for education and outreach infrastructure already in place.

II. PROJECT OVERVIEW

Problem Statement and DMDII Relevance

The objective of this project was to establish a foundation for rapidly certifying manufacturing processes using physics-based simulation tools and real-time sensors integrated by the efficient Bayesian update framework. We created three key capabilities that are currently missing in practices that hinder rapid certification of fabricating one-of-a-kind products using novel manufacturing processes, which were:

a) *A unified material data structure* (Task 1) and *process data structure* (Task 2) for information needed by various parts in the digital manufacturing sequence such that individual material model or process model can be seamlessly linked as a plug-and-play module in the digital world;

b) *An adaptive Bayesian inference algorithm* (Task 3) to consider the uncertainty in physics-based computational models, that directs the updating of material parameters in the physics-based simulations using in-situ sensors; and

c) *A direct integrated framework* (Task 4) of material microstructural evolution during the process, as well as its influence on mechanical properties, via an extremely efficient computational method such that real-time updating is feasible;

The foundation, as illustrated in Fig. 1, will be applicable to various rapid manufacturing processes, particularly for those high-value-added, low-volume productions, for example, metal-based additive manufacturing (AM) processes, dieless three-dimensional sheet metal forming processes, precision machining, and investment casting. The AM LENS (Laser Engineered Net Shaping) process, was used as a *verification and validation testbed* (Task 5) to demonstrate the approach while knowledge from other processes was used to ensure that the framework can be extended/applicable to other metal-based manufacturing processes in general. The team for this project included experts in the above mentioned processes covering materials from the powder form to the bulk form, including all three major processes, i.e., subtractive, net-shape, and additive.

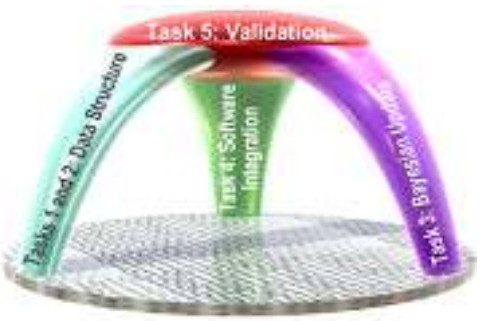

Fig. 1: Foundation of the Verification Framework.

Project Deliverables

- Digital material data structure that can handle powder and bulk metallic materials integrated with CAD packages such that local material information and microstructure can be captured.
- Digital process data structure that can be incorporated with CAD packages to assess the manufacturability and for process planning. The data structure will be able to track time-dependent toolpath information used in AM processes, incremental forming process or machining process, and can store time-independent process information, such as in investment casting.
- Validation methodology that is suitable for verifying low-volume production using Bayesian updating method combined with real-time sensing as well as the software package of the Bayesian inference approach and GP surrogate models.
- The integration result of the above 3 key deliverables will be demonstrated through a butterfly coupon test with an AM process using a software platform based on NX.
- Software framework in prototype quality (binary) for the integration of simulators of manufacturing processes with NX CAD as interface to the user's input and NX CAE as output interface for results visualization.

III. KPI'S & METRICS

KPI'S and metrics can be seen in Table 1.

Metric	Baseline	Goal	Results	Validation Method
Digital materials	-Proprietary material properties as a function of temperature -Commercial software allows table look up	-Open source digital materials with constitutive equation representation	-Material meta-model that captures constitutive relationship available upon request	-Experiments -Cross validation
Process data structure	-Start-up software & process modelers require $250K, a huge hurdle for SME -Materials and process information are cumbersome to collect and trace	-Digital structure that contains microstructure, geometry and process information all in one -Lower the barrier for software integration to engage startup and SME firms	-Voxel structure contains geometry, and simulation solution variables -Standard interface has been developed for tool path and process parameters -Voxel code is used to link GAMMA and NX -Developed high level architecture to contain critical process parameters	-Code verification and unit tests -Demonstration simulation
Simulation software integration	-Users require to perform multiple interactions with different software tools to obtain desired quality KPI on the manufactured part -Uncertainties are expensive to be considered (in days – months)	-Users will provide a list of inputs to a single software framework to obtain the desired quality KPI on the manufactured part. -Will efficiently adapt uncertainties in process and simulation	- Single software framework based on NX that connects several software tools to perform various steps of qualification and verification test and calculate uncertainty	-Code verification and unit tests -Demonstration
Reduction of time and cost	-Requires a large volume of prototypes for functional testing and 8-15 month (AM parts)	-Will enable a potential reduction of the certification time by 50%	-Build time has been shortened by ⅔ -Meta-model reduced prediction time from hours to seconds -GPU version has reduced simulation time by 100x -Integrated software has streamlined the certification and verification workflow, eliminating many hours of manual processing	-Reduced number of empirical trials -Experimentally demonstrated a build time reduction from 20 hours to 8 hours

IV. TECHNOLOGY OUTCOMES

Task I. Digital Material Structure

Ferrium® PH48S maraging stainless steel was adopted as a benchmark, with the nominal composition listed in Table 2. PH48S is a forgeable and castable corrosion-resistant high-strength steel, computationally designed by QuesTek Innovations LLC, as a lower-cost alternative to cast titanium for structural applications subjected to corrosive environments [1]. PH48S utilizes an efficient intermetallic η-Ni_3(Ti, Al) phase as a strengthening dispersion precipitated through ageing. Since PH48S exhibits excellent solidification behavior, it becomes a candidate for additive manufacturing processing.

Table 2: Nominal composition (in wt.%) of Ferrium® PH48S maraging stainless steel

Element	Fe	Cr	Ni	Co	Mo	Ti	Al	C	O	N
Nominal	Bal.	10.9-11.3	8.6-9.0	7.2-7.6	1.5-1.7	0.58-0.62	0.40-0.45	0.008-0.012	–	–

In this project, a certification framework for DED PH48S tensile yield strength was created using physics-based simulation tools. Since PH48S is applied in the aged condition, it is appropriate to evaluate the strength after all post-process steps (listed in Table 3) are performed.

Table 3: In/Post-AM process thermal history for PH48S

Step No.	In/Post-AM process thermal history
1	LENS process
2	Homogenization + FC 1200 °C, 4 hours
3	Solution + WQ 800 °C, 1 hour
4	Cryogenic treatment + AW -73 °C, 2 hours
5	Ageing + WQ 520 °C, 4 hours

* FC – furnace cool; WQ – water quench; AW – air warm

In Task I, the physics-based models to predict tensile yield strength was identified and calibrated following the flow chart shown in Figure 2. The total tensile yield strength is contributed by the strength of pure BCC-Fe, precipitation strengthening (by η/B2 and oxide), solid-solution strengthening, grain boundary strengthening and dislocation substructure strengthening.

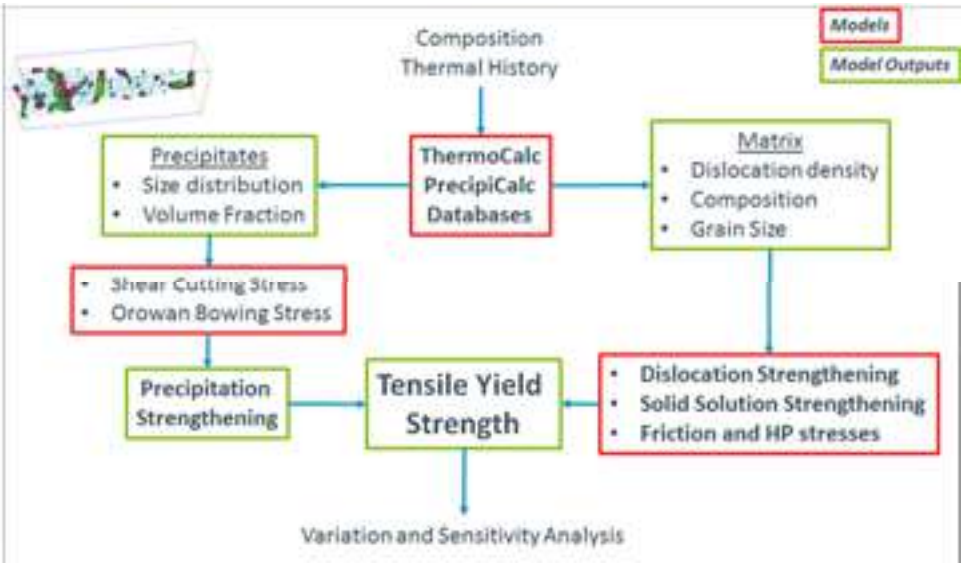

Figure 2: Digital flow chart for tensile yield strength prediction

A. Oxide strengthening

Finely dispersed oxide inclusions were observed in the as-deposited LENS PH48S (Figure 3). STEM-EDX analysis identify them to be rich in Al and Ti, which corresponds to the stable corundum phase (Figure 4) as predicted by the thermodynamic database with the composition of the build Fe-10.9Cr-8.67Ni-7.31Co-1.59Mo-0.61Ti-0.35Al-0.009C-0.013O (in wt.%).

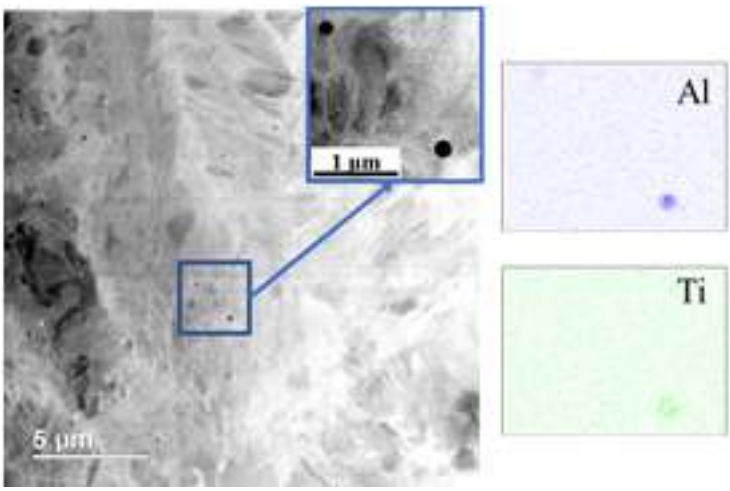

Figure 3: Submicron corundum oxide particles in the as-deposited LENS PH48S

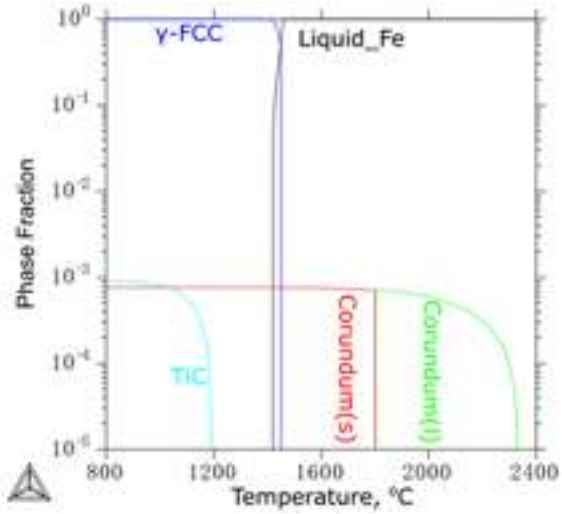

Figure 4: Step diagram of PH48S with the composition Fe-10.9Cr-8.67Ni-7.31Co-1.59Mo-0.61Ti-0.35Al-0.009C-0.013O (in wt.%)

Strengthening by oxide particles can be evaluated by the Orowan equation, as in Equation ,1

$$\Delta\tau_{\text{oro}} = \frac{Gb}{\sqrt{\pi}} \cdot \frac{\sqrt{f}}{r} \qquad 1$$

where G = 71 GPa is the shear modulus of α-Fe and b = 0.219 nm is the Burgers vector.

Oxides evolve during the AM process and the subsequent heat-treating steps. With the AM thermal profile (as shown in Figure 5), which is simulated by the GAMMA code, input to the *PrecipiCalc* software, oxide evolution during AM thermal cycles (above the liquidus temperature) can be predicted.

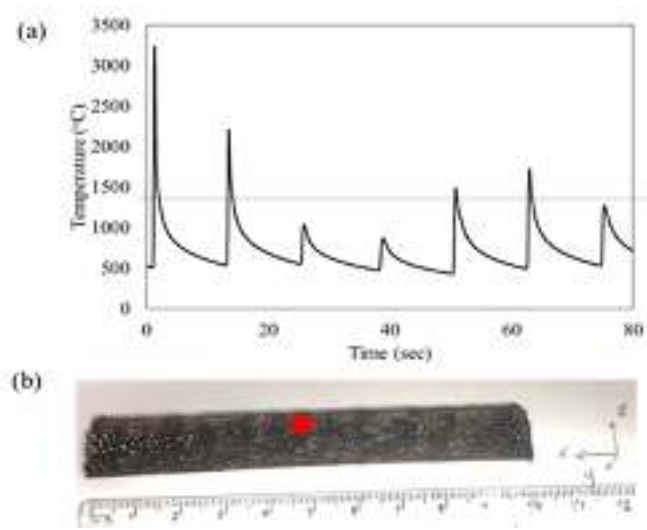

Figure 5: The simulated thermal profile (a) for the top center point in the PH48S bar as indicated by the red dot (b).

The temperature-dependent interfacial energy between corundum and liquid Fe is taken from literature data as represented in Figure 6. The simulated evolution of oxide distribution is displayed in Figure 7 (a), which matches well with the experimental observations in Figure 7 (b).

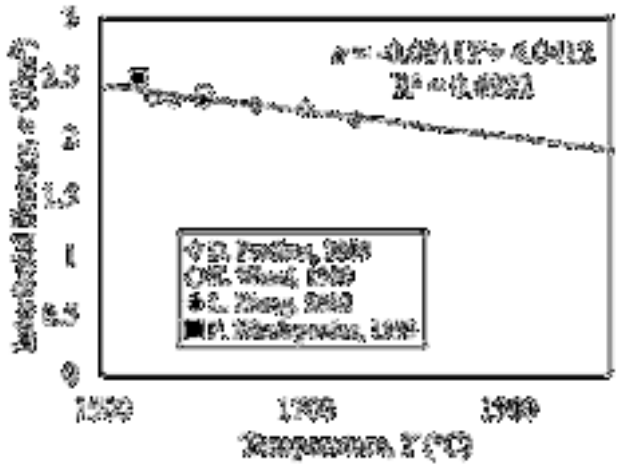

Figure 6: Temperature-dependent interfacial energy between corundum and liquid Fe [2–4].

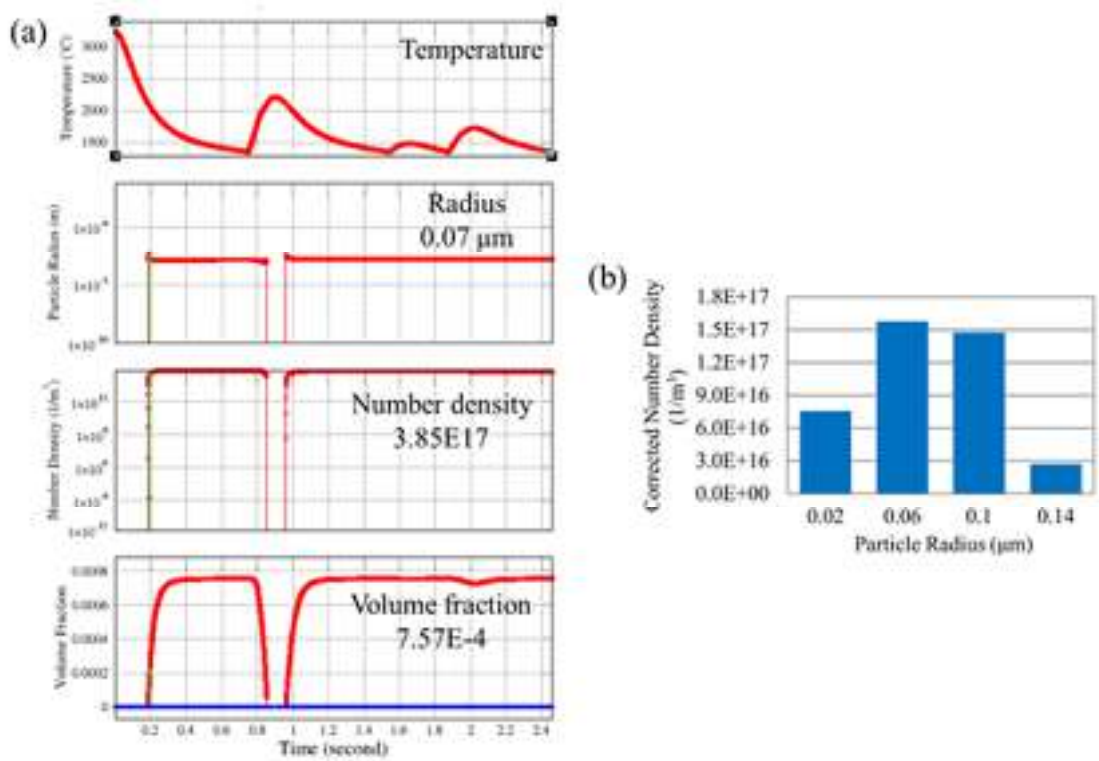

Figure 7: A comparison of (a) predicted oxide evolution by PrecipiCalc simulation and (b) experimental characterization of as-deposited size.

B. Grain boundary strengthening

1200 °C is the HIPping/homogenization temperature for PH48S. Therefore, evolution of prior austenite grain size and oxide size distribution during 1200 °C isothermal heat treatment was investigated and correlated in terms of the Zener pinning effect of the submicron oxide particles.

The evolution of prior austenite grain size during 1200 °C isothermal heat treatment is shown in Figure 8. Columnar grain structures still prevail after holding for 2 hours, but the formation of small equiaxed grains indicates recrystallization, which is also implied by the grain size drop in the quantitative grain size analysis (Figure 8 (e)). After prolonged holding for a day, most grains turn equiaxed and coarsen slowly. The slow grain coarsening rate is attributed to the high stability of the oxide phase. The evolution of oxide size distribution was characterized by STEM. In the equiaxed grain regime, a linear relationship between the recrystallized prior austenite grain size and the oxide size distribution (*d*/*f*) is constructed in Figure 9 according to the Zener-Gladman boundary pinning model [5] described by Equation 2,

$$D = \frac{4}{3}\left(\frac{3}{2} - \frac{2}{Z}\right)\frac{d}{f} \qquad 2$$

where *d* is the average pinning particle diameter, *f* is the total volume fraction of the pinning particle, and *Z* is a grain size distribution parameter. From Figure 9, the *Z* value for the PH48S system is calibrated to be 1.53, which is within a reasonable range (1.4~2.0).

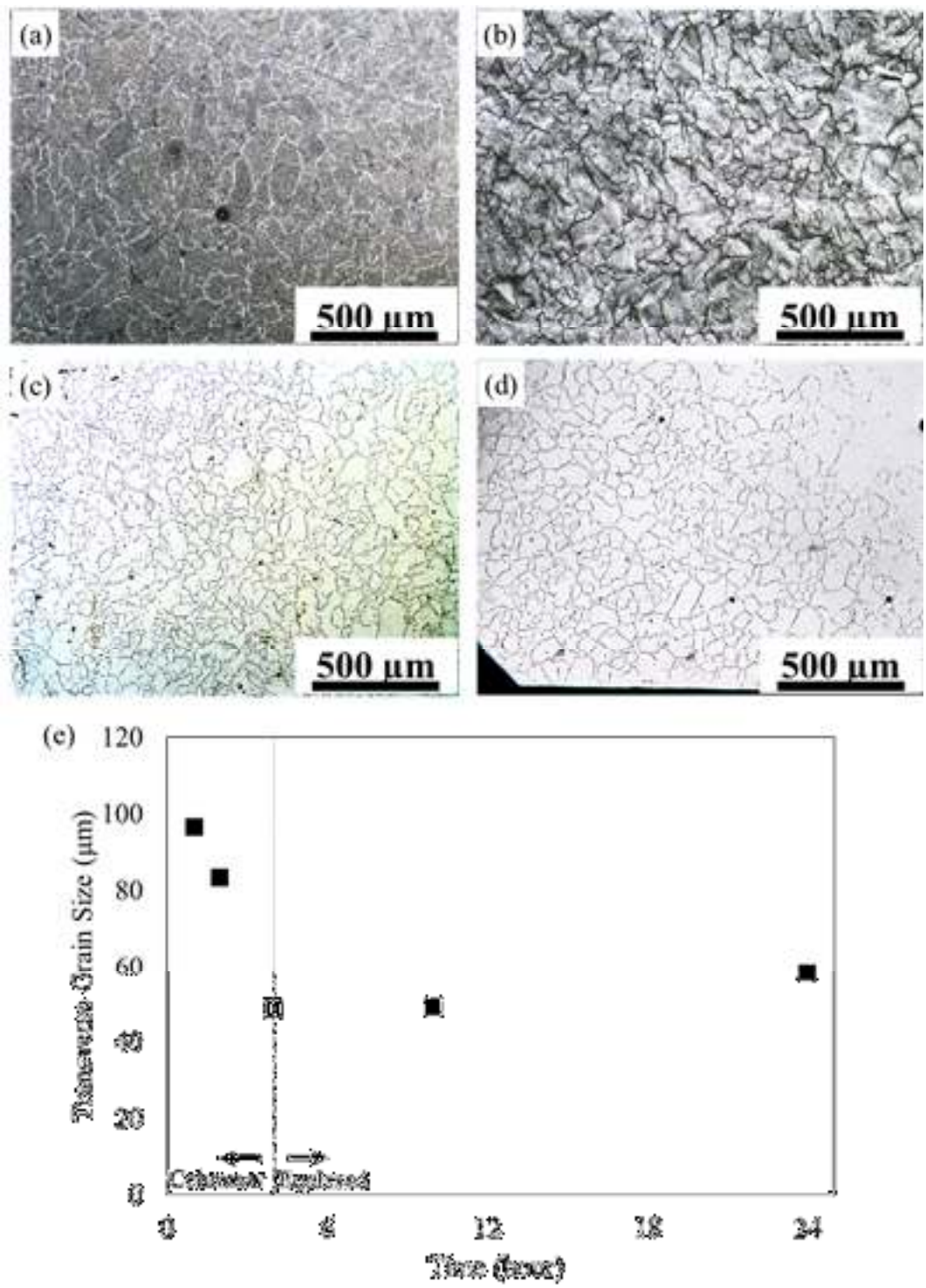

Figure 8: Evolution of prior austenite grain structure during 1200 °C isothermal heat treatment for (a) 1 hour, (b) 2 hours, (c) 12 hours and (d) 24 hours with (e) quantitative analysis.

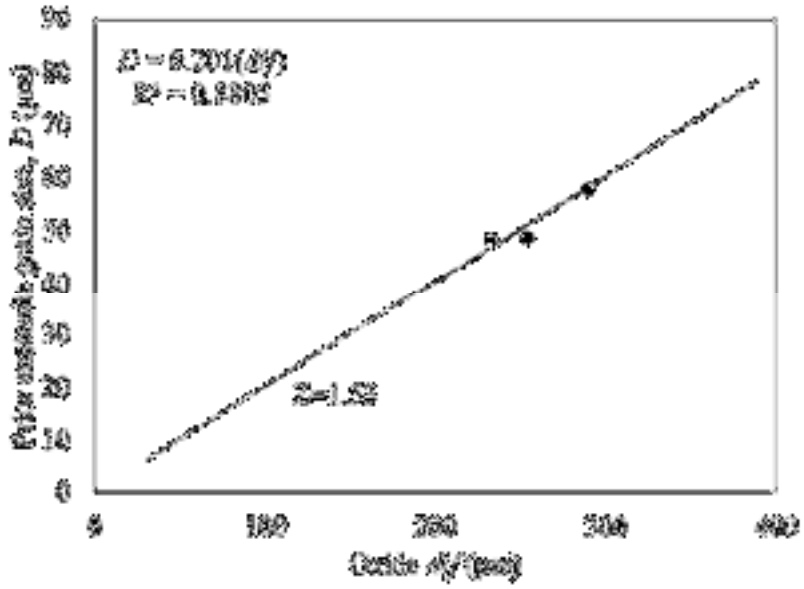

Figure 9: The linear relationship between the prior austenite grain size (in the equiaxed regime) and oxide size distribution with the *Z* value calibrated to be 1.53.

Since only the prior austenite grain size in the equiaxed regime is used to fit the pinning model, the fitted model may be not applicable to estimate the average grain size in the columnar regime. However, it can still predict the largest size that the recrystallized grains can grow into. With the Zener pinning model, the recrystallized prior austenite grain size can be predicted by the oxide size distribution. Due to the martensitic structure within the prior-austenite grain, the grain boundary strengthening is represented by the martensite packet size, which can be linearly related with the prior austenite grain size using Equation 3, according to Figure 10.

$$D_p\ (\mu\text{m}) = 0.3749 \times D_\gamma + 2.9033 \qquad 3$$

The yield stress increment by grain boundary strengthening is described by the Hall-Petch equation (Equation 4),

$$\sigma_{HP}(\text{MPa}) = K{D_p}^{-1/2} \qquad 4$$

where K = 0.2 MPa $m^{1/2}$ is the Hall-Petch constant for martensite packets [6].

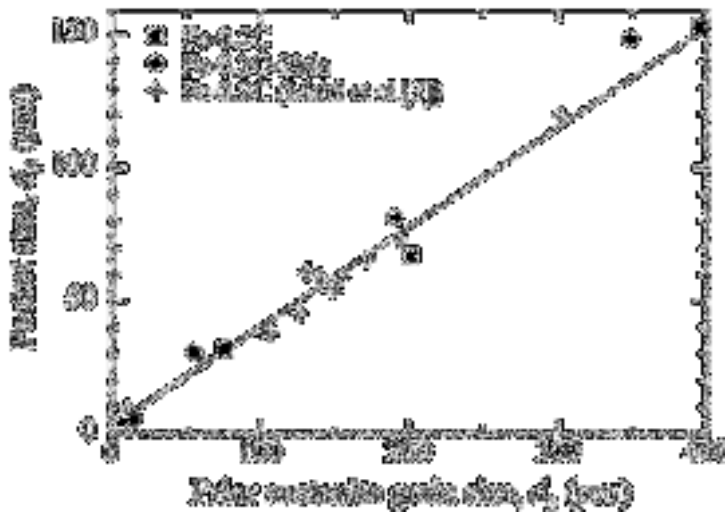

Figure 10: Relationship between the prior austenite grain size and the packet size in quenched martensite in the Fe–0.2C and the Fe–0.2C–2Mn alloys [7].

C. Precipitation strengthening

Upon ageing, two types of intermetallic phases, η-Ni_3(Ti,Al) and B2-NiAl, precipitate from the martensitic matrix.

The strengthening by η phase can be described by Equation 5, which considers the effect of coherency strengthening and modulus strengthening, when the particles are shearable. When the particles are impenetrable, the strengthening effect is described by Orowan strengthening with shape correction term as in Equation 6.

$$\Delta\sigma_{\eta_{shear}}\ (\mathrm{MPa}) = \alpha_e G \varepsilon^{1.5} \sqrt{\frac{fR}{b}} + 0.9\sqrt{fR}\frac{Gb}{2}\left(\frac{\Delta G_1}{G}\right)^{1.5}\left[2b\ln\left(\frac{2R}{\sqrt{f}b}\right)\right]^{-1.5} \qquad 5$$

$$\Delta\sigma_{\eta_oro}\ (\mathrm{MPa}) = 0.15G\frac{b}{D_r}(f^{0.5} + 1.84f + 1.84f^{1.5})\ln\left(\frac{1.316D_r}{b}\right) \qquad 6$$

where

$$D_r = \left(\frac{8}{5}R^3\right)^{1/3} \qquad 7$$

The values of the parameters involved in the above equations are: α_e = 3.7, G = 71, ε = 2/3×0.0222, b = 0.219 nm, ΔG_1 = 64 GPa (shear modulus difference between α-Fe and η). The

strengthening by η phase is determined by the lower of the two strengthening mechanisms, i.e., $\sigma_\eta = \min\{\sigma_{\eta_shear}, \sigma_{\eta_oro}\}$.

B2-NiAl phase precipitates simultaneously with the η phase. Since B2 particles are fine and shearable, only the dislocation-shearing mode is considered. The strengthening model for B2 phase is given by Equation 8, considering the effects by modulus strengthening and ordering strengthening [8].

$$\Delta\sigma_{B2_shear}\ (\mathrm{MPa}) = \frac{\Delta G_2}{4\pi^2}\left(\frac{3\Delta G_2}{Gb}\right)^{1/2}\sqrt{fR}\left[0.8 - 0.143\ln\left(\frac{R}{b}\right)\right]^{2/3} + \frac{\gamma^{3/2}}{b}\left(\frac{8R_s f}{\pi G b^2}\right)^{1/2} \quad 8$$

where

$$R_s = (2/3)^{1/2}R \quad 9$$

The values of the parameters involved in the above equations are: ΔG_2 = 17 GPa (shear modulus difference between α-Fe and B2) and γ = 0.5 J/m^2 (anti-phase boundary energy) [8].

The evolution of η and B2 phases during 520 °C ageing can be simulated by the PrecipiCalc software, with the interfacial energy for η and α-Fe as 0.2 J/mol and the interfacial energy for B2 and α-Fe as 0.02 J/mol. The matrix composition at 800 °C (Fe-10.91Cr-8.68Ni-7.32Co-1.59Mo-0.57Ti-0.34Al in wt.%) is used for the precipitation simulation during ageing. The evolution of η phase and B2 phase size distribution during the standard ageing process (520 °C for 2 hours) is shown in Figure 11 (a,b), and the corresponding stress increments are shown in Figure 11(c).

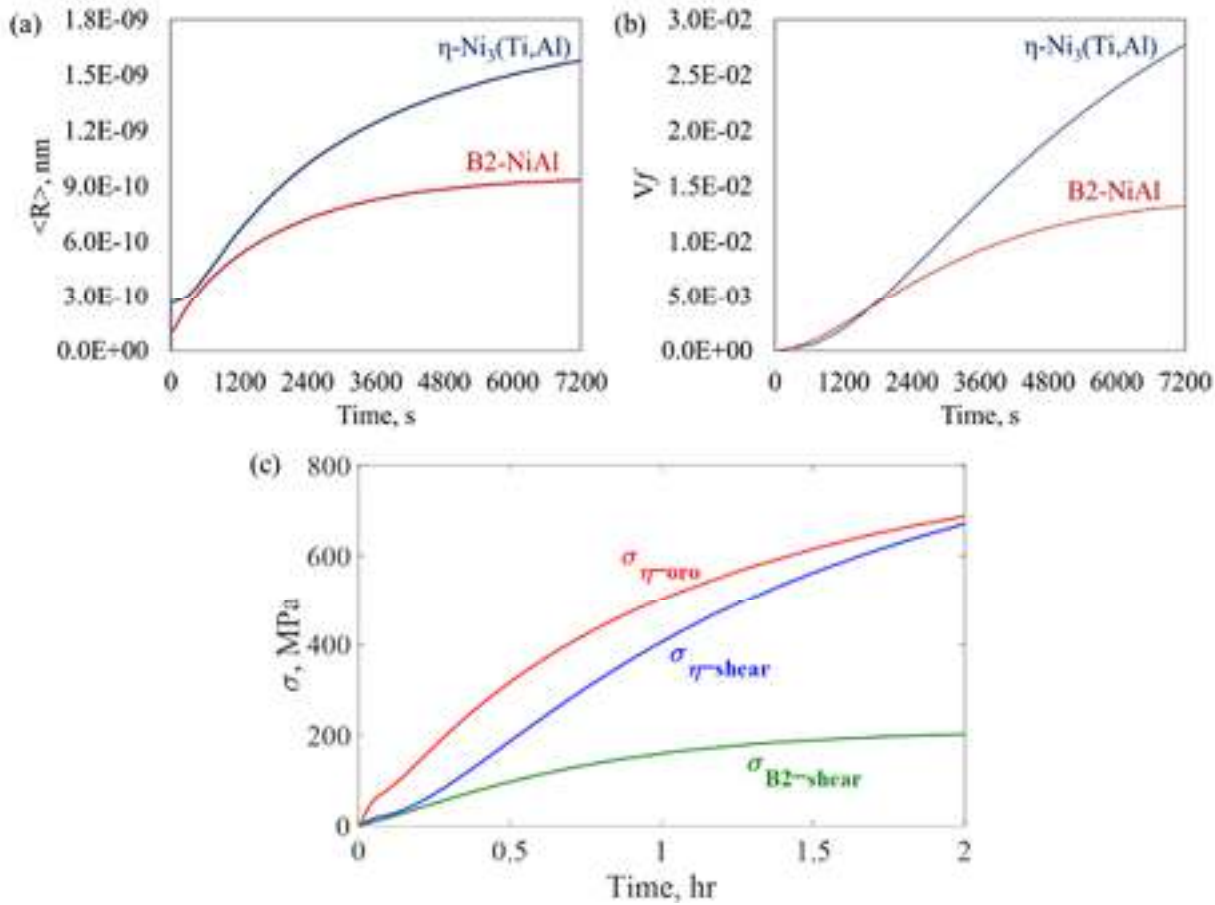

Figure 11: Evolution of η phase and B2 phase during ageing at 520 °C in terms of (a) average particle radius, (b) volume fraction and (c) strengthening effect.

The total precipitation strengthening effect with mixed types of precipitates can be calculated through the power law for the superposition (Equation 10) with the superposition exponent *p* as 1.71 [6].

$$\sigma_{ppt}\ (\mathrm{MPa}) = \left({\sigma_\eta}^p + {\sigma_{B2}}^p + {\sigma_{\mathrm{oxide}}}^p\right)^{\frac{1}{p}} \qquad 10$$

D. Solid solution strengthening

The solid solution strengthening of the matrix is given by Equation 11 [9],

$$\sigma_{sss}\ (\mathrm{MPa}) = 0.95 \times 0.0078 \times G \times \sum_i k_i c_i^{2/3} \qquad 11$$

where c_i is the atomic fraction of the element i in the matrix and k_i is the strengthening coefficient (Table 4).

Table 4: Solid solution strengthening coefficient in α-Fe (MPa)

Cr	Ni	Co	Mo
0.19744	0.67128	0.21366	1.37421

The matrix composition after ageing is obtained from the *PrecipiCalc* simulation.

E. Dislocation strengthening

Dislocation strengthening depends on the dislocation density (ρ) according to Equation 12.

$$\tau_{dis}\ (\mathrm{MPa}) = Gb\sqrt{\rho} \qquad 12$$

In maraging steels, the dislocation density is ~10^{14} m^{-2} in the as-quenched condition [10,11]. Dislocations recover during ageing, and the dislocation density is estimated to drop to 0.5 × 10^{14} m^{-2} [11].

F. Total tensile yield strength

Assuming the total yield strength is the linear superposition of all strengthening contributions, the total yield strength can be therefore expressed by Equation 13.

$$\sigma_y\ (\mathrm{MPa}) = M(\tau_{\alpha\text{-Fe}} + \tau_d) + \sigma_{ppt} + \sigma_{SSS} + \sigma_{HP} \qquad 13$$

where M = 2.8 is the Taylor factor for BCC-metals, and $\tau_{\alpha\text{-Fe}}$ = 64 MPa is the Peierls stress of pure α-Fe [6].

For PH48S tensile bars that went through the whole heat-treating steps, the tensile yield strength is predicted as shown in Figure 12 with the composition Fe-10.9Cr-8.67Ni-7.31Co-1.59Mo-0.61Ti-0.35Al-0.009C-0.013O (in wt.%). The predicted value of the total tensile yield strength is very close to the measured value.

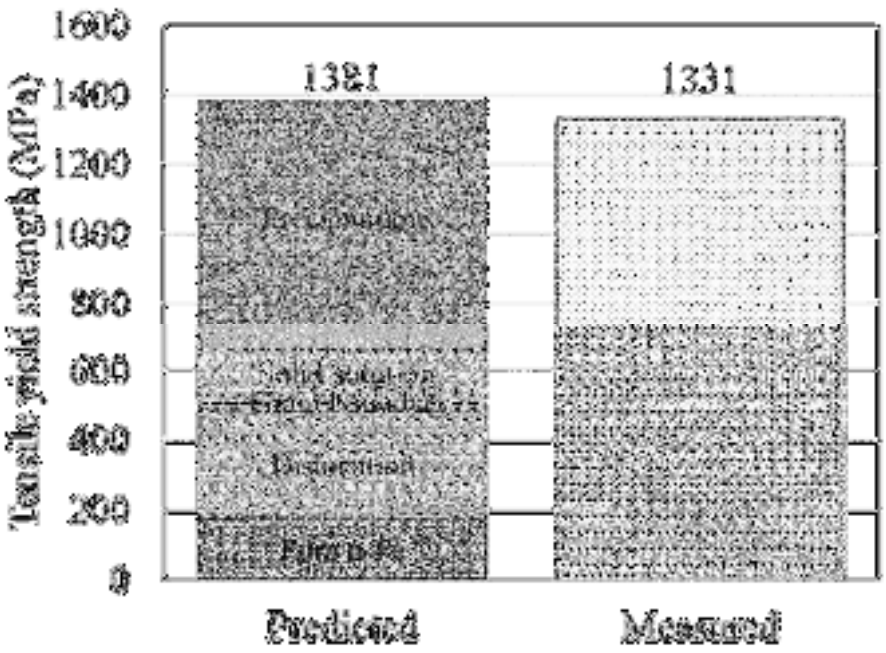

Figure 12: The tensile yield strength of LENS PH48S tensile bar: (a) predicted; (b) measured.

Reference (Task I)

1. Wright, J.; Jung, J.-W. MARTENSITIC STAINLESS STEEL STRENGTHENED BY NI3TI η-PHASE PRECIPITATION 2011.

2. Nikolopoulos, P.; Agathopoulos, S.; Tsoga, A. A method for the calculation of interfacial energies in Al2O3 and ZrO2/liquid-metal and liquid-alloy systems. *J. Mater. Sci.* 1994, *29*, 4393–4398, doi:10.1007/BF00414227.

3. Zhang, L.; Pluschkell, W.; Thomas, B. G. NUCLEATION AND GROWTH OF ALUMINA INCLUSIONS DURING STEEL DEOXIDATION. In *85th Steelmaking Conference*; Warrendale, PA, 2002; pp. 463–476.

4. Pradhan, D.; Steel, T.; Reddy G., R. Thermodynamics of Interfacial Properties between Liquid Iron, Liquid Silicon and Solid Oxide Substrates Phase Equilibria, Thermodynamic and Transport Properties of TE Alloys View project High Temperature Solid Oxide Fuel Cells View project Thermodynamics of Interfacial Properties between Liquid Iron, Liquid Silicon and Solid Oxide Substrates. *High Temp. Mater. Process.* 2009, *28*, 203–210, doi:10.1515/HTMP.2009.28.4.203.

5. Olson, G. B. Overview: Science of Steel. In *Innovations in Ultrahigh-Strength Steel Technology*; Olson, G. B., Azrin, M., Wright, E. S., Eds.; U.S. Army Laboratory Command, Materials Technology Laboratory: Watertown, Massachusetts, 1987; pp. 3–66.

6. Wang, J.-S.; Mulholland, M. D.; Olson, G. B.; Seidman, D. N. Prediction of the yield strength of a secondary-hardening steel. *Acta Mater.* 2013, *61*, 4939–4952, doi:10.1016/J.ACTAMAT.2013.04.052.

7. Morito, S.; Yoshida, H.; Maki, T.; Huang, X. Effect of block size on the strength of lath martensite in low carbon steels. *Mater. Sci. Eng. A* 2006, *438–440*, 237–240, doi:10.1016/J.MSEA.2005.12.048.

8. Jiang, S.; Wang, H.; Wu, Y.; Liu, X.; Chen, H.; Yao, M.; Gault, B.; Ponge, D.; Raabe, D.; Hirata, A.; Chen, M.; Wang, Y.; Lu, Z. Ultrastrong steel via minimal lattice misfit and high-density nanoprecipitation. *Nature* 2017, *544*, 460–464, doi:10.1038/nature22032.

9. Qian, Y. Residual stress control and design of next-generation ultra-hard gear steels, PhD Thesis, Northwestern University, 2007.

10. Galindo-Nava, E. I.; Rainforth, W. M.; Rivera-Díaz-del-Castillo, P. E. J. Predicting microstructure and strength of maraging steels: Elemental optimisation. *Acta Mater.* 2016, *117*, 270–285, doi:10.1016/J.ACTAMAT.2016.07.020.

11. Zhu, F.; Yin, Y. F.; Faulkner, R. G. Microstructural control of maraging steel C300. *Mater. Sci. Technol.* 2011, *27*, 395–405, doi:10.1179/026708309X12506933873503.

Task 2: Process Data Structure

A Process Data Structure was developed for the computation, storage, and querying of geometries and variables. Under this task, a voxel data structure was implemented and demonstrated. Further improvements were also made to the GAMMA (Generalized thermal simulation code and its preprocessor to give improved speed, accuracy, and useability, allowing integration within the part certification framework developed under this project.

A. Voxel Data Structure

A voxel data structure was developed to act as a link between the CAD engine (Siemens NX) and the FEM thermal simulation software (GAMMA, for "Generalized Analysis of Multiscale and Multiphysics Applications"). This voxel structure was implemented in a C++ program (VoxelCode) that is included with the project software deliverables. Within this software tool, geometry and solution fields from GAMMA, which uses a native unstructured finite element representation, are interpolated on a uniform voxel grid using a fast search and interpolation algorithm. This interpolation was initially demonstrated through application to a sample case simulating the generation of a cruciform build through the DED process (Figure 13). The voxel interpolation and query operations are parallelized to improve efficiency.

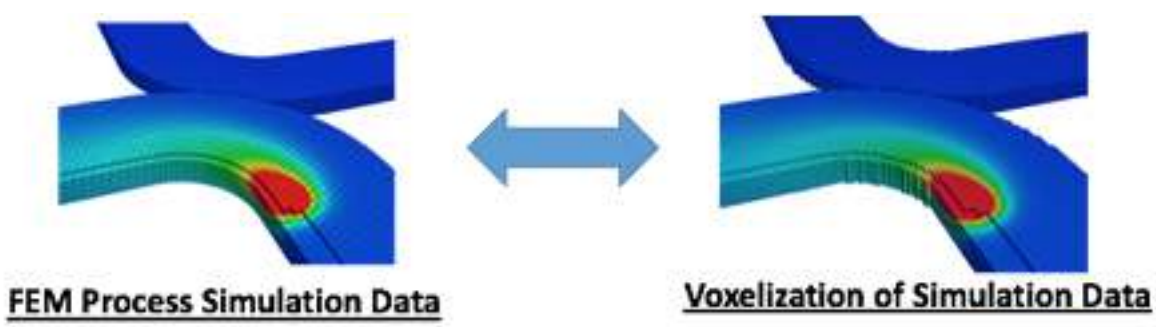

Figure 13: Interpolation of simulated temperature field from unstructured finite element method (FEM) mesh to the voxel structure for the cruciform build

To allow further resolution of the voxel data structure where needed, an octree refinement was added to the voxel structure. This approach allows local refinement to better capture geometric interfaces and large gradients while reducing memory and file storage requirements. An example of the octree refinement of the cruciform geometry is shown in Figure 14.

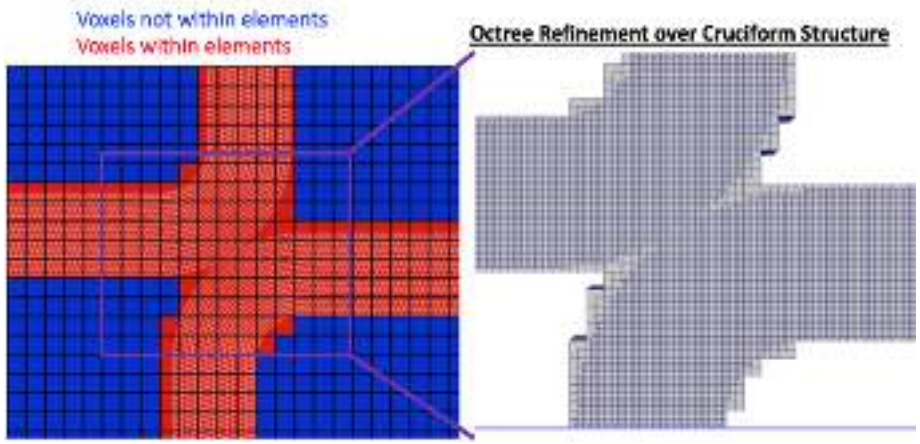

Figure 14: Octree refinement for the cruciform geometry

Each voxel gets divided into eight smaller structured voxels in every Octree refinement level and this enables the voxel representation to more accurately capture the curvatures in the main grid. Normally, three levels of voxel refinements are sufficient to fully cover the entire geometry with a structured voxel grid without overuse of memory.

Temperature of every voxel is determined based on the temperature of the finite element that it belongs to. More precisely, the voxel temperature is interpolated among the nodes that make up the aforementioned element. (Figure 16). This interpolation method is also used to compute the associated voxelized quantities of any other scalar or vector physical field properties, such as solidification cooling rate (scalar) and thermal flux (vector). The voxelized representation of the temperature field data with multiple refinement levels for the step-plate build is shown Figure 15. It is clear that a higher accuracy in representing the temperature field is achieved with every refinement level.

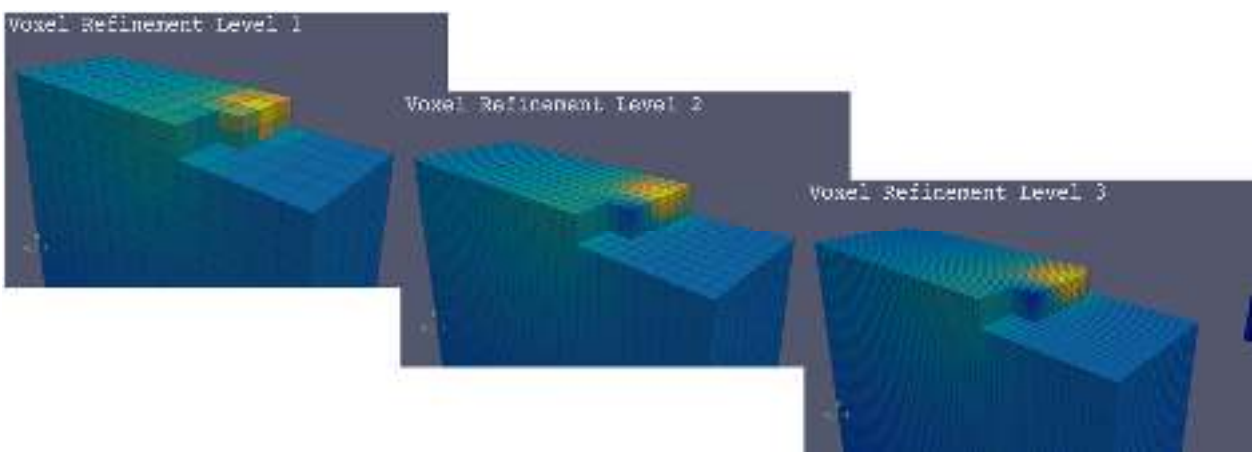

Figure 15: Temperature field for step-plate at three levels of voxel refinement

Another purpose of voxelizing the computational grid is to accelerate the probing of the calculated properties at any point within the domain. These properties include thermal properties that are computed by the thermal simulation, such as temperature, and the structure properties that are obtained by Task 3 and will be written into the voxel structure. Having already interpolated the computed field variables facilitates

querying data given the coordinates of the desired location because there is no need for interpolating within the main finite element mesh. Figure 16 shows how first a voxel is tagged or associated with an unstructured element and then its properties are computed based on the nodal values of the element.

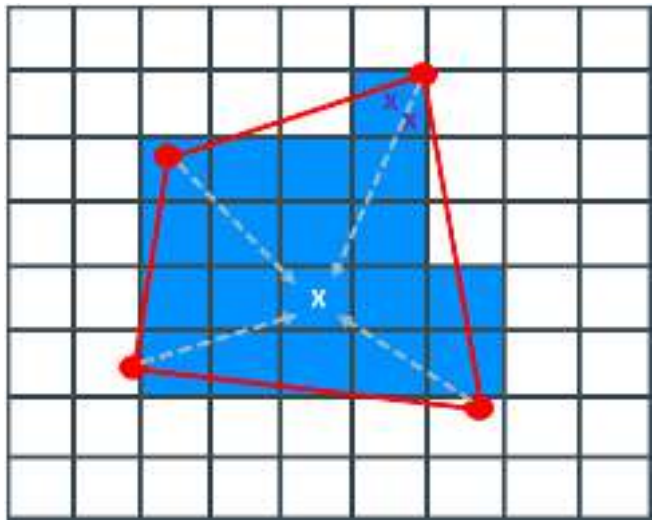

Figure 16: overlaying a structured voxel grid on the mesh, tagging the voxel to the FEM element that encompasses it, interpolating the properties based on nodal values

There are two query operations designed in the voxel code:

1. probing all the field properties that are computed through the thermal simulation
2. probing final structural properties, such as yield strength, that are computed by Task 3

Different stages of the voxel code, such as voxel refinement, property interpolation, data query and generating the output files, have been parallelized to enhance the computational efficiency. Figure 17 shows the gained speedup in the computational time with respect to the number of processors used for running the code.

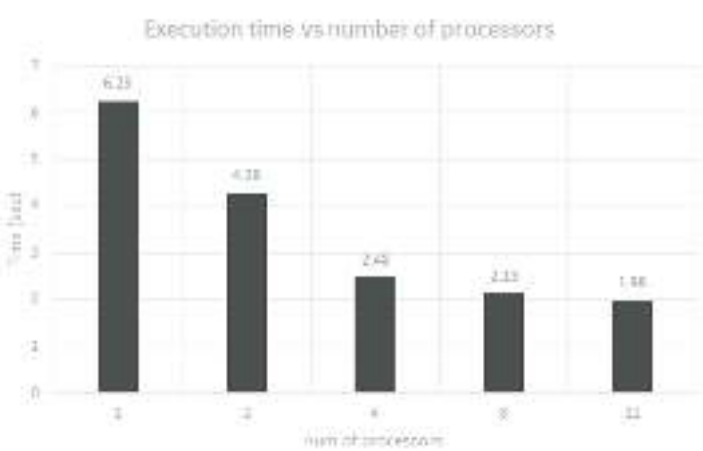

Figure 17: parallelization of the voxel code reduces the computational time

B. GAMMA Preprocessor

An important step in the prediction of temperature history in the AM part is the conversion of mesh and toolpath data to a format readable by the finite element code, GAMMA. Because GAMMA uses an "element birth" formulation to model the addition of material during the DED process, with new elements being activated as metal is deposited at each spatial location, the toolpath and mesh must be preprocessed to yield a schedule for the birth of new elements. This is accomplished through the GAMMA Preprocessor code. The workflow of the original preprocessor code is shown in Figure 18. As seen from this figure, both the mesh file and the original machine DMC toolpath is needed to generated this birth curve. In addition, the a toolpath generator is needed to convert the DMC file into a format acceptable by GAMMA. The toolpath generator, in particular, is difficult to maintain as new functionalities needed to be added into the software as more complex builds were generated in order to generate the corrected movements of the laser within the simulation. These steps allow the generation of the birth curve, which is then inputted into the GAMMA input file.

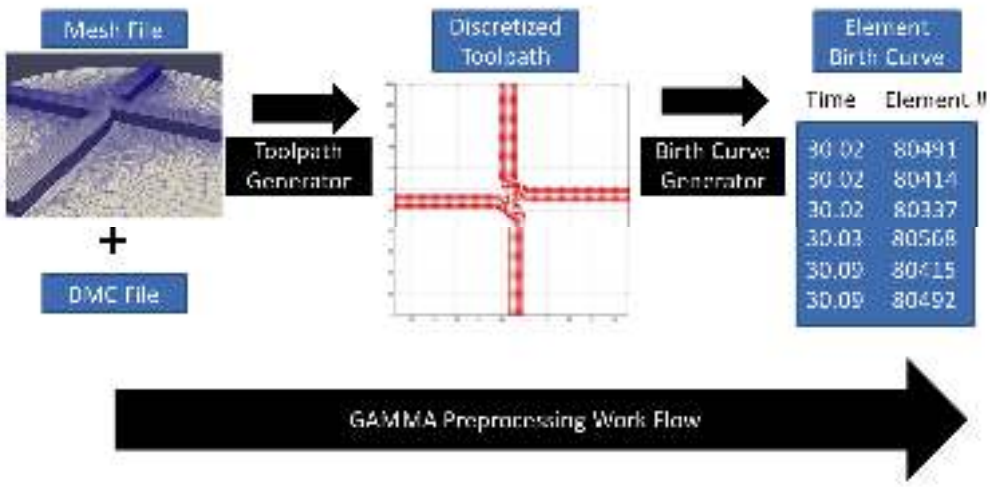

Figure 18: Schematic of work flow of old version of GAMMA preprocessor

As part of this project, the GAMMA preprocessor was revised and rewritten in C++. It takes inputs in the form of data files that are output from the NX software, allowing a simple interface within the overall analysis workflow. As a result, a large portion of the work associated with preprocessing has been substantially reduced; a DMC file and toolpath generator is no longer necessary, since both of these are provided by the NX software. The output of the Preprocessor software is a file containing the element birth schedule, which is in turn read by the GAMMA simulation code. The GAMMA Preprocessor software is included in the project software deliverables.

C. GAMMA

The main thermal simulation software used for AM modeling in this project is GAMMA, an in-house finite element code developed at Northwestern University. GAMMA was developed for AM applications, in particular DED processes, and includes a mass addition model using an element birth strategy. The mass addition model is based off of the inactive element approach [1,2]. In this approach, elements are not included in the analysis until the corresponding material is deposited; this results in a more computationally efficient approach as this reduces the number of nodal degree of freedoms to be solved at the beginning of the analysis. Figure 19 shows a schematic of the inactive element scheme, where the

deposited “active” material are solved for and have a temperature field, whereas the elements that are labelled “inactive” do not carry any material and are not solved for; as a result the “inactive” elements do not have a temperature field associated with them.

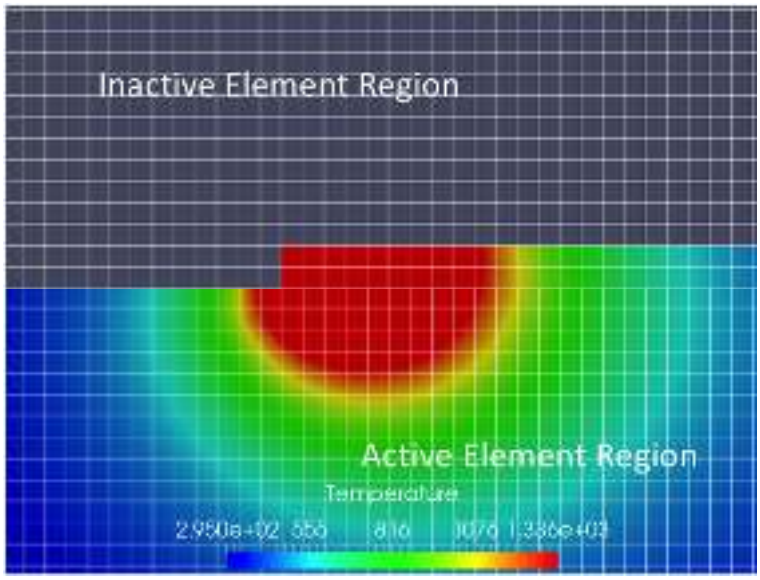

Figure 19: Schematic showing inactive element method

The heat equation is solved to resolve a spatially varying temperature field as a function of time. The heat equation is given in Equation 14 below:

14

$$\rho c_{p,eff} \frac{\partial T}{\partial t} - \nabla \cdot (\kappa \nabla T) = 0$$

where \rho is the density, c_{p,eff} is the effective specific heat, T is the temperature, and \kappa is the thermal conductivity. Radiation, convection and a moving gaussian flux conditions are applied to the evolving boundary that tracks the interface of the mass deposition front, and are given in Equations 15, 16, and 17, respectively:

15

$$q_{conv} = h(T - T_{amb})$$

16

$$q_{rad} = \sigma\varepsilon(T^4 - T_{amb}^4)$$

17

$$q_{laser} = -\frac{2\alpha P}{\pi R_b^2} \exp\left(-\frac{2r^2}{R_b^2}\right)$$

where *h* defines the convection heat transfer coefficient, T_amb is the ambient temperature, \sigma is the Stefan-Boltzmann constant, \varepsilon is the material emissivity, \alpha is the material absorption coefficient, P is the laser power, R_b is the beam radius and r is the distance between the laser position and material point of interest.

GAMMA uses an explicit time integration formulation to solve the heat equation within the solid part. It allows an unstructured mesh representation for complex geometries. An effective heat capacitance model is used to capture the effects of the latent heat of melting and solidification which is resolved through c_{p,eff} in Equation 14; this heat capacitance may be based on handbook material values, or may come from more detailed specifications (e.g., using Thermo-Calc software to determine the enthalpy and specific heat as a function of temperature for a given material). Prior work has been done to compare temperature histories and thermal fluxes using handbook material values and Thermo-Calc software predictions for enthalpy and specific heat as a function of temperature [3]; from this it has been shown that the nonlinear material properties predicted by Thermo-Calc predicting a much larger solidification time and smaller peak temperature than handbook material values of the same material.

The GAMMA code is written in C++, and has been successfully installed on Linux, Windows, and Mac systems. Early work on the serial version of GAMMA demonstrated a simulation time for a specific simulation that was around 1000 times faster than a commercial code. Much of this speed-up is attributed to the use of an explicit integration scheme. GAMMA has been parallelized using MPI for use on distributed memory systems, giving further speedup. Recent extension of GAMMA to run on Graphical Processing Units (GPUs) have yielded a demonstrated 85x speedup compared with the serial version.

The primary output of GAMMA is the temperature as a function of space and time throughout the part during the build process. This further allows the computation of fields such as the temperature gradient and the cooling rate. These fields can in turn be used together with analytical models, empirical correlations, detailed ICME calculations, or surrogate models (such as those developed in the current project) to predict material quality, microstructure, and properties at locations of interest in an AM-built part. A sample workflow for predicting temperature and microstructure for the cruciform geometry is shown in Figure 20.

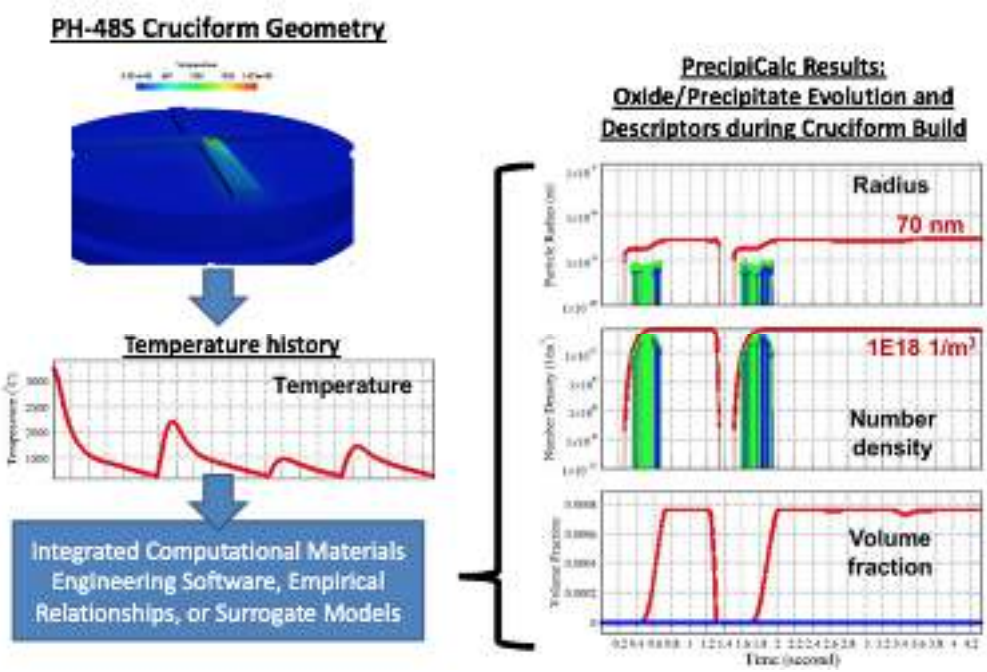

Figure 20: Workflow linking GAMMA thermal simulation through ICME software to predict material microstructure and properties.

As part of the current project, GAMMA has been integrated into a Virtual Certification Framework driven by the Siemens NX software. NX has the capability to generate mesh and toolpath files that can be directly used as inputs to GAMMA. A graphical user interface (GUI) in NX allows efficient input of model

and solution parameters, which are used to populate the GAMMA input file; the GAMMA executable can then be launched within NX. Computed fields such as the temperature and the solidification rate can be output directly to unstructured mesh data files, or can be interpolated using the voxel data structure implemented through the VoxelCode software for visualization within NX. Finally, the output data can be post-processed to yield inputs for other simulations. For example, the computed solidification cooling rate at each location in the part may be used to predict the yield strength through data-driven surrogate models, allowing a solid-mechanics simulation for prediction of failure under a given set of load conditions.

D. Verification of the GAMMA simulations

Collaborating with Task 5 in this project, a series of additive manufacturing experiments were conducted by Northern Illinois University in order to be used as a validation and verification tool for our thermal simulations. The verification process involves comparison of the experimental thermal histories of a few points, that are measured by some thermocouples placed on the top surface of the substrate, with the simulation results and also calibration of the uncertain simulation parameters to achieve a better a correspondence with the experiment. These uncertain simulation parameters include absorptivity of the laser power, heat convection coefficient and radiative emissivity of the manufactured part. The experiments that were used for verification of GAMMA are **a)** Half-Charpy build and **b)** Cruciform build. For the detailed description of these experiments, the reader is referred to the Task 5 section of this document. We tried to closely emulate different features of experimental environment, such as boundary conditions and variable ambient temperatures, in our simulations in order to minimize the possibility of differing from the experimental results.

a) Half-Charpy experiment

Figure 21. shows the comparison between simulation and experimental results for one of the probe points before doing any calibration on the simulation parameters.

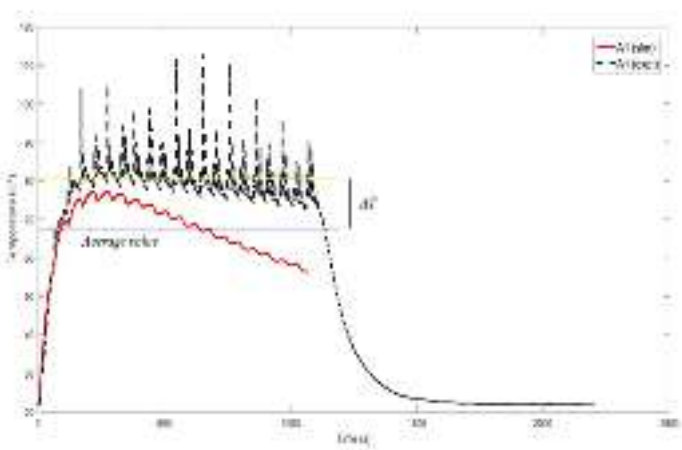

Figure 21: comparison of GAMMA and experimental results for a probe point before calibration

In these experiments the base of the substrate is in contact with flowing water (a calorimeter) that acts as a heat convection boundary condition in the simulation. Other boundary conditions capture heat loss through heat convection by the surrounding air and radiation to the environment. Furthermore, only a fraction of the laser power is absorbed by the built part and the rest is either taken away by the blown powder or gets radiated away. So, a non-dimensional fraction known as laser absorptivity is defined in simulations of additive manufacturing that accounts for the loss of laser power. Because there is an

uncertainty about the exact value of the convection coefficients, radiative emissivity and absorptivity, calibration has to be performed to find the true values of theses parameters based on the experiment. The convection coefficient of air was excluded from the set of calibration parameters. Figure 22 shows the rather high sensitivity of the simulation results to the value of the water convection coefficient at the base. The calibration method involves running GAMMA for a set of Design of Experiment (DOE) and varying the calibration parameters in each simulation and then performing a Gaussian Process Metamodeling. The metamodel is constructed in such a way that it minimizes the difference between the experimental and simulation data. This difference is defined as the difference between the time-average of the experimental and simulation results and it has been depicted as ΔTin Figure 21. Figure 23. shows the response surface of ***J*** (goal function of metamodel) versus ***h*** (convection coefficient), ***epsilon*** (radiative emissivity) and ***alpha*** (laser absorptivity). Here, ***J*** is a function that collectively accounts for all of the thermocouples in the experiment. The ultimate goal is locate the minimum of ***J*** and thereby the true values of the uncertain parameters.

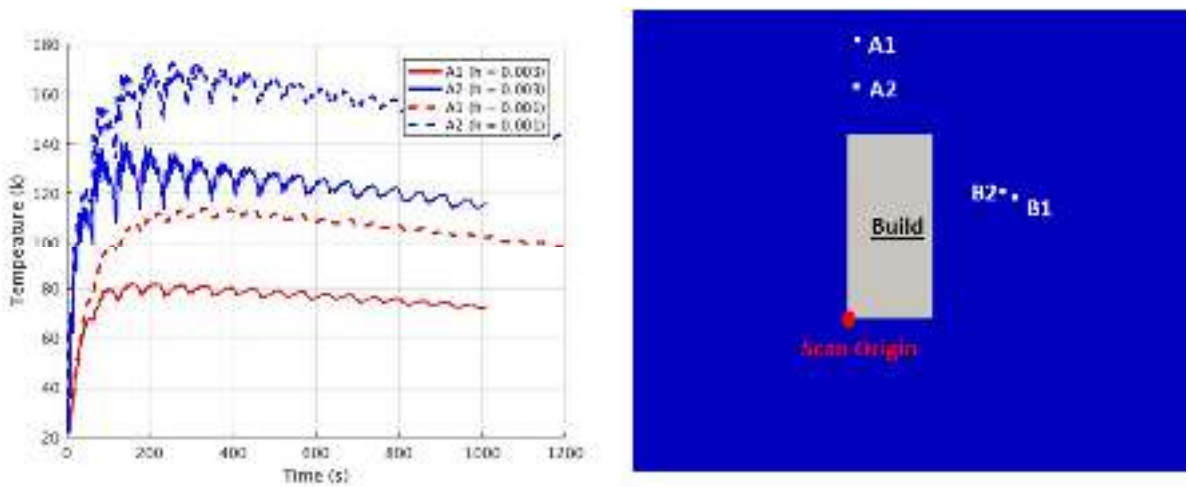

Figure 22: high sensitivity of results toward water convection coefficient, the image on the right shows the relative position of the thermocouples on the substrate

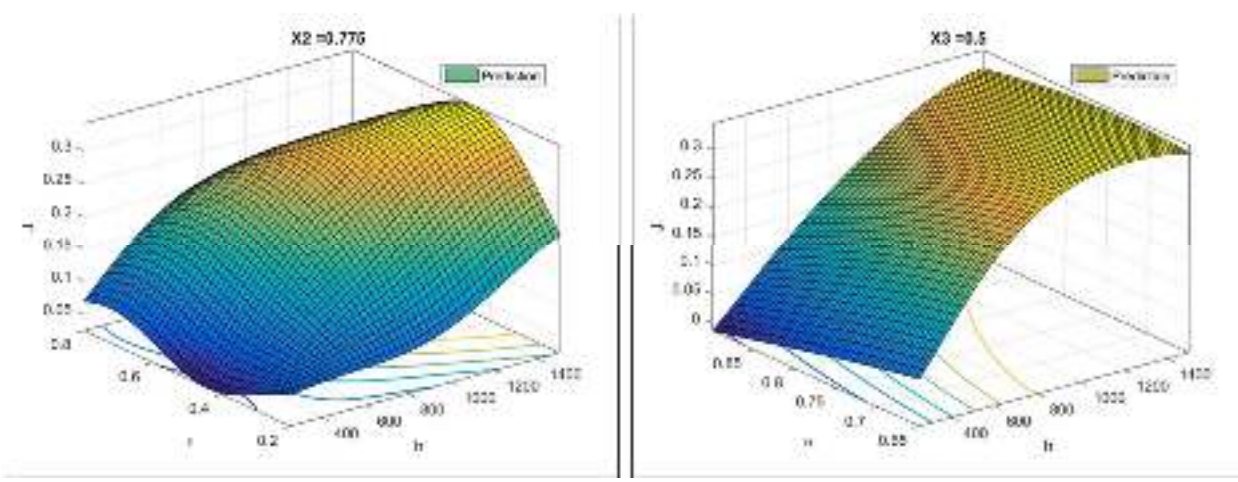

Figure 23: Response surface of the calibration cost function ***J***

Having done the calibration, it was found that the GAMMA results could be improved by lowering the convection coefficient, increasing the absorptivity and decreasing the radiative emissivity. Table 5. shows the calibrated set of parameters that yield the best match with the experiment and Figure 24 demonstrates the data comparison following the calibration.

Table 5: Calibration results

$h\ (\frac{W}{m^2K})$	α	ε	*Flaw*
250	0.8	0.8	Unrealistic *h*
500	0.85	0.2	Unrealistic ε
350	0.8	0.5	Small *h*

Apparently, a better match in terms of a smaller difference between the two plots has been achieved in Figure 24, but there are certain shortcomings with the overall method. First, the final calibrated values have turned out to be unrealistic in a physical sense. For example, getting a convection coefficient of 250 (W/m^2.K) for moving water is not consistent with reality because it is much smaller than expected value which is above 2000 (W/m^2.K). Second, we are not still able to match the high peaks observed in the experiment. Third, the slope of the GAMMA results is not quite the same as that of the experimental results. It was later discovered that the slope of the simulation curve is a direct function of the ambient temperature, in the sense that if it is assumed that the ambient temperature of the experiment rises with a ramp through time, the simulation curve also rises in the same manner. (Figure 25) However, the measured ambient temperature data by NIU which is shown in Figure 26, does not show much of a ramp-up with time.

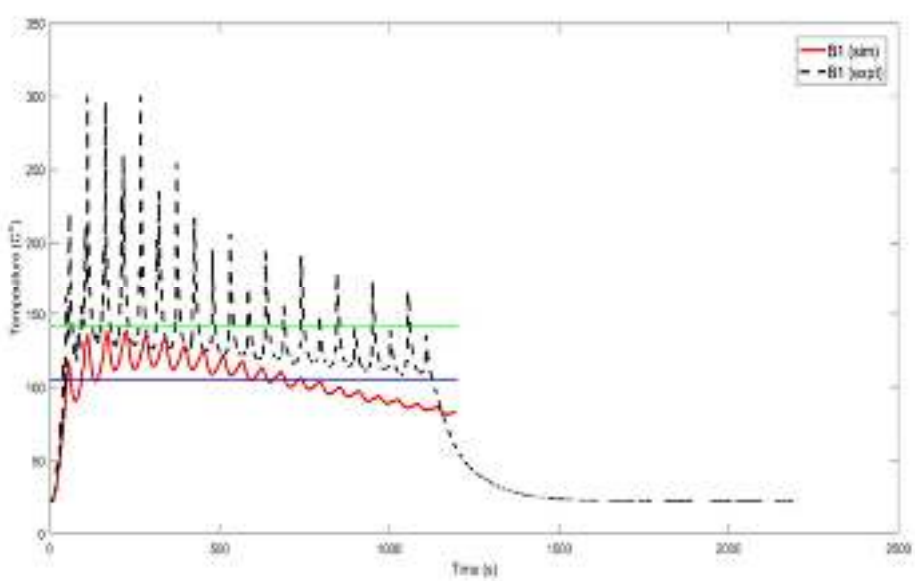

Figure 24. Comparing experimental and simulation results for one thermocouple after calibration

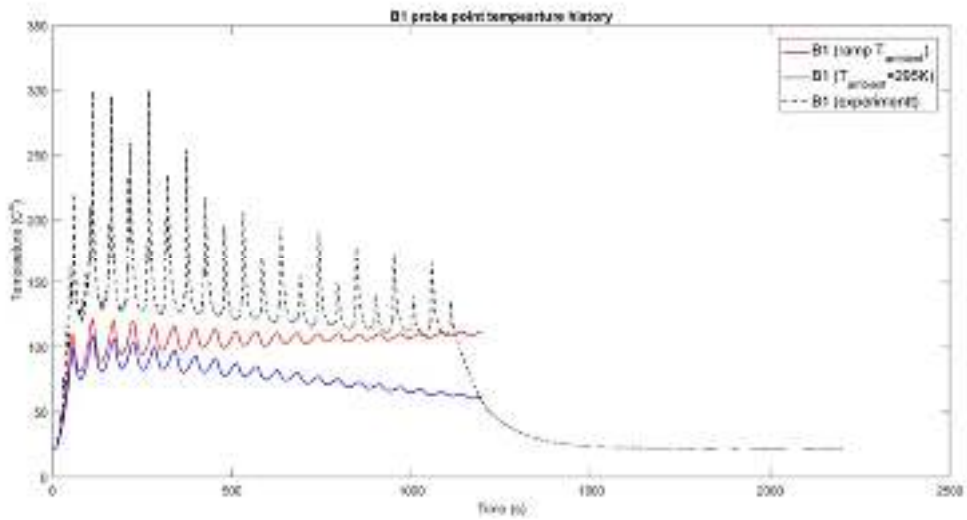

Figure 25. Simulation result by assuming that the ambient temperature ramps up

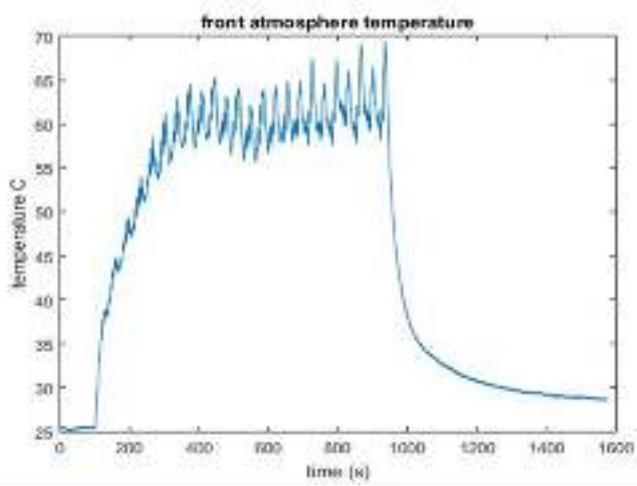

Figure 26. Measured variable ambient temperature during experiment by NIU

Finally, we tested effects of considering the heat radiation from the sides of the build on to the surface of the substrate where the thermocouples are placed because this extra incident energy might play a role in the large peaks that we see in the experimental data. Figure 27 shows the results of GAMMA after including the lateral radiation and the insignificant overall contribution that it has on the temperature history. Therefore, it was ruled out as a major factor.

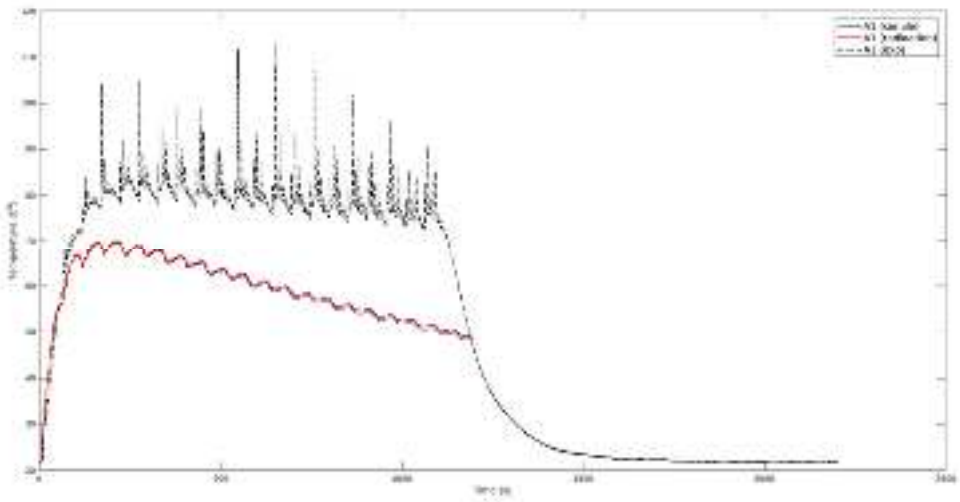

Figure 27. Comparing GAMMA results before and after including radiation from side

A second experiment was done by Task 5 again building the half-Charpy with slightly different process parameters and thermocouple positions. A better match with the experiment was achieved with GAMMA in this case. Figure 28 and Figure 29 present the obtained results for two thermocouples. According to Figure 26, the ambient temperature gradually rises with time. For the verification against this experiment, it was once assumed that the ambient temperature remains constant at 60 C and another time it was supposed to be changing according to Figure 26. No calibration was done for this experiment.

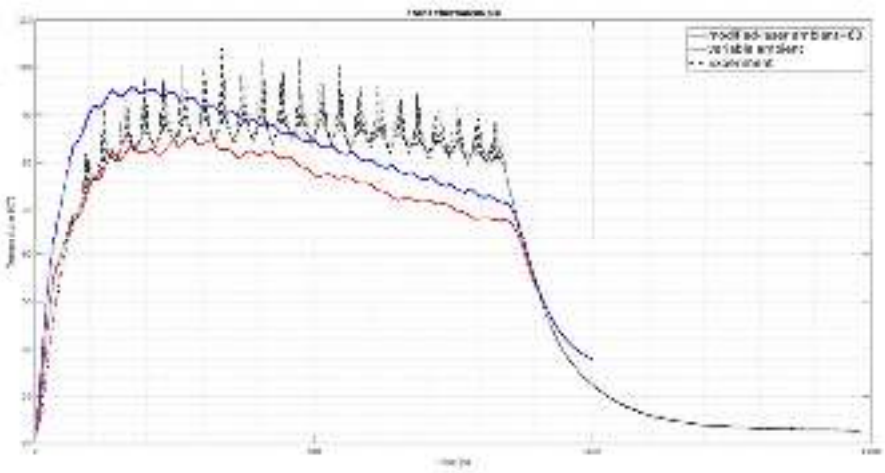

Figure 28. Front thermocouple temperature history with constant and varying ambient temperatures (GAMMA vs Experiment)

.

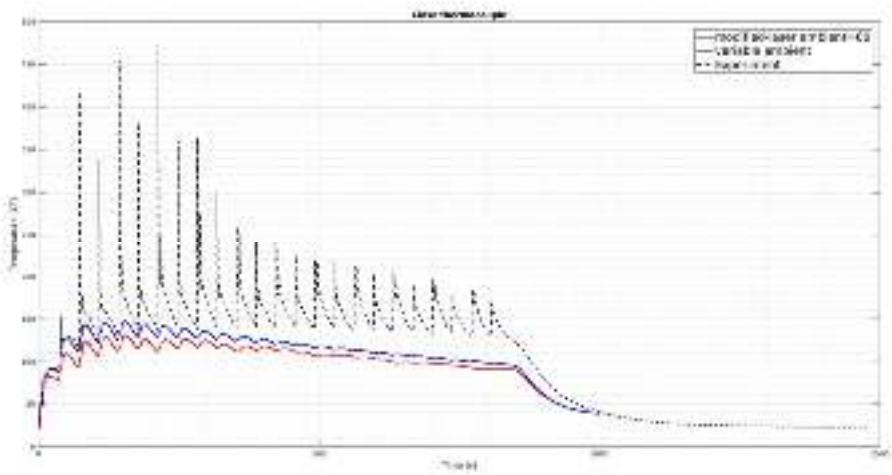

Figure 29. Close thermocouple temperature history with constant and varying ambient temperatures (GAMMA vs Experiment)

b) Cruciform experiment

The final verification experiment was conducted on a tangential cruciform geometry (Task 5, page 93). The experimented lasted for over seven hours under same boundary conditions and experiment setup as the half-Charpy experiment. Figure 30 shows the comparison results between simulation and experiment for one of the thermocouples. The sudden rise of temperature in the experimental results was due to some malfunction in the operating device.

After much deliberation on the outcome of these simulations and experiments, we are fairly confident that the observed discrepancies, in terms of both temperature magnitude and evolution pattern, are caused by the significant uncertainties over the real nature of the boundary condition underneath the base. This is because there is absolutely no knowledge about the water flow and the manner of heat convection at this location which has a considerable effect the overall results.

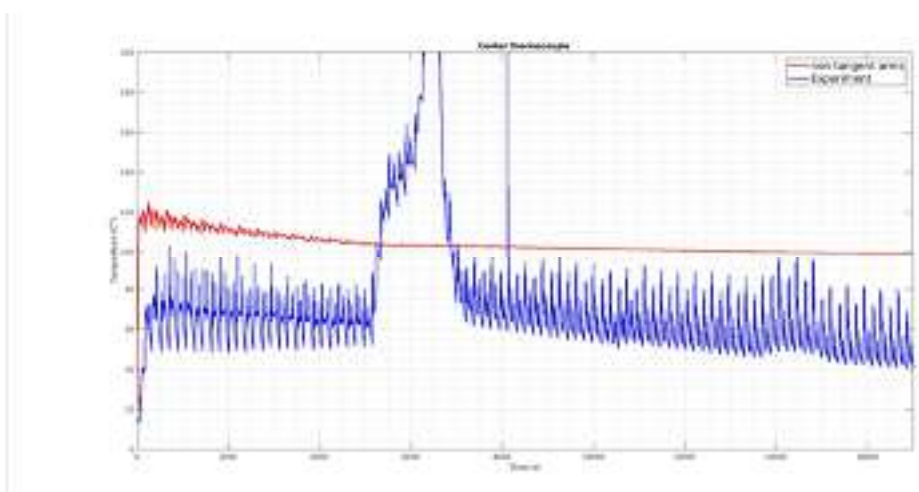

Figure 30. Comparing simulation (red) with experiment (blue) in cruciform experiment

Reference (Task 2)

1. Lindgren, Lars-Erik, Henrik Runnemalm, and Mats O. Näsström. "Simulation of multipass welding of a thick plate." *International journal for numerical methods in engineering* 44.9 (1999): 1301-1316.

2. Lindgren, Lars-Erik, and Erika Hedblom. "Modelling of addition of filler material in large deformation analysis of multipass welding" *Communications in numerical methods in engineering* 17.9 (2001): 647-657.

3. Smith, J., Xiong, W., Cao, J., & Liu, W. K. (2016). Thermodynamically consistent microstructure prediction of additively manufactured materials. *Computational mechanics*, *57*(3), 359-370.

Task 3: Certification Methodology

A. Identification of Processing-Structure-Property Relationship Flow

We established a general processing-structure-property relationship flow (Figure 31) for validating microstructural material models in the manufacturing process. We chose to demonstrate our certification methodology using investment casting of a step plate as an example. The process simulations in this flow was specific to casting, but the structure-property relationship flow was generalized to additive manufacturing as well. The simulation models of processing-structure and structure-property are provided by PDA and QuesTek, respectively.

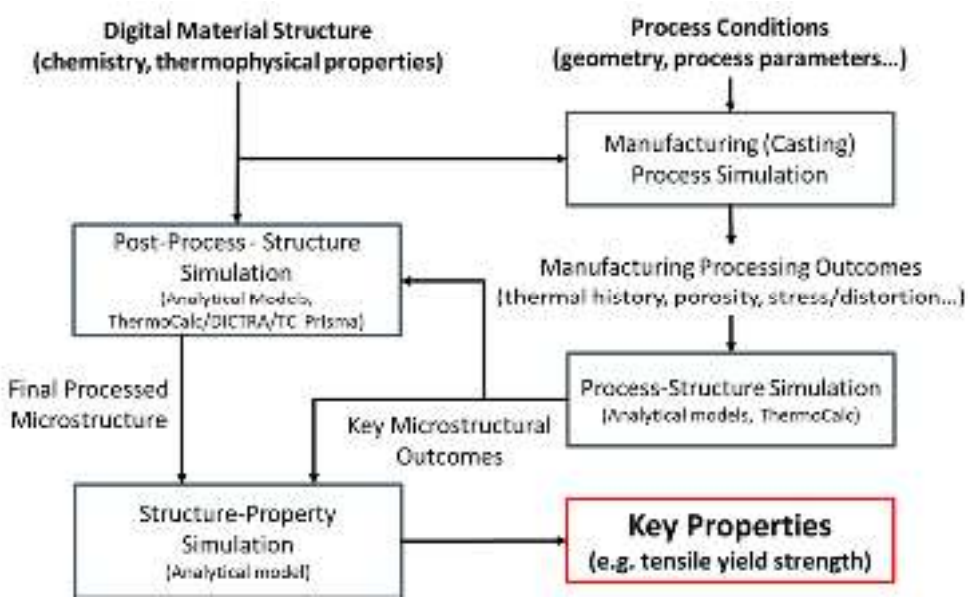

Figure 31: General flow of the process-structure-property relationship

Surrogate models, or metamodels, were trained by Northwestern for each of the components in the flow, utilizing the Design of Experiments and Gaussian random process models described in the next sections.

B. Development of Optimal Latin Hypercube Sampling and Visualization Package

Optimal Latin hypercube sampling (OLHS) is a Design of Experiments (DoE) method that was developed by Northwestern, allowing for the automatic generation of training data inputs that span the

desired metamodel space as optimally and uniformly as possible. Any number of input variables and number of samples can be specified. The OLHS can then be used as inputs in physics-based simulations; the set of inputs and outputs are the training data for the metamodel.

The OLHS package and a tool to visualize the samples in either 2D or 3D space (choosing 2 or 3 of the input variables at a time) were integrated into Siemens NX (see details under Task 4). Figure 32 show examples of the visualization tool for the DoE generated for the casting process metamodel (see later section).

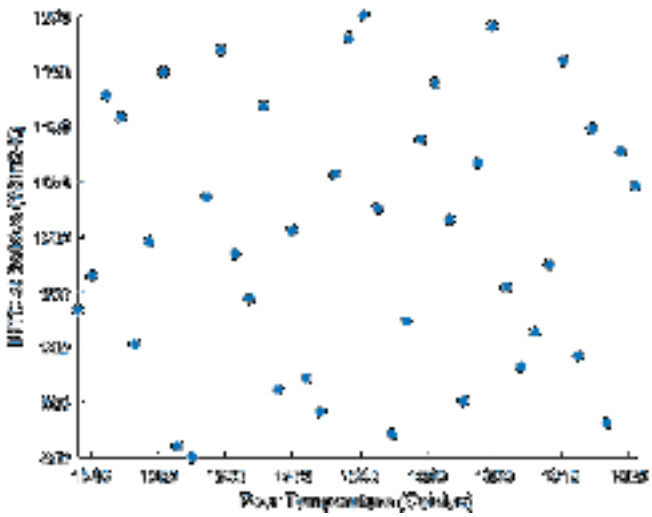

(a)

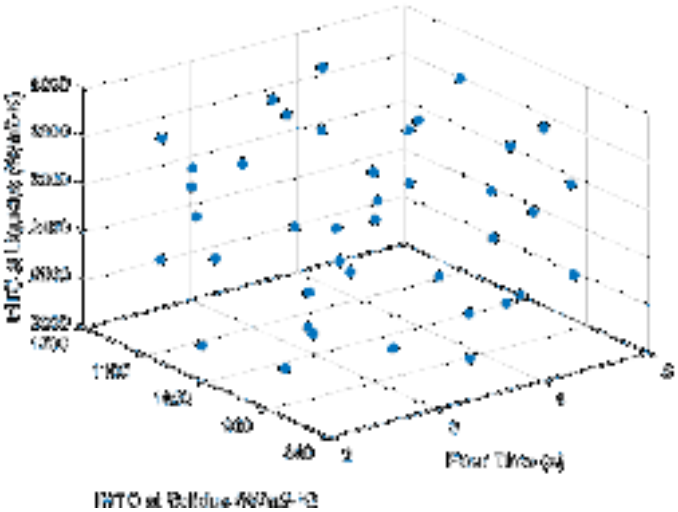

(b)

Figure 32: Visualization of DoE samples generated by OLHS in 2D (a) and 3D (b) for the casting process metamodel

C. Development of Gaussian Process Metamodeling and Visualization Package

Northwestern developed a software package for efficient and accurate response surface modeling with Gaussian random processes. Our package is applicable to multi-dimensional and multi-response datasets and can also automatically handle noisy observations once enough training data is provided. Our Gaussian process (GP) metamodel can replace expensive computer simulators and subsequently speed up the design and analysis process. Additionally, the package is accompanied with a visualization tool that allows to conveniently investigate the input-output relations regardless of the problem dimensionality.

This package was integrated into Siemens NX software (see Task 4), as well as used to replace expensive physics-based models (as shown in the next few sections). For figures of the visualization tool, please see the following sections detailing the GP metamodels trained for this project.

D. GP Metamodeling for Investment Casting

Experimental and simulated data of investment casting of step plates (Figure 33) was used to develop fast metamodels.

Figure 33: Metal investment casting of step plates, provided by PDA

a. Automatic Extraction of Solidification Cooling Rate

Using MAGMAsoft, PDA obtained simulated thermocouple data from 12 locations on a step plate, in the form of temperature vs. time. A code was written by Northwestern to automatically regress a linear line between the solidus and liquidus temperatures, and the solidification cooling rate (SCR) was extracted as the slope of this line.

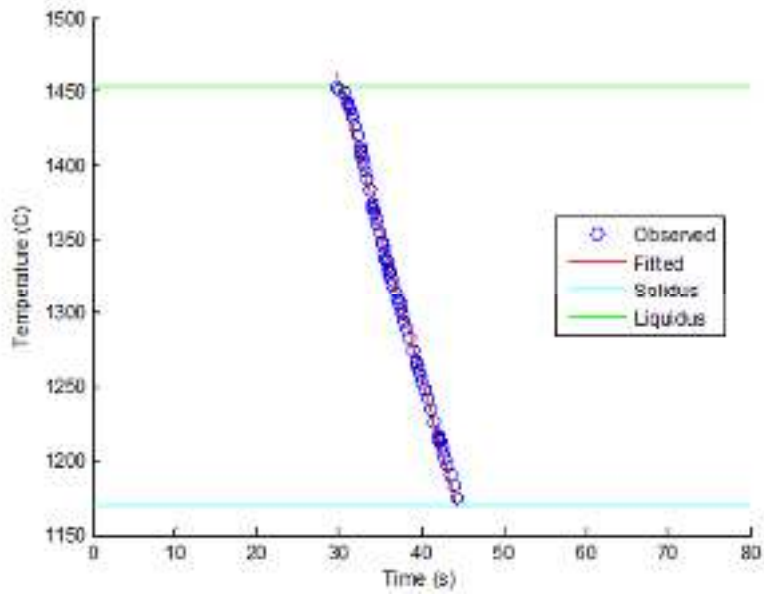

Figure 34: Automatic extraction of solidification cooling rate from casting process simulation data

b. Process Metamodel

Firstly, an OLHS DoE was made by Northwestern for PDA with 4 inputs (pour time, pour temperature, interfacial heat transfer coefficient (IHTC) at liquidus, and IHTC at solidus). A total of 40 samples were generated, and a MAGMAsoft simulation run for each by PDA (taking close to 2 months). An example of the simulation result is shown in Figure 36. The SCR was extracted from each simulation output with the aforementioned method.

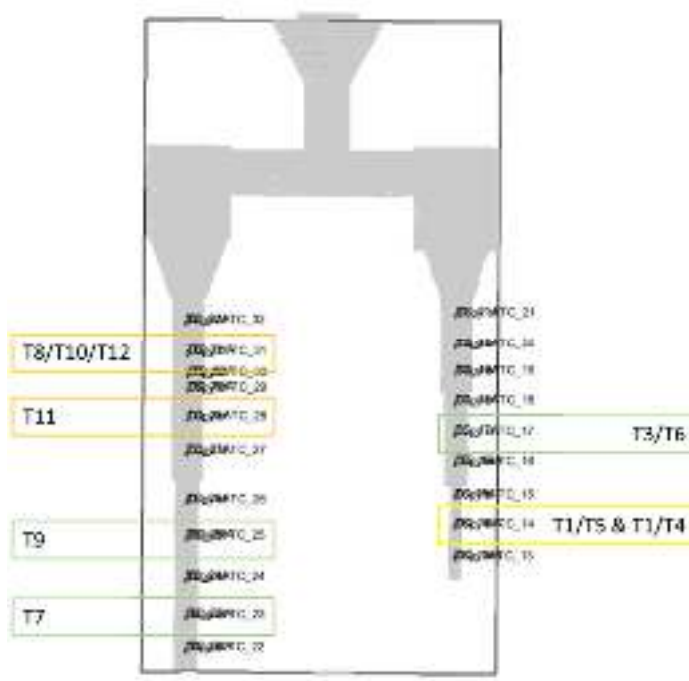

Figure 35: Locations and labels of the 12 thermocouples on the step plate

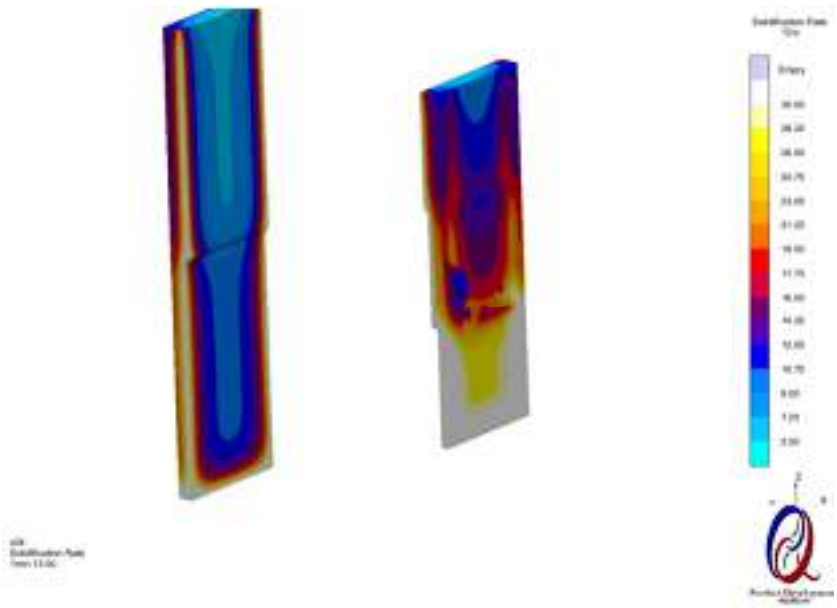

Figure 36: MAGMAsoft thermal simulation of the step plate

For each of the 12 simulated thermocouple locations on the step plate, a GP metamodel was fitted, relating the pour conditions to the SCR. Now, instead of running the expensive simulations, the SCR can be predicted in fractions of a second.

To validate the metamodels, the leave-one-out cross validation (LOOCV) errors were calculated using an analytical equation that can be derived for Gaussian random process models. The LOOCV errors of the 12 location-specific metamodels range from 0.022 to 0.079, which are considered reasonably low errors.

By selecting two input variables at a time and holding all others at their mean values, response surfaces (Figure 37) can be plotted to visualize the relationship between the two chosen variables, as well as the 95% prediction interval (PI), a measure of the uncertainty of the model. The 95% PI are plotted as surfaces, along with the mean prediction. PI surfaces that are “closer” to the mean surface means smaller uncertainty -- and thus can be a visual validation of the metamodel.

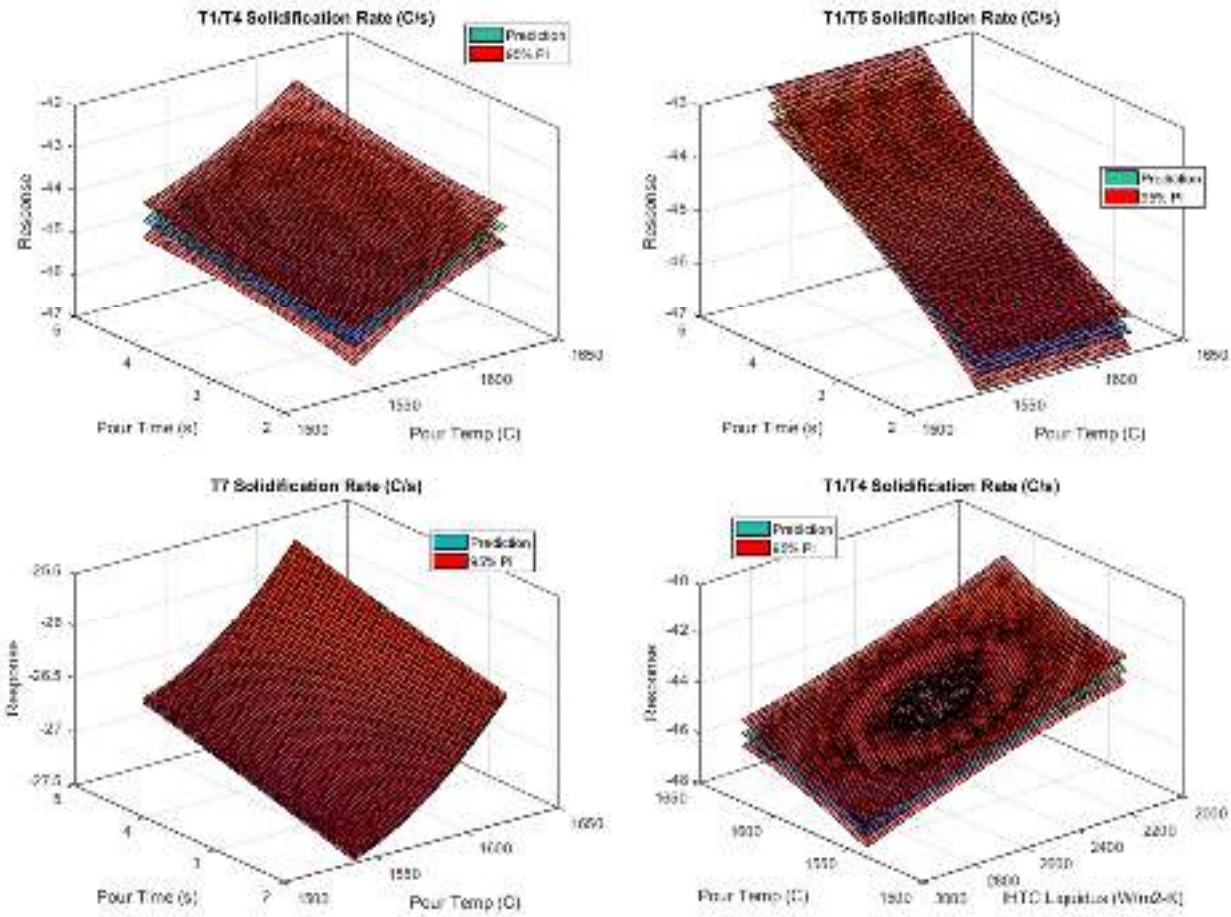

Figure 37: Selected response surfaces of the casting process metamodels. The response plotted on the Z-axis is the solidification cooling rate (SCR)

c. Global Sensitivity Analysis

Moreover, using the fast prediction of the casting processing metamodels, we were able to perform Sobol Sensitivity Analysis to uncover which of the input variables have the most impact on the SCR. For the step plate locations shown in Figure 35, the Sobol indices are shown in Figure 38. Here we see clearly that IHTC at solidus contributes more significantly to SCR than the other parameters (a higher index is regarded as higher significance). Furthermore, the main indices and total indices are nearly equal everywhere, meaning that there is almost no interaction effect between parameters.

Figure 38: Sobol indices (y-axis) of four locations on the step plate

d. Microstructure Homogenization Metamodel

NU, PDA, and QuesTek worked together to identify the scope and flow of the procedure to replace of post-processing-structure simulation (DICTRA) with much faster GP metamodels. The metamodel inputs are secondary dendrite arm spacing (SDAS), compositions of Ni and Co, and homogenization temperature; the output is minimum homogenization time required (with log transformation to achieve better fit during training). DICTRA simulations were run with long enough holding time during homogenization.

We generated 40 OLHS samples for running DICTRA segregation and homogenization simulations. A large range (10-10,000K/s) of the solidification cooling rate (input of the segregation simulation) was used so that the model is applicable for both casting and additive manufacturing processes. The metamodel also combines both the process-structure (as-built segregation) and post-process-structure (homogenization) DICTRA simulations. The LOOCV error of this model is small, 0.0168.

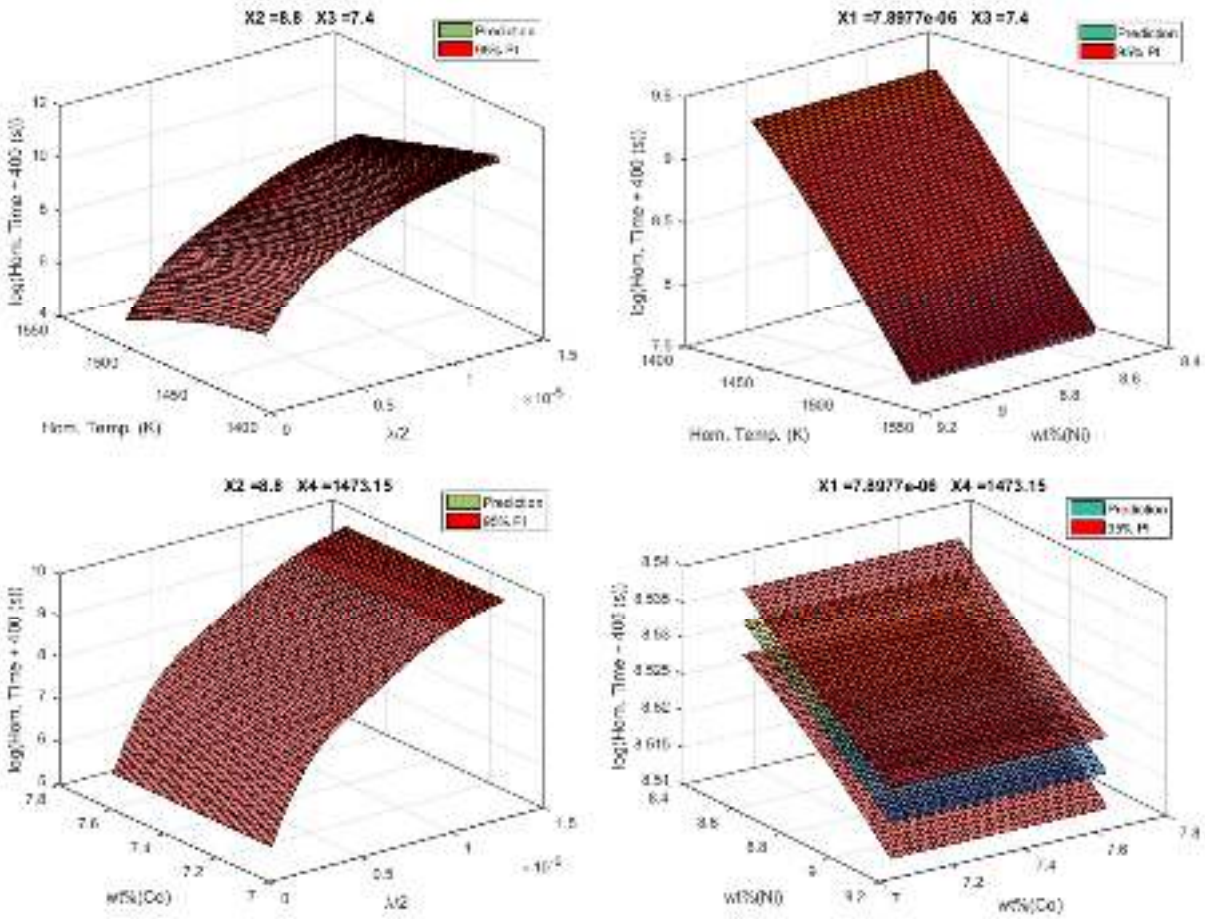

Figure 39: Selected response surfaces of the casting homogenization metamodel. *The titles show the values of the inputs that were held constant. (X1: secondary dendrite arm spacing; X2: wt%(Ni); X3: wt%(Co); X4: homogenization temperature)*

Finally, using the roughness hyperparameters ω of the GP metamodel, we can get a sense of the impact of each input on the response, i.e., if the hyperparameter is high, then the corresponding input causes more variation in the response. Here, the SDAS drives the required homogenization time with ω = 4.242; the next most significance input is the homogenization temperature with ω = 0.195, a much lower value.

e. Validation of Homogenization Metamodel

In addition, the process-structure metamodel was linked to the casting process metamodel, which has solidification rate as a response. Using an analytical equation developed by PDA and QuesTek through experiments (Table 6, Figure 40), the solidification rate response is converted into SDAS, which is then used as an input to the microstructure metamodel. With this linkage, the minimum required homogenization time for the step-plate casting part can be quickly predicted based on the process parameters (pour time and pour temperature).

Table 6: Experimental values for cylindrical casting samples

Sample	Cooling rate (°C/sec)	Dendrite arm spacing (μm)
0.25" RD	3.50	40 μm
3" RD	0.67	68 μm
5" RD	0.40	80 μm
Fastest cooling region from 200 pound component	0.20	100 μm
Slowest cooling region from a 200 pound component	0.05	150 μm

Figure 40: As-cast grain structure for step plate (SDAS)

To validate the above, the required homogenization time was predicted directly from MAGMAsoft thermal results for H13 die steel poured at 1538°C over 5 seconds by PDA (Figure 41). The results show that a maximum of nearly 12 hours was needed for homogenizing the entire step plate, which agrees with QuesTek's experimental assessment that more than 8 hours (28,800 seconds) was needed for sufficient total homogenization.

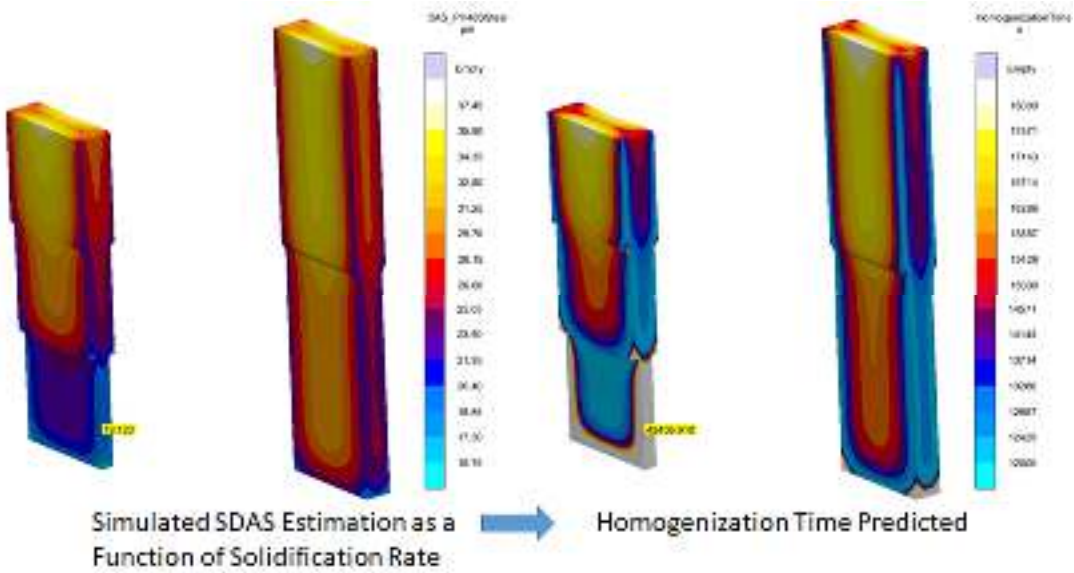

Figure 41: Homogenization time prediction using metamodeling and analytical SDAS calculation, directly from MAGMAsoft thermal history results

f. Demonstration of Process Optimization

Additionally, automated optimal design of the process parameters was demonstrated using the integrated metamodels. In the case study, the casting process conditions were optimized such that the longest homogenization time out of the 12 locations was minimized (the upper left location in Figure 42). The optimized parameters are shown in Table 7.

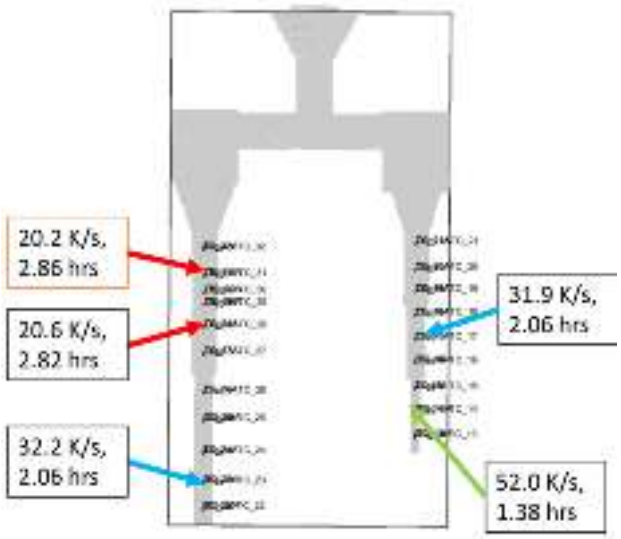

Figure 42: Predicted solidification cooling rates and required homogenization times for the optimized process conditions

Table 7: Optimized casting process conditions for minimum homogenization time

Optimal Parameters:

Hom. Time (hrs)	**2.86**
Pour Temp. (C)	1538
Pour Time (s)	2
IHTC at Solidus	1200
IHTC at Liquidus	3000

E. GP Metamodeling for Microstructure Simulations

a. Precipitation and Solid Solution Strengthening Metamodels

In the area of integrating processing-structure-property models, a set of OLHS DoE with 8 inputs and 300 samples were generated and provided to QuesTek for precipitation aging simulations. The eight (8) inputs are aging temperature, aging time, and composition weight percentages of Co, Cr, Mo, Ni, Ti, and Al. Based on the PrecipiCalc simulation results, the yield strength contributions from precipitation and solid state hardening were found. Two GP metamodels were fitted separately for precipitation and solid solution strengthening, with very low LOOCV errors 1.15e-4 and 4.52e-5, respectively.

Again, the roughness hyperparameters ω of the metamodels serve as an approximate sensitivity analysis. For precipitation strengthening, the inputs from greatest to least values of ω (most significant to least) are: aging temperature, Al, aging time, Ti, Ni, Co, Cr and Mo. For solid

solution strengthening, the order is: aging temperature, Mo, aging time, Ni, Al, Ti, Cr and Co. These relationships can also be seen in the response surfaces below.

Table 8: Inputs of the precipitation and solid solution strengthening metamodels

Inputs	
X1	Co (wt%)
X2	Cr (wt%)
X3	Ni (wt%)
X4	Ti (wt%)
X5	Al (wt%)
X6	Mo (wt%)
X7	Temp (°C)
X8	Time (s)

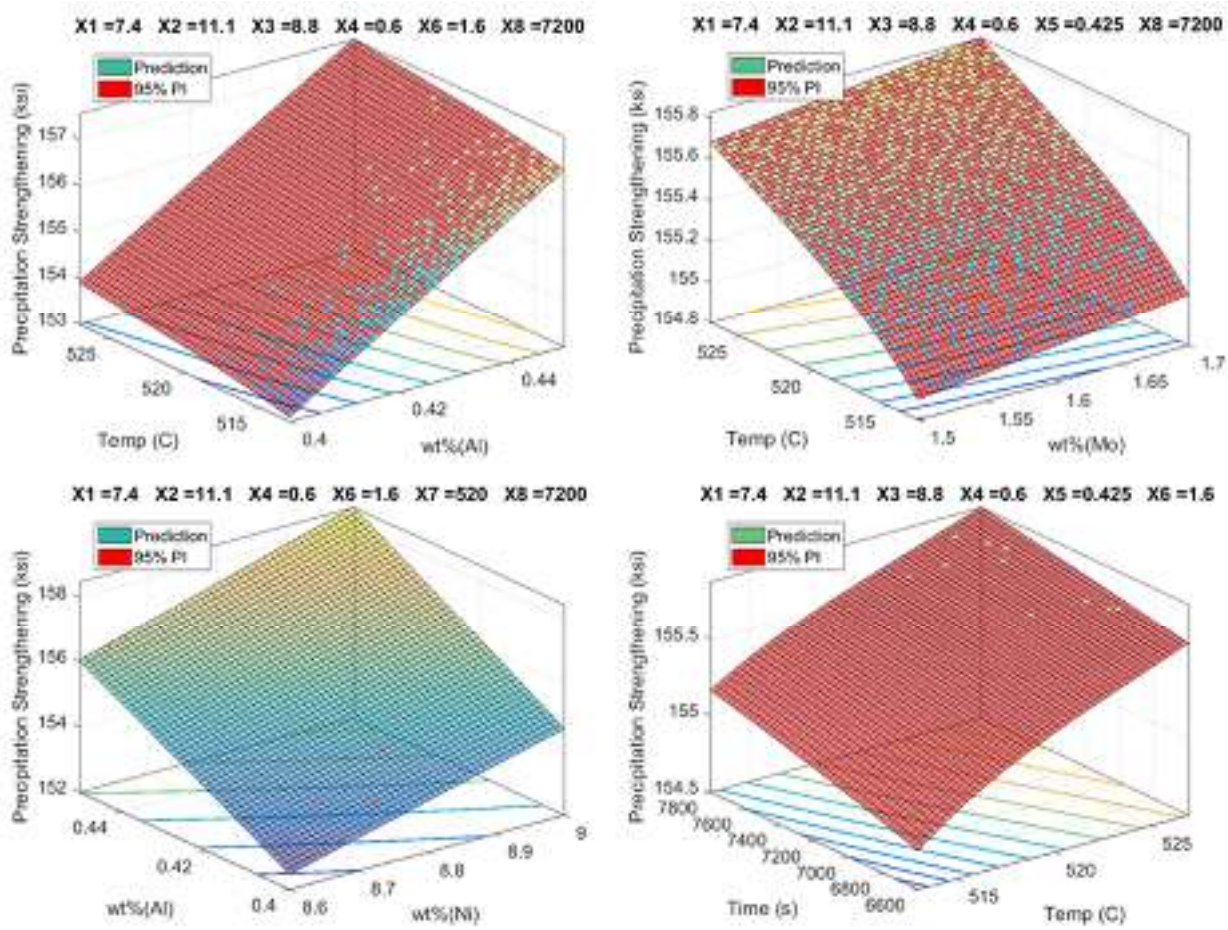

Figure 43: Selected response surfaces of the precipitation strengthening metamodel. *The title shows the values of the inputs that were held constant. Please refer to Table 8 for the physics-based names of X1 through X8.*

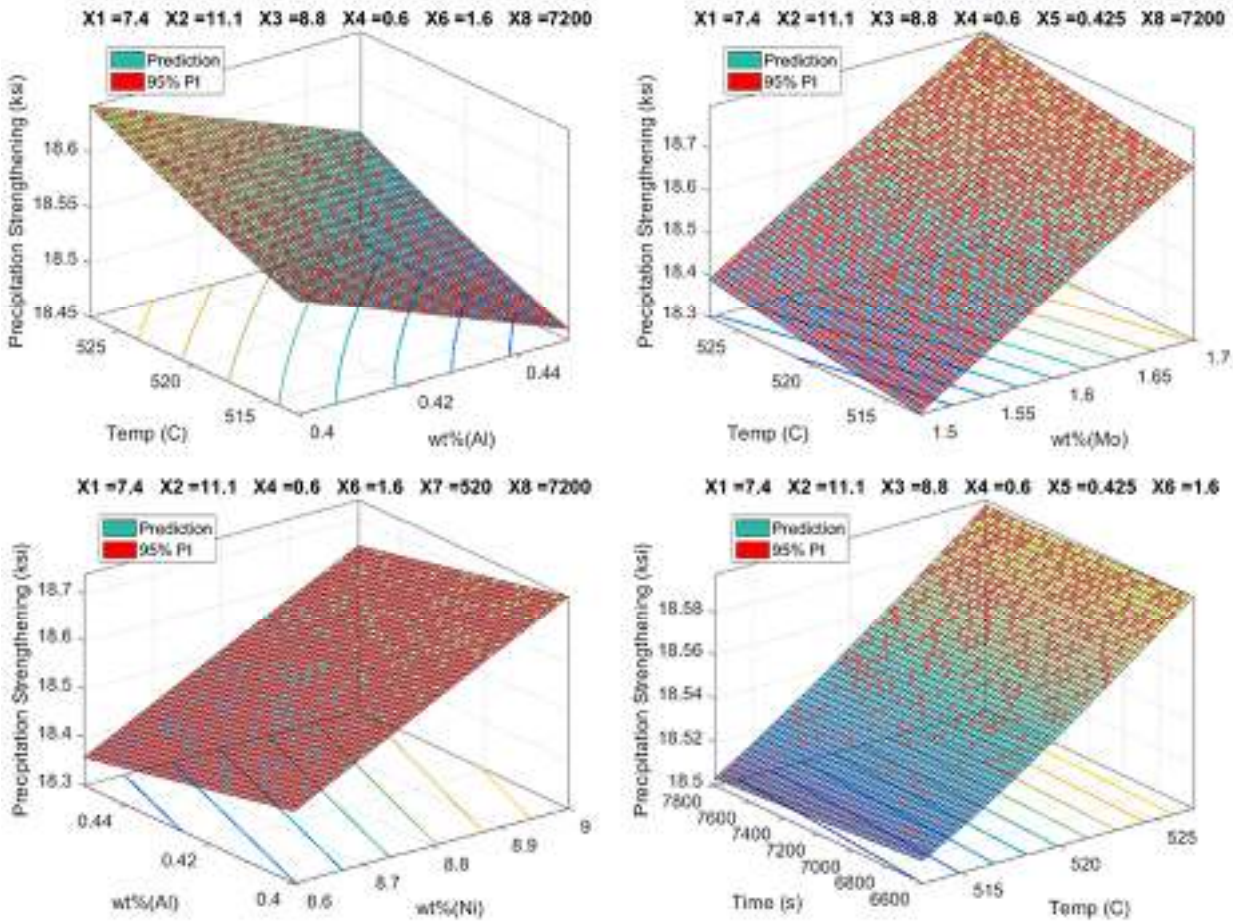

Figure 44: Selected response surfaces of the solid solution strengthening metamodel. *The title shows the values of the inputs that were held constant. Please refer to Table 8 for the physics-based names of X1 through X8.*

b. Oxide Evolution Metamodel

To find the Hall-Petch stresses that contribute to tensile yield strength, two groups at Northwestern collaborated to identify the simulation and metamodeling flow. First, a metamodel was fitted to calibrate interfacial energy in PrecipiCalc as follows. Prof. Wei Chen's group generated 100 samples using OLHS with 3 inputs (solidification cooling rate, and X- and Y-intercepts of the temperature-dependent interfacial energy). Prof. Greg Olson's group used the OLHS and PrecipiCalc to calculate the outputs of the metamodel, mean oxide particle radius (R) and total number density (Nv) (see more descriptions under Task 1).

To calibrate PrecipiCalc, a code was written to back-calculate the fixed intercepts of interfacial energy given a set of known experimental outputs (R, Nv). However, since the experimental values of cooling rate corresponding to the set of R and Nv are not known and difficult to measure, the method using inverse optimization was ill-posed and suffered from many possible solutions for interfacial energy. Another method involving Bayesian calibration using simulation and experimental results for both LENS and casting was considered, however, was also not possible due to the difficulties obtaining experimental cooling rates for LENS samples and resolving PrecipiCalc simulations for casting.

Thus, finally, we gathered several values from existing literature and found an approximate linear relationship between temperature and interfacial energy. A DoE of 160 optimal Latin hypercube samples with 8 inputs (solidification cooling rate, and weight percentages of Ni, Ti, Al, Co, Cr, Mo, O) was created. From PrecipiCalc simulations using the fixed temperature-dependent interfacial energy, a metamodel of these inputs and outputs (mean oxide particle radius and number density) will be fitted.

c. Framework for Total Yield Strength

Northwestern and QuesTek finalized the procedure to chain together the precipitation strengthening, solid solution strengthening and oxide distribution metamodels to obtain the final total yield strength metamodel as shown in Figure 45.

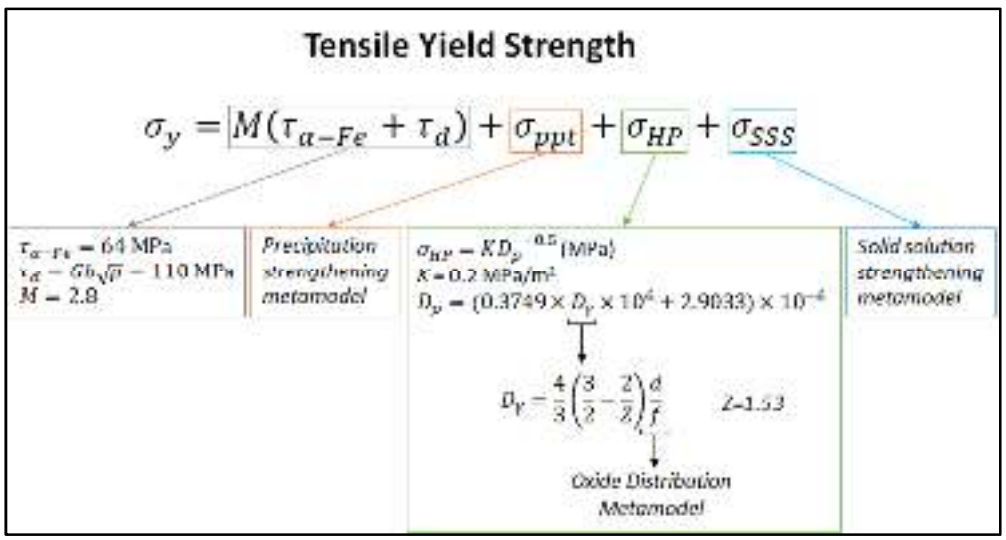

Figure 45: The final structure-property metamodeling flow to obtain tensile yield strength

F. Statistical Characterization and Analysis of Porosity in Additive Manufacturing Process

To relate processing parameters to the porosity of additively manufactured parts, image processing, 3D microstructural voids characterization and statistical analysis were developed by Northwestern. The methods were then performed on SS316L half-charpy and Inconel thin wall samples built using DED-LENS.

a. Image Processing

Using X-ray computed tomography (XCT), 2D cross-sectional images of the experimental samples were acquired, and the complete volumetric representation was obtained by stacking the 2D slices. However, the images are rotated with unwanted borders around the actual sample, grayscale and often contain noise and edge effects. Therefore, a procedure was developed to clean and binarize the images for the next step, characterization; it is enumerated below and shown in Figure 46.

1. Find the angle of rotation of the image, assuming the sample is rectangular.
2. Remove the background.

3. Detect the biggest square/rectangle. By doing so, it eliminates noise and edge effects that vary between the 2D slices of one volumetric sample.

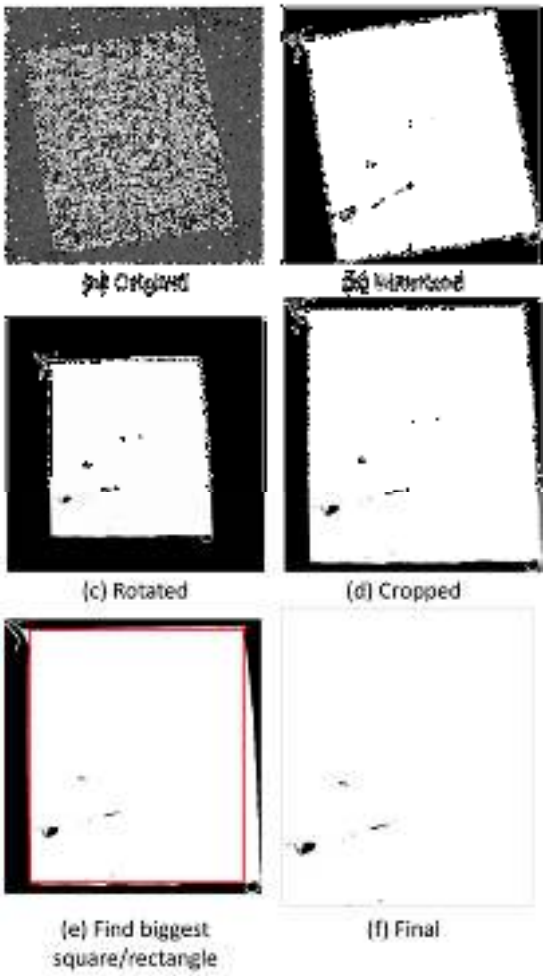

Figure 46: Image processing procedure

XCT sometimes produces images affected with concentric rings (so-called ring artifacts), caused by a minor variation in the response from individual elements in a 2D X-ray detector. These rings complicate the image processing and may be regarded as voids by the characterization program. A ring artifact correction procedure was developed that reduces most of the artifacts (Figure 47).

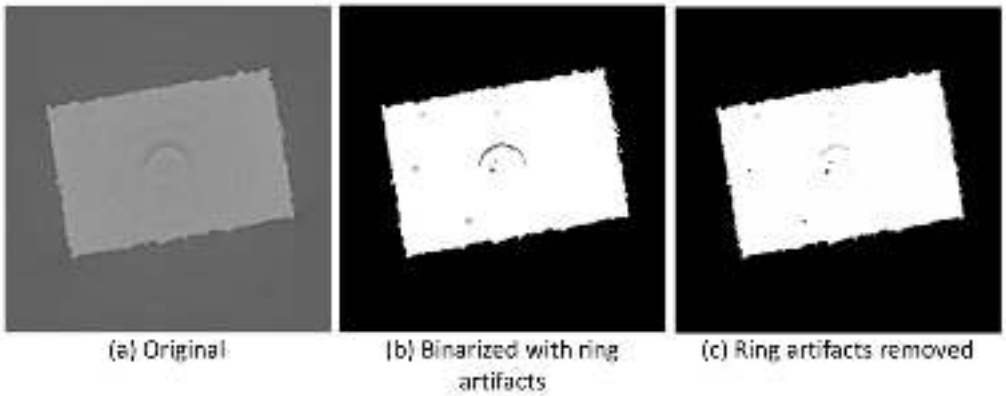

Figure 47: Image with ring artifacts (a), with voids due to porosity shown in red (b). The image after ring artifacts removal (c).

b. 3D Characterization

The open-source software DREAM.3D was used to characterize (quantitatively measure and represent the porosity) for each 3D sample using the processed binary images. The physical descriptors used are the centroids, volume, equivalent diameter, principal axis lengths/directions, aspect ratios and Omega3's of each void within the sample. Also, the number of neighboring voids within a predefined distance are found. This method proved to be successful in characterizing 3D additive manufacturing voids.

c. Effect of Processing Parameters on Porosity

The volume and Omega3 descriptors were averaged for each sample. Along with number of voids, they were related to process parameters using factor analysis. In this method, the input parameters (process) were grouped into different levels, and the standardized effects, main effects and interaction effects of the parameters on the responses (porosity descriptors) were found statistically.

For SS316L Half-Charpies, we had 3D images (set of 1889 2D images) at approximately 13 positions for 4 global process conditions (about 50 3D-images in total). The global process parameters considered were laser power (478W and 645W) and travel speed (5 in/m and 20in/m), as well as the position. The conclusions are summarized below.

- For the three responses (# voids, Omega3 and the volume), Measured Laser Power and its interaction with the position in the Half-Charpy are potentially significant.
- By increasing the laser power, we obtain less porosity; it's the opposite case for the travel speed. There is also a significant decrease of the porosity when moving from the middle of the Half-Charpy to the left back.
- Position within the Half-Charpy had a higher impact on the amount of porosity only for small values of laser power.
- By increasing the laser power and by changing the position from left back to the middle, we obtain higher values of Omega3 i.e. voids close to spheres or ellipsoids. However, the travel speed had not a significant influence on Omega3. Changing the position in the Half-Charpy had a higher impact on Omega3 only for small values of laser power.

- The position in the Half-Charpy and the travel speed had not a significant influence on the volume of the voids. However, by increasing the laser power we obtain smaller voids. Changing the position in the Half-Charpy had a higher impact on the size of the voids only for small values of laser power.

We had 3 Inconel thin walls built with different dwell times; from the thin walls, we obtain a total of 44 samples from different locations. They are related to local processing parameters, including the average solidification cooling rate of each sample obtained computationally from GAMMA, and the distance from the substrate. From factor analysis, we observed that:

- The amount of the porosity is influenced only by the solidification cooling rate.
- Both the solidification cooling rate and the position are influencing the volume of the voids.
- The shape descriptor Omega3 is not influenced by solidification cooling rate or the position.
- There fewer voids by increasing the SCR and smaller voids by decreasing the solidification cooling rate.
- The effect of the position is not significant.

However, it should be noted that the experimental samples were created without this study in mind. Thus, the chosen process conditions could not be factored into sufficient enough levels for a process-porosity relationship to be established through metamodeling.

G. Development of Bayesian Calibration Package

We developed a modularized Bayesian calibration and bias correction package that enables calibrating computer simulators against experiments. This package allows to estimate the joint posterior distribution (rather than a single point estimate) of the calibration parameters that are not directly observable or measurable. It also estimates a bias function that can explain the potential discrepancies between the computer simulator and the experiments. The unique aspects of our package are that it is robust against numerical errors and is computationally efficient and applicable to multi-response problems.

Task 4: Simulation Software Integration

The software deliverable for integrated Rapid Process Certification has been developed using NX Open Application Programming Interface and tested with Siemens NX 11 on a Windows 7 Operating System.
The purpose of this software prototype is to integrate different software prototypes and guide the user through the steps that need to be performed in order to perform a virtual evaluation of the effects of the additive manufacturing process on the mechanical characteristics of the printed part.

While some of the steps can be performed either for additive manufacturing or for casting, the integrated workflow is only available for additive manufacturing process as the process simulator for casting (MAGMA) was not available for integration.

Two types of process certification workflows have been conceived and implemented during the project. The first type is called “training mode” and refers to the use of a set of accurate and detailed simulation

tools, together with experimental campaigns to acquire data for calibration and model development, to perform predictions at different scales and of different phenomena involved in the manufacturing process. The second type is called "rapid mode" and refers to the use of a set of tools partially overlapping with the ones for the training mode, but where some of the time consuming steps are replaced with faster surrogate models.

In the following paragraphs a brief description of these workflows is provided, together with mapping to the developed. More detailed description of each step is provided in other sections of the document. For the components integrated with the NX environment, see the How-To section.

Figure 48 show the overall workflow for the virtual process certification in training mode. In this mode, the user may perform the following steps either in a chain, where applicable, or as separate steps:

1. Create or load a part representing the *CAD* design in NX. This step is performed using already existing NX functionalities.
2. Create or load an additive manufacturing operation in NX (*toolpath*). This step is performed using already existing NX functionalities.
3. Export the toolpath in the format needed for *experimental tests* and for the process simulation. This step is performed using already existing NX functionalities.
4. Create a hexahedral *mesh* following the specs described in the How-To section. This step is performed using already existing NX functionalities.
5. Select the raw *material properties* and specify the parameters to perform an additive manufacturing *process simulation* and perform the simulation using GAMMA. This step involves a series of sub-steps that are performed using NX Open software prototype components developed during the project as well as GAMMA process simulation software (BIP) improved during the project.
6. Visualize and post-process the results of the process simulation to extract information necessary to perform *material microstructure prediction* and *mechanical property prediction.* This step is partially performed using a NX Open based software prototype component developed during the project.
7. Perform the *material microstructure prediction* and *mechanical property prediction*. This step is performed with BIP software PrecipiCalc, ThermoCalc, DICTRA.
8. Store the results of process simulation into the *voxel storage.* This step is performed using a NX Open software prototype component developed during the project and the Voxel Storage prototype developed during the project.
9. Generate and visualize the optimal sampling of the design space for the generation of a surrogate model. This step is performed using a NX Open software prototype component developed during the project and the *Optimal Latin Hypercube DoE Generation* prototype developed during the project.
10. Generate and visualize the *Gaussian Process Metamodels* for the mechanical properties utilizing the output of the *Optimal Latin Hypercube DoE Generation* in conjunction with the output of the *material microstructure prediction* and *mechanical property prediction* and the *experimental calibration* data. This step is performed using a NX Open software prototype component developed during the project and the *Gaussian Process Metamodeling* prototype developed during the project.
11. Utilize the macroscale mechanical property predicted by either step 7 or step 10 to perform an *as-manufactured product performance prediction*. This step is performed using a NX Open software prototype component developed during the project in conjunction with built-in NX functionalities, specifically NX Nastran Finite Element Analysis capabilities.

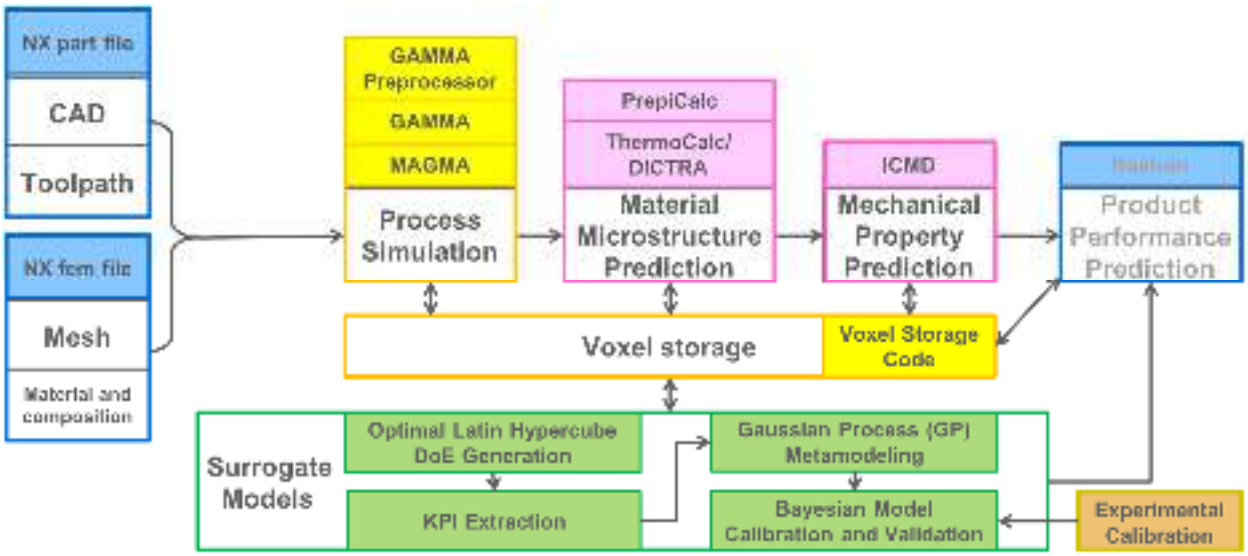

Figure 48 - Virtual certification workflow - Training Mode

Figure 49 show the overall workflow for the virtual process certification in rapid mode. This mode is intended to be used to rapidly evaluate the as-manufactured product performance based on the surrogate models built during the training mode. In this mode, the following steps are supposed to be performed in a chain workflow:

1. Create or load a part representing the *CAD* design in NX. This step is performed using already existing NX functionalities.
2. Create or load an additive manufacturing operation in NX (*toolpath*). This step is performed using already existing NX functionalities.
3. Export the toolpath in the format needed for the process simulation. This step is performed using already existing NX functionalities.
4. Create a hexahedral *mesh* following the specs described in the How-To section. This step is performed using already existing NX functionalities.
5. Select the raw *material properties* and specify the parameters to perform an additive manufacturing *process simulation* and perform the simulation using GAMMA. This step involves a series of sub-steps that are performed using NX Open software prototype components developed during the project as well as GAMMA process simulation software (BIP) improved during the project.
12. Visualize and post-process the results of the process simulation to extract information necessary to perform *material microstructure prediction* and *mechanical property prediction through the surrogate models* generated during the training mode. This step is partially performed using a NX Open based software prototype component developed during the project and the *Gaussian Process Metamodeling* prototype developed during the project.
6. Store the results of process simulation into the *voxel storage.* This step is performed using a NX Open software prototype component developed during the project and the Voxel Storage prototype developed during the project.
7. Utilize the macroscale mechanical property predicted by step 6 to perform an *as-manufactured product performance prediction*. This step is performed using a NX Open software prototype component developed during the project in conjunction with built-in NX functionalities, specifically NX Nastran Finite Element Analysis capabilities.

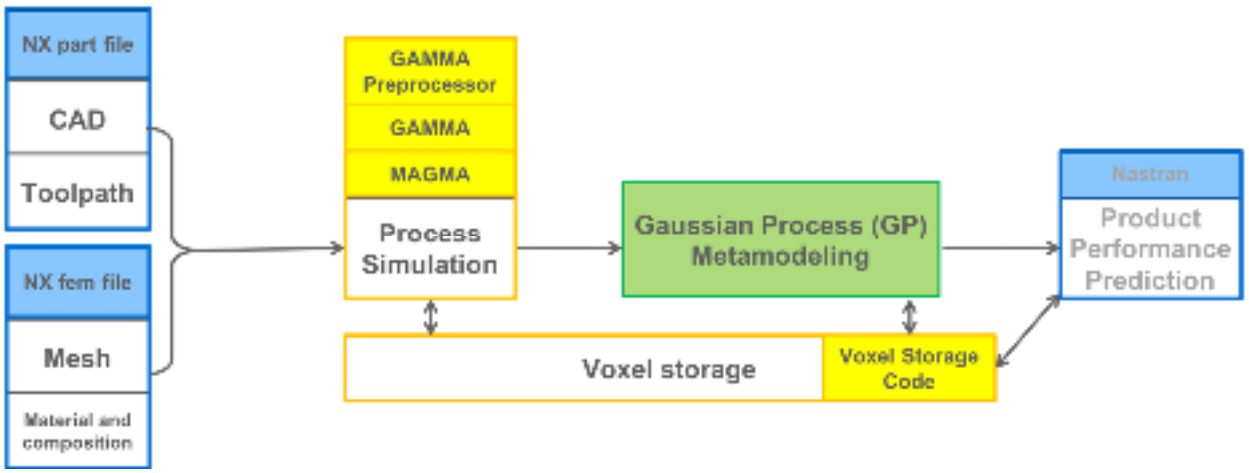

Figure 49 - Virtual certification workflow - Rapid Mode

How to Use the NX-based Prototype

For installation instruction, please see the Appendix of this document.
In this section, the functionalities implemented in the NX-based add-on for process certification will be introduces.
To run the NX add-on, double click on the file NX.bat in the installation directory.
The integrated Process Certification NX add-on includes a set of functionalities that are shown in in the add-on ribbon shown in Figure 50.

Figure 50 - Process Certification add-on ribbon in NX.

The first step to be perform to start a process certification project is to click on button "Configure RPC Project". This button opens a dialog box that can be used in 2 ways:

1. Open an existing process certification project and browse the files already created in a past instance of the program (*Figure 51*).
2. Create a new process certification project (*Figure 52*).

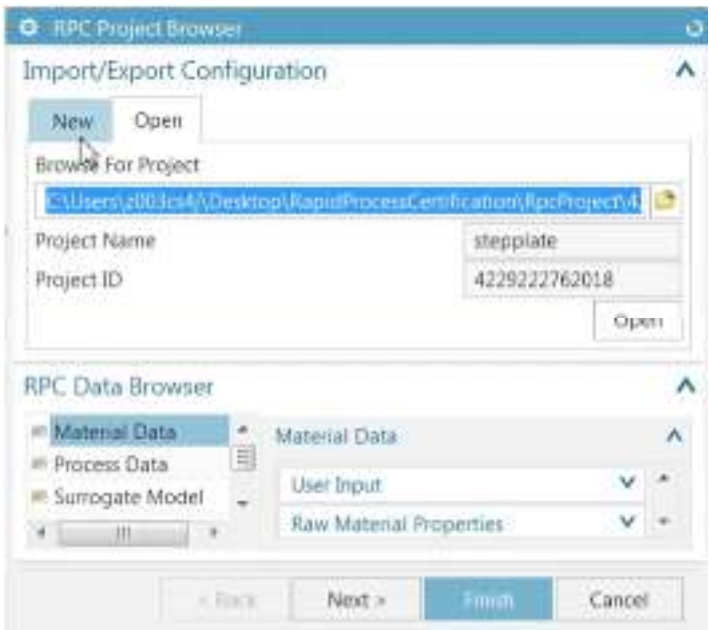

Figure 51 - Open existing process certification project.

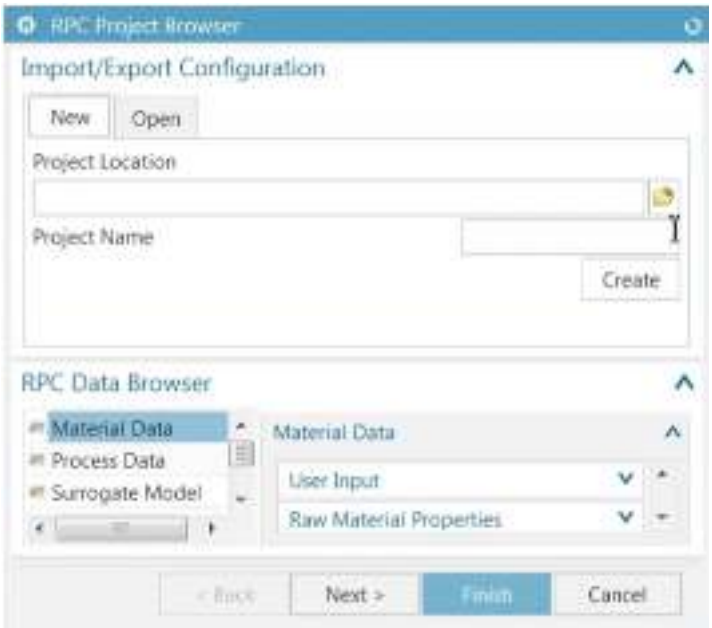

Figure 52 - Create new process certification project.

When a process certification project is created, a folder is created in the specified location of the filesystem, containing a predefined sub-folder structure to contain all the input/output data needed for the operation of the program. The name of the parent folder for the project will be composed of a unique ID, automatically generated, concatenated with "_" and the user specified name. Inside the project folder, the following sub-folders will be created:

- "CAD" folder is where the CAD file in NX compatible format (e.g. .prt) is supposed to be stored

- “CAE” folder is where the simulation-related files are automatically stored, such as mesh in GAMMA compatible format, results of GAMMA simulation, results of NX NASTRAN simulation.
- “CAM” folder is where the manufacturing operation toolpath will be exported, in the various formats needed for the process certification.
- “MATERIAL” folder is where the data related to material properties (either needed for material characterization, or computed by the material characterization tools) will be stored.
- “MM” folder contains the output of the Optimal Latin Hypercube Sampling (OLHS) and of the Gaussian Process Modeling (GPM) tools and is supposed to contain the training data for GPM.

In addition, a file with the user specified project name and extension “.rpc” is generated to store the project configuration information.

The next step is to load or create a 3D CAD model, using native NX functionalities. For the use case in this demonstration, the part is composed of two vertical structures, with step features, as shown in *Figure 53*. The base plate is also part of the part file, per requirements of GAMMA simulation software. For additional guidance in the preparation and use of GAMMA, we refer to the document GAMMA_INPUT_MANUAL.pdf.

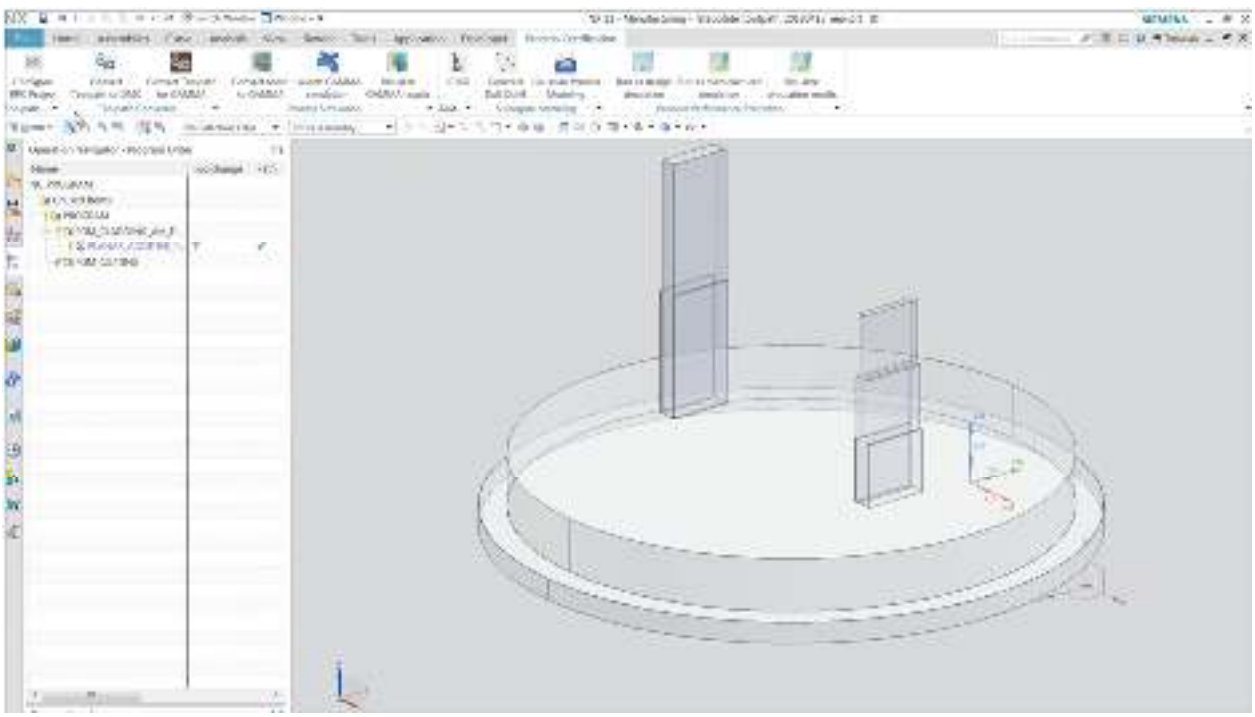

Figure 53 - Step plate test part with base plate.

The model can be optionally manipulated using NX functionalities such as scaling and translating.

Next, an additive manufacturing operation can be created using the functionality provided by the NX CAM Hybrid Manufacturing Beta Release. In this way, the additive manufacturing process settings can be specified using the dialog box and the generated toolpath can be visualized using the animation functionality in NX CAM, as shown in *Figure 54*. For more information on how to operate in the NC CAM environment, please refer to NX documentation.

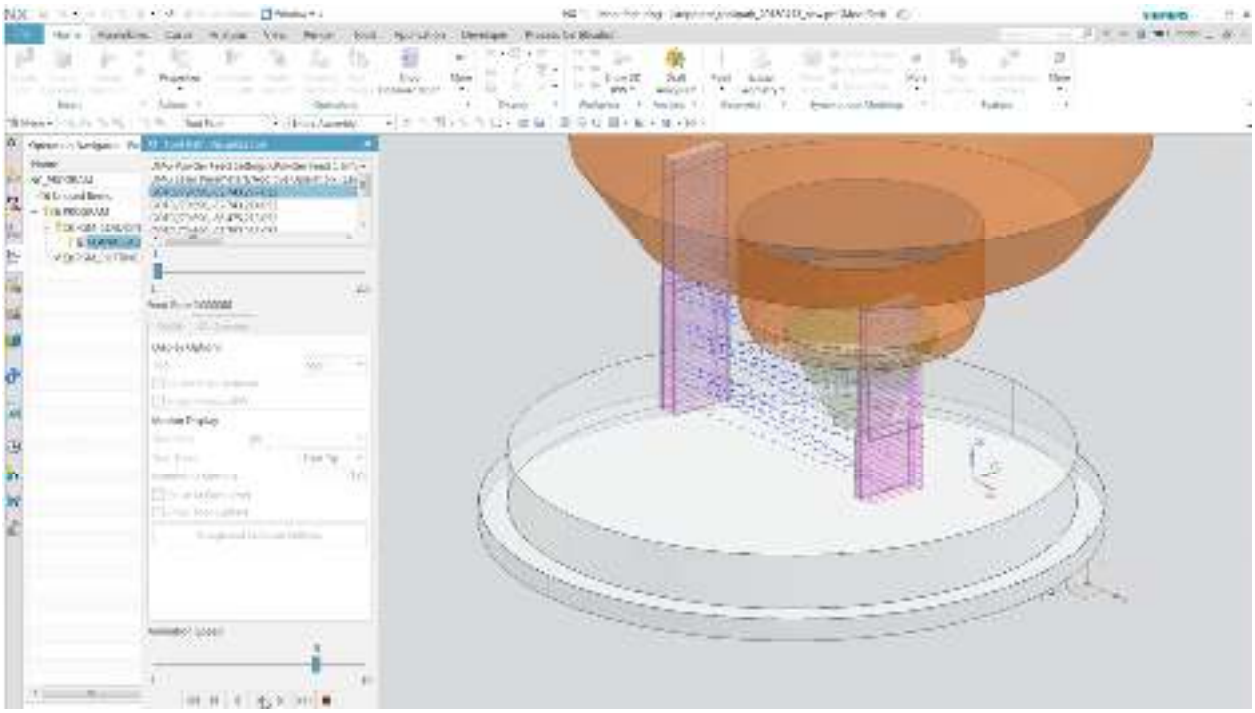

Figure 54 - Visualization of additive manufacturing toolpath in NX.

Once the toolpath is generated, the NX Open based add-on allows to convert it to the format needed by the additive manufacturing machine used for testing during the project (DMC format), using the menu option “Convert Toolpath to DMC” (*Figure 55*), that allows to input machine specific conversion factors.

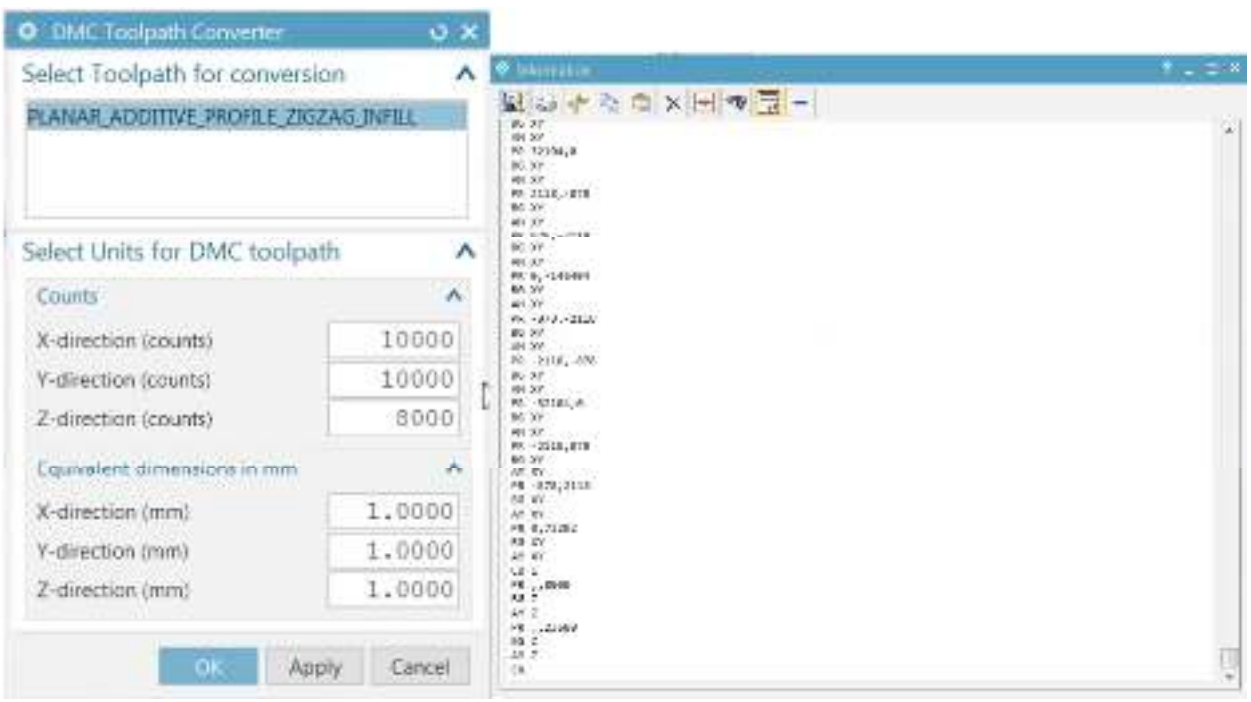

Figure 55 - Dialog box for toolpath conversion to DMC an example output format.

In addition, the toolpath can be exported in the format needed by GAMMA to perform the process simulation, as shown in Figure 56.

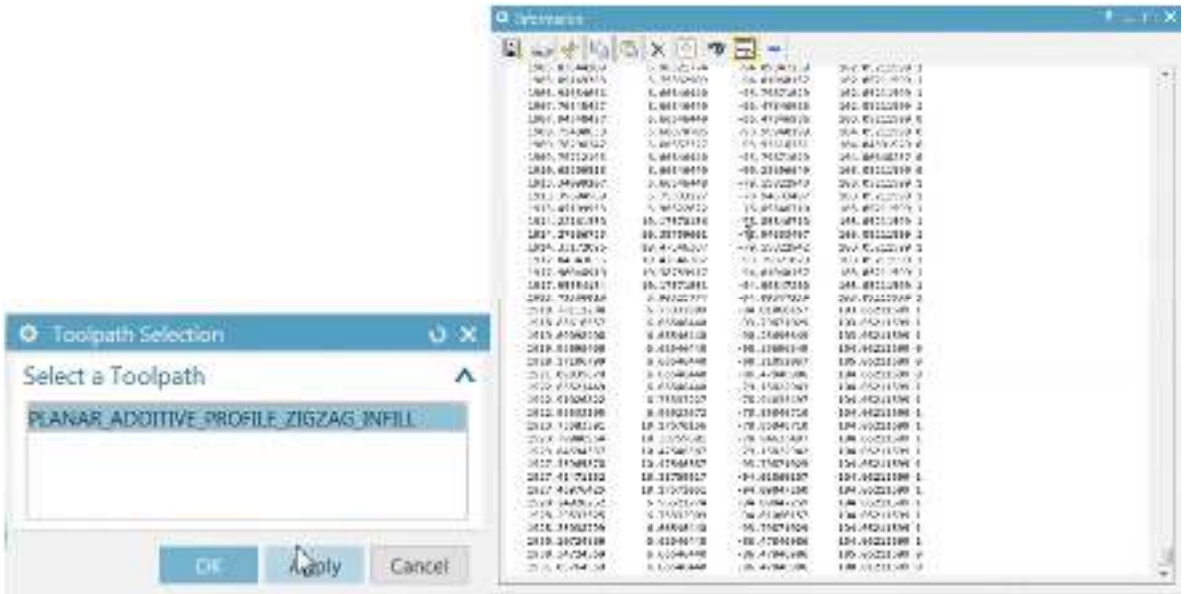

Figure 56 - Dialog box for toolpath conversion to GAMMA compatible format.

The following step of the workflow consists in creating the finite element mesh of the CAD part, or loading an existing one.

The mesh has to satisfy the following conditions in order to be compatible with GAMMA. For further information, please refer to the document GAMMA_INPUT_MANUAL.pdf.

- The mesh must consist of only hexahedral elements.
- An integer number of elements has to be created for each hatch spacing.
- An integer number of elements has to be created for each layer thickness in the build direction.
- Both the part to print and the build plate need to be meshed.

To create a new mesh in NX, a new Finite Element model needs first to be created from the CAD part (File->New-Simulation->NX Nastran FEM). Next, the NX meshing functionalities can to be used to create first a quadrilateral mesh on horizontal surfaces that can be extruded to form hexahedral meshes. For further information on mesh generation capabilities, please refer to NX documentation.

An example of mesh generated using NX is shown in *Figure 57*.

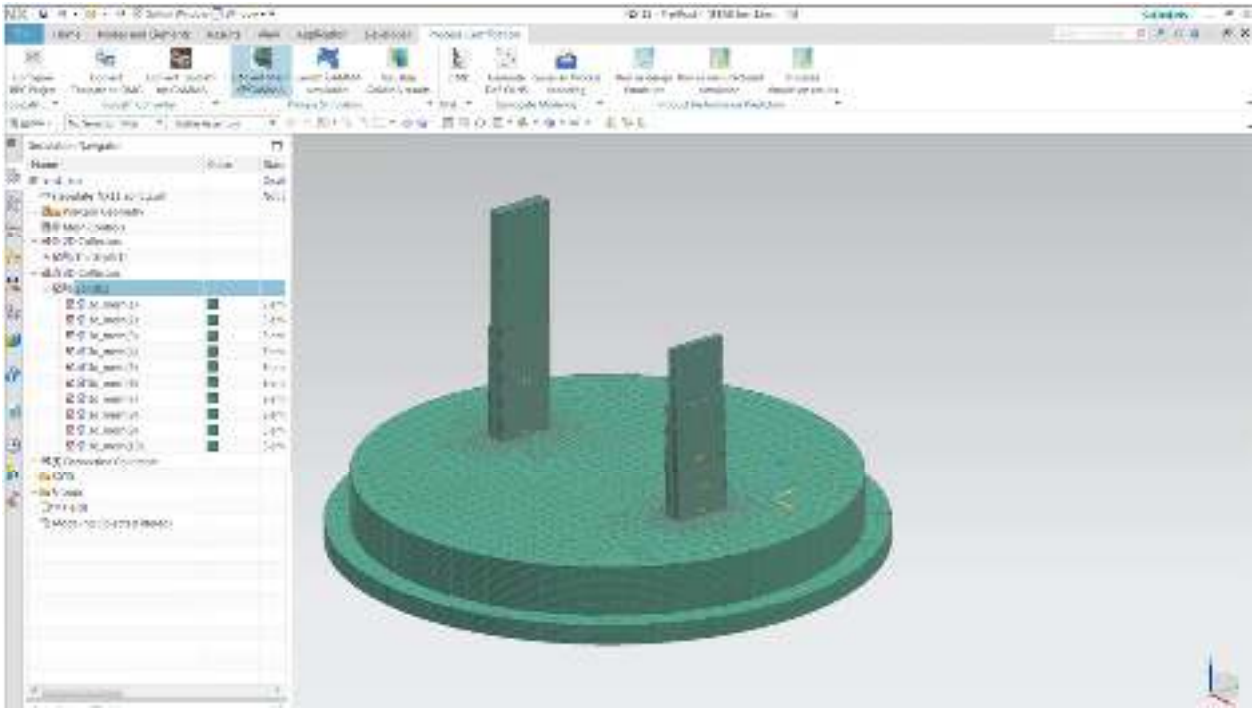

Figure 57 - GAMMA compatible mesh generated using NX.

Next, the button “Convert Mesh to GAMMA” can be triggered. The dialog triggered by this action (*Figure 58*) collects a series of input information that is needed from the user in order to prepare the input file to execute a thermal simulation of the additive manufacturing process using GAMMA.

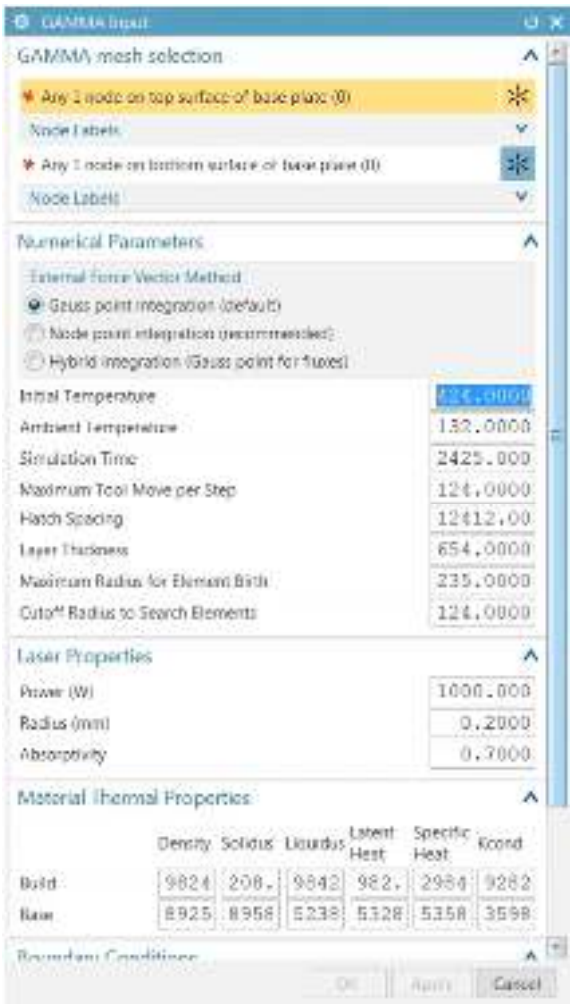

Figure 58 - Dialog box to collect user input needed to run GAMMA.

The user input includes the selection of mesh nodes needed to identify the mesh of the base plate and distinguish it from the mesh of the build part. In addition, properties needed to correctly set up the boundary conditions and other simulation parameters are required at this stage. Once the "OK" button is selected, the mesh and input file for GAMMA are generated and exported in the "CAE" folder of the project directory.

Next, the button "Launch GAMMA simulation" can be triggered. This opens a dialog box (*Figure 59*) from which the user can trigger a GAMMA simulation ("Start GAMMA") and check the status of a GAMMA simulation ("Check GAMMA Status"). Since GAMMA is developed to run on an unix operating system, while the integrated NX-based process certification is set up to run on a Windows operative system, to run a GAMMA simulation the connection with a virtual machine running Ubuntu operative system needs to be set up and utilized.

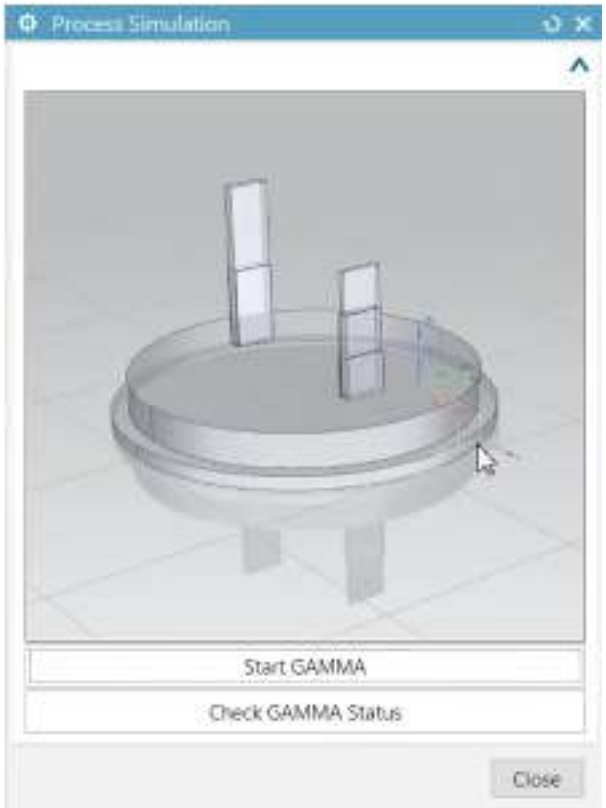

Figure 59 - Dialog box to perform a GAMMA simulation.

The “Start GAMMA” button performs the following actions in the background:

1. Packages the set of input files for a GAMMA simulation
2. Transfers the input package to the virtual machine
3. Connects to the virtual machine
4. Triggers the execution of a GAMMA simulation

The “Check GAMMA Status” button performs the following actions in the background:

1. Connects to the virtual machine
2. Checks if the simulation process is running.
3. If the process is complete, packages the output files and transfers them to the project folder (subfolder “CAE”) on the host Windows machine.
4. Unpackages the output package.

After the simulation is over, the native results in VTK format can be converted into NX-compatible UNV format and visualized and explored in NX, by clicking on the button “Visualize GAMMA results”.

Figure 60 - Options to import GAMMA results.

Two options are provided:

- *Single-step* can be used to convert and load the results of a single time point. In this case the output file in VTK format has to be selected and the option "Merge mesh partitions" can be selected in case the GAMMA simulation was run on multiple processors. If this is the case, the software analyzes the meshes of each partition and then merges them in a single one to generate the results to be shown in NX (*Figure 60*, left).
- *Multi-step* can be used to convert and load the results of all the available time point. In this case in multiple mesh partitions exist, they are automatically merged in a single one to generate the results to be shown in NX (*Figure 60*, right).

Once imported, the results can be explored using all the native functionalities provided by NX, including the possibility to animate transient results loaded using the multi-step option. An example of visualization is shown in *Figure 61*.

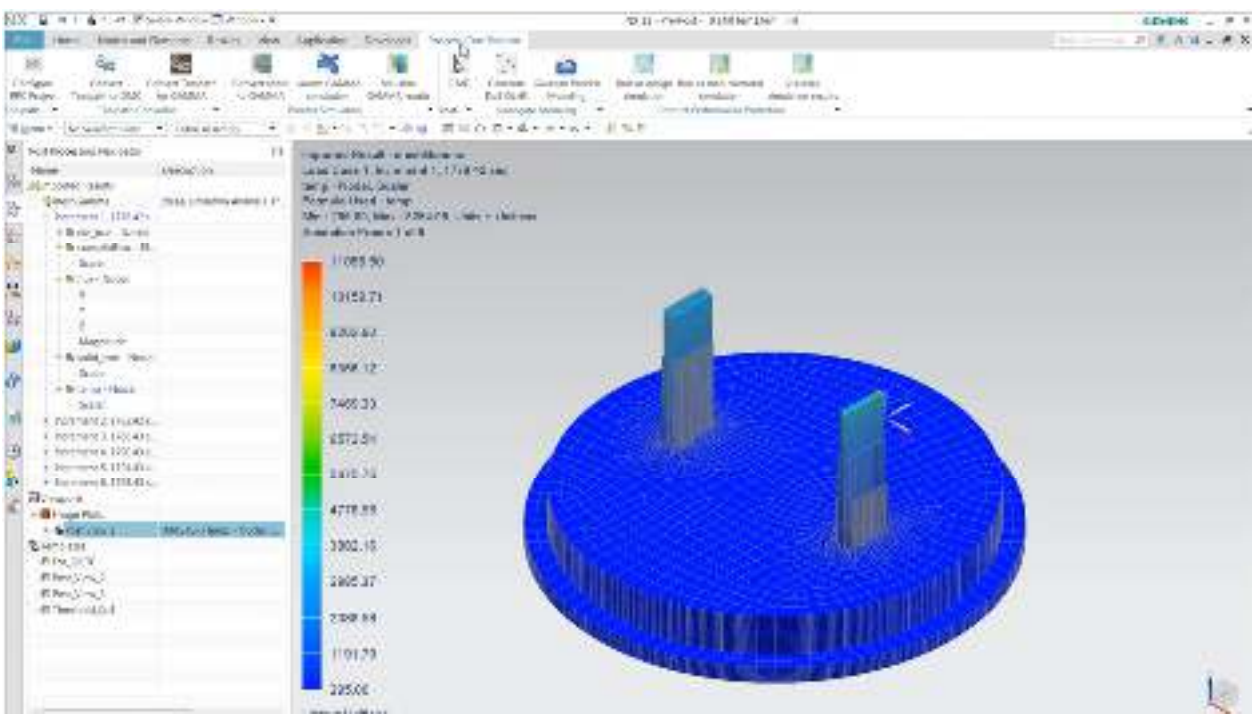

Figure 61 - Visualization and exploration of GAMMA results.

The next step of the workflow consists in the preparation of thermal history data in view of Integrated Computational Material Design (ICMD). While the material characterization software tools could not be integrated for copyright reasons, the utility triggered by clicking on “ICMD” button can be used to prepare the data that need to be manually fed into the separate material characterization software, in order to prepare the training data for the Gaussian Process Modeling step. As shown in *Figure 62*, multiple options are provided. In all cases, the first step consists in clicking on “Load GAMMA mesh”. Then the user can either select one specific location (mesh node), then select “Plot and Export thermal history last picked node”, to visualize the history, as in *Figure 63*, or/and select “Export thermal history of the selected nodes”, to save on file the information. Alternatively, the thermal history of all location can be exported all at once, by selecting the last option in the dialog box. All the exported files will be saved in the “MATERIAL” subfolder of the project directory.

Figure 62 - Dialog box to export thermal data for ICMD computation.

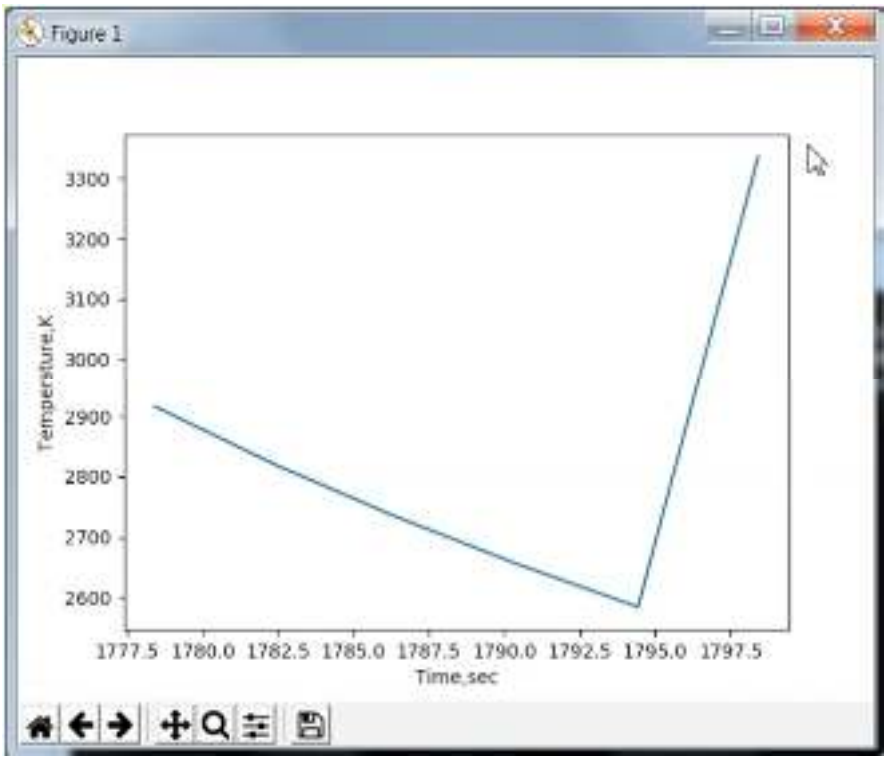

Figure 63 - Example of thermal history plot for a single location.

The next step of the workflow consists the generation of the Gaussian process model based on the available (experimental or simulated) data. To do so, the user can select "Generate DoE OLHS" to first generate the sampling point using the Optimal Latin Hypercube Sampling (OLHS) algorithm developed during the project. As shown in *Figure 64*, the user can specify the number of variables to be predicted and the desired number of samples. Then the optimality criterion can be selected between "Entropy", "Maximin" and "Centered L2 Discrepancy" (further details on the different options and on the algorithm are provided in Section XX). Then the button "Generate DoE OLHS" can be selected to generate the samples. The user can inspect the generated samples in the design space via 2D or 3D plots. In both cases, the variable IDs to be plotted on each axis should be provided as input, before clicking on "Visualize the OLHS on a Plot". Two examples of visualization are shown in *Figure 66*, while *Figure 65* shows the native output of the OLHS executable. The generated output of OLHS (coordinates of the generated samples) is saved in folder "MM" of the project directory.

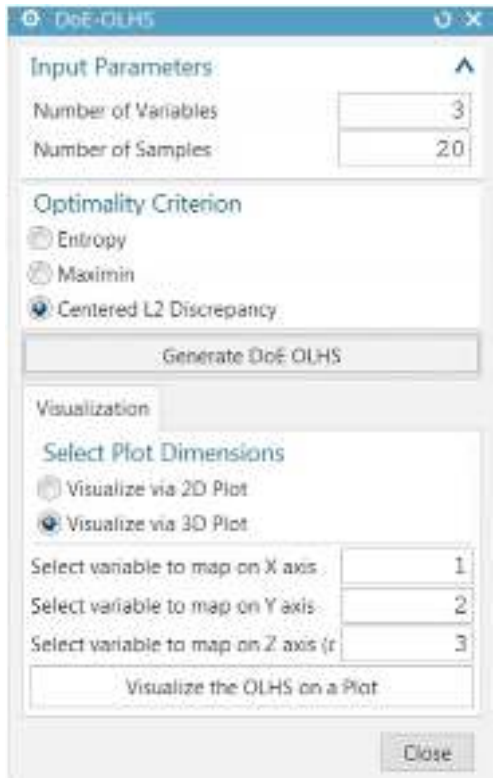

Figure 64 - Dialog box to generate and visualize the OLHS.

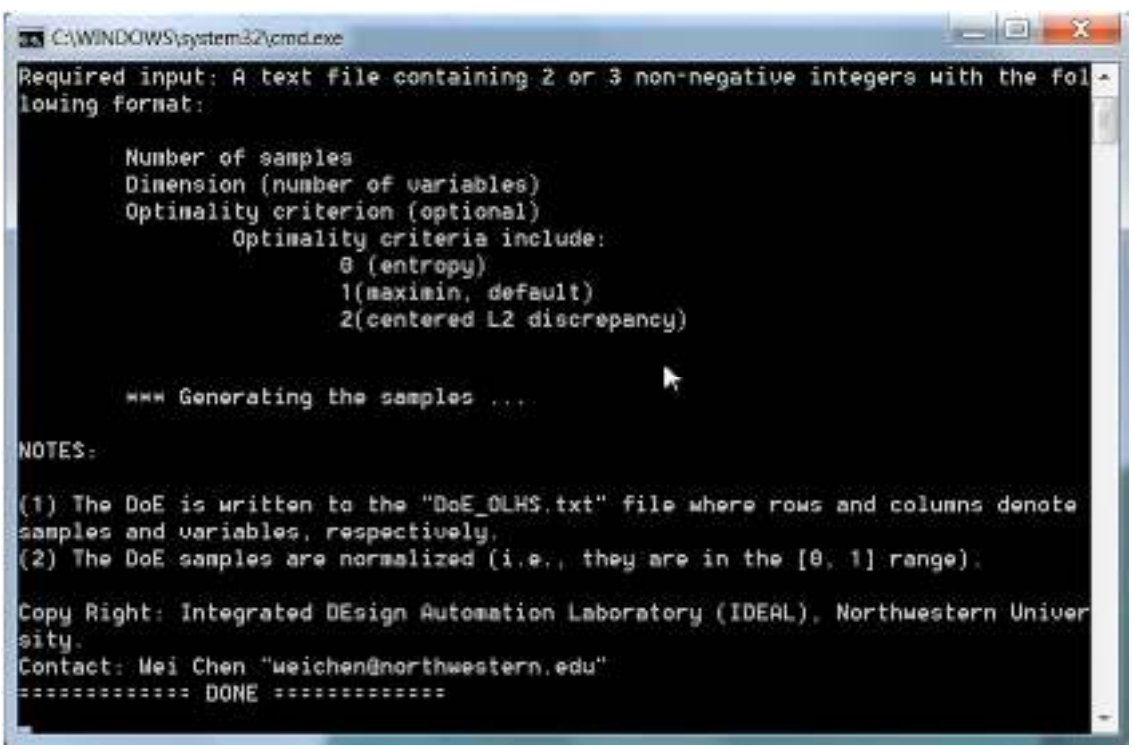

Figure 65 - Native output of the OLHS executable.

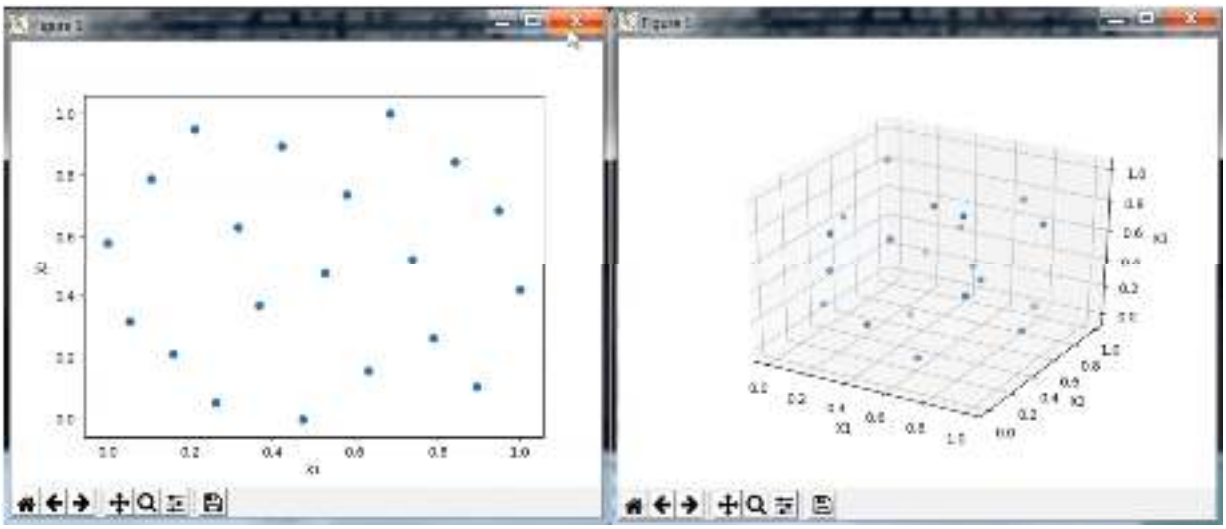

Figure 66 - Example of 2D (left) and 3D (right) visualization of the OLHS results.

Once the samples are generated and training data is available on sample points, the next step "Gaussian Process Modeling" can be triggered. In the dialog box (*Figure 67*), the user has to input the name and index of the input/output variables and the title of the plot, input the number of points to plot, select the file containing the input and output training data. Once the input is provided, clicking on "Fit GP Model" performs the meta-model generation. *Figure 68* shows the native output of the GPM executable, while *Figure 69* shows the visualization of the fitted model.

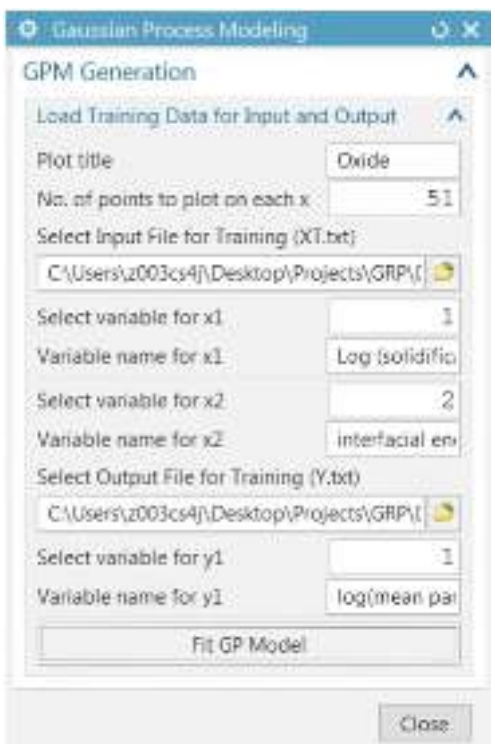

Figure 67 - Dialog box to gather input for the Gaussian Process Model fitting.

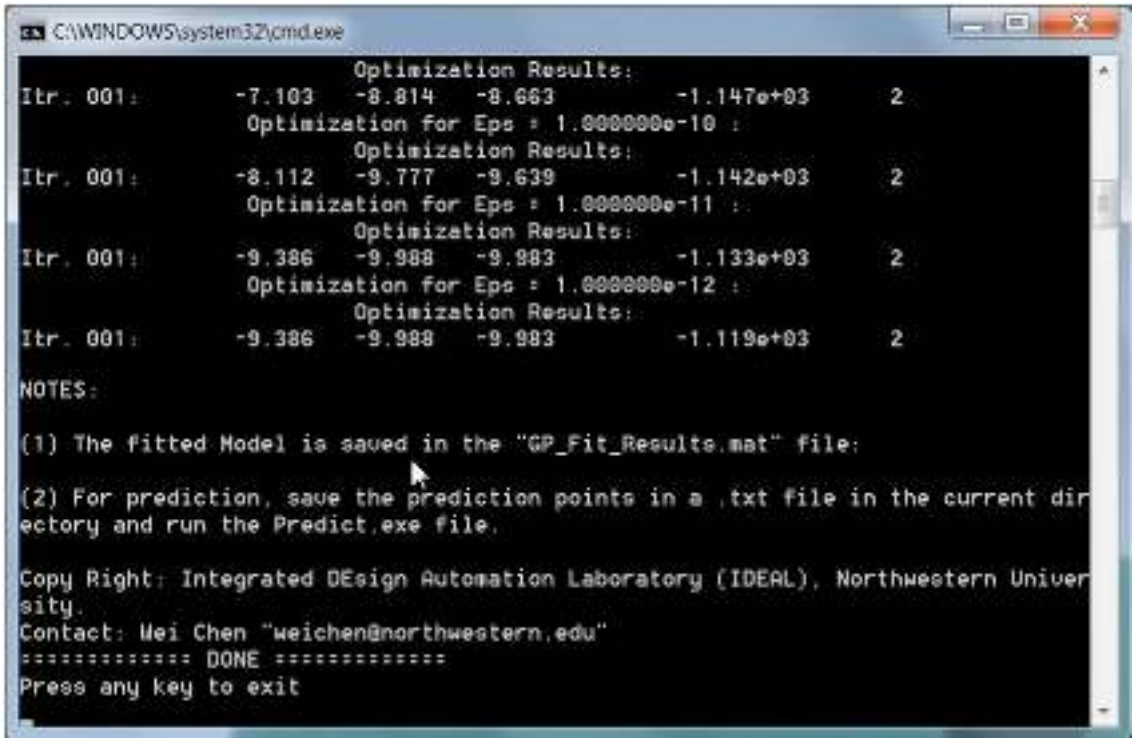

Figure 68 - Native output of the Gaussian Process Modeling executable.

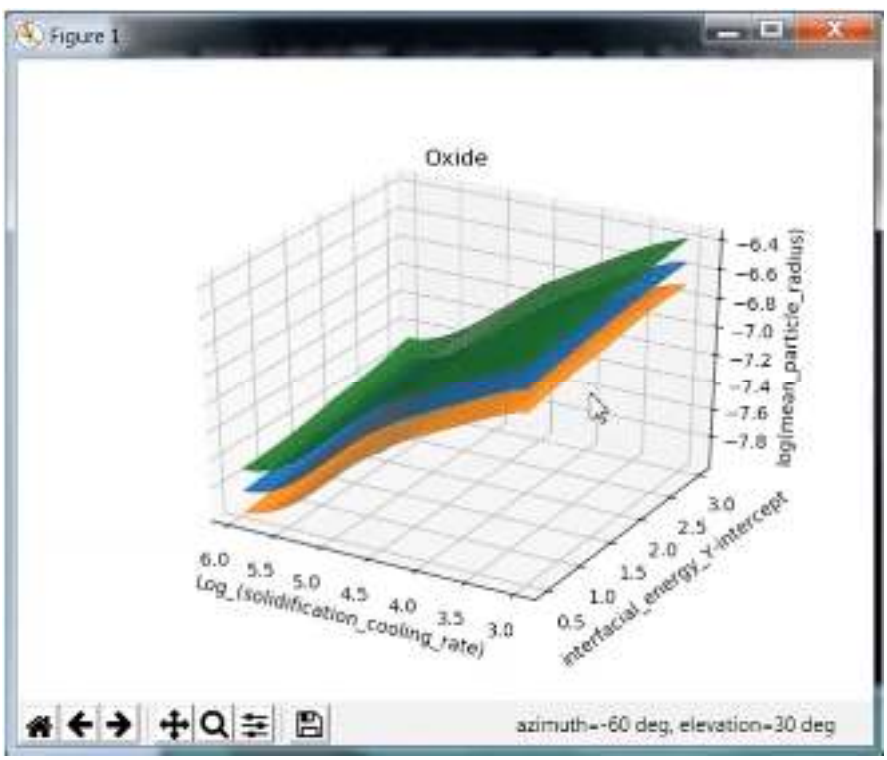

Figure 69 - Example of visualization of a surrogate model that predicts the logarithm of mean particle radius as a function of the logarithm of the solidification/cooling rate and of the interfacial energy.

The last steps of the process certification workflow consists in performing a structural simulation to virtually evaluate the mechanical performance of the printed part. The first step is to setup a NX Nastran simulation, by adding load and constraints to the finite element model previously created and to assign as-designed material properties, using the NX functionalities. Then, three utilities are provided to perform the project specific analyses.

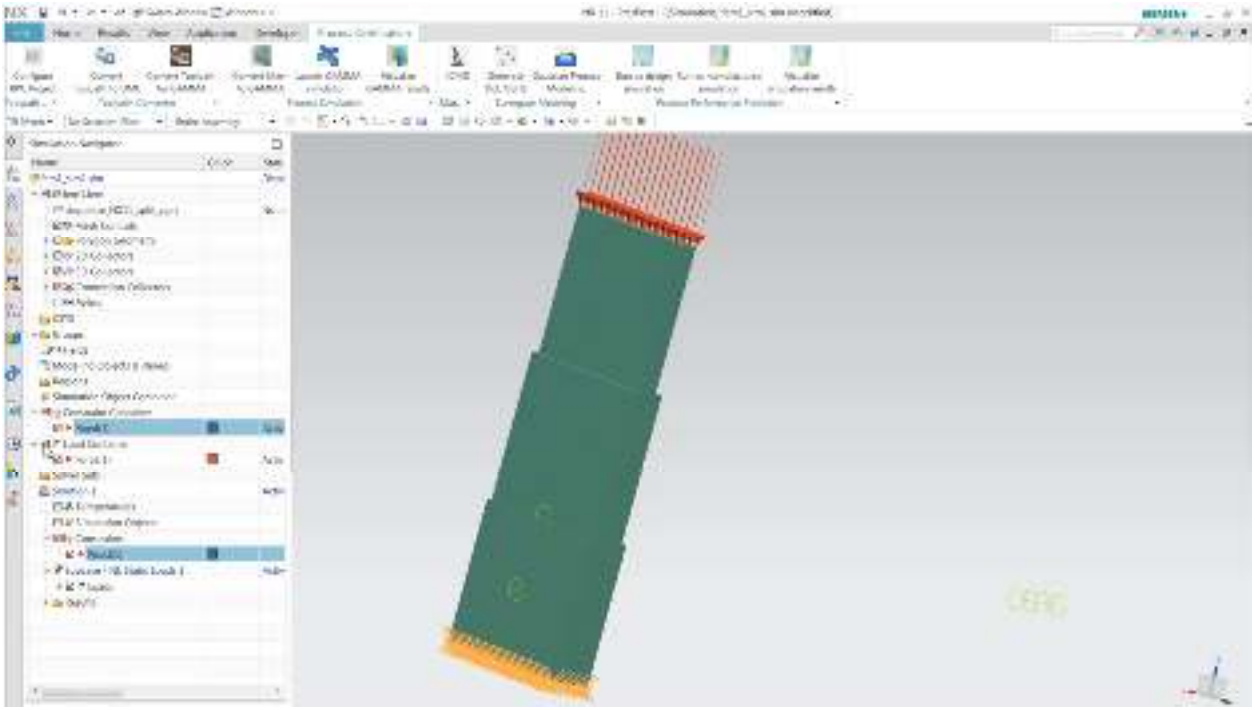

Figure 70 - NX Nastran simulation model with load and constraints.

The user can click on the button "Run as designed simulation" (*Figure 71*) to perform a non-linear static analysis of the selected part using the material properties of the raw material, using NX Nastran. The computed displacement and stress can then be visualized and explored by clicking on the button "Visualize simulation results" (*Figure 72*).

Figure 71 - Dialog box to trigger the as-designed simulation.

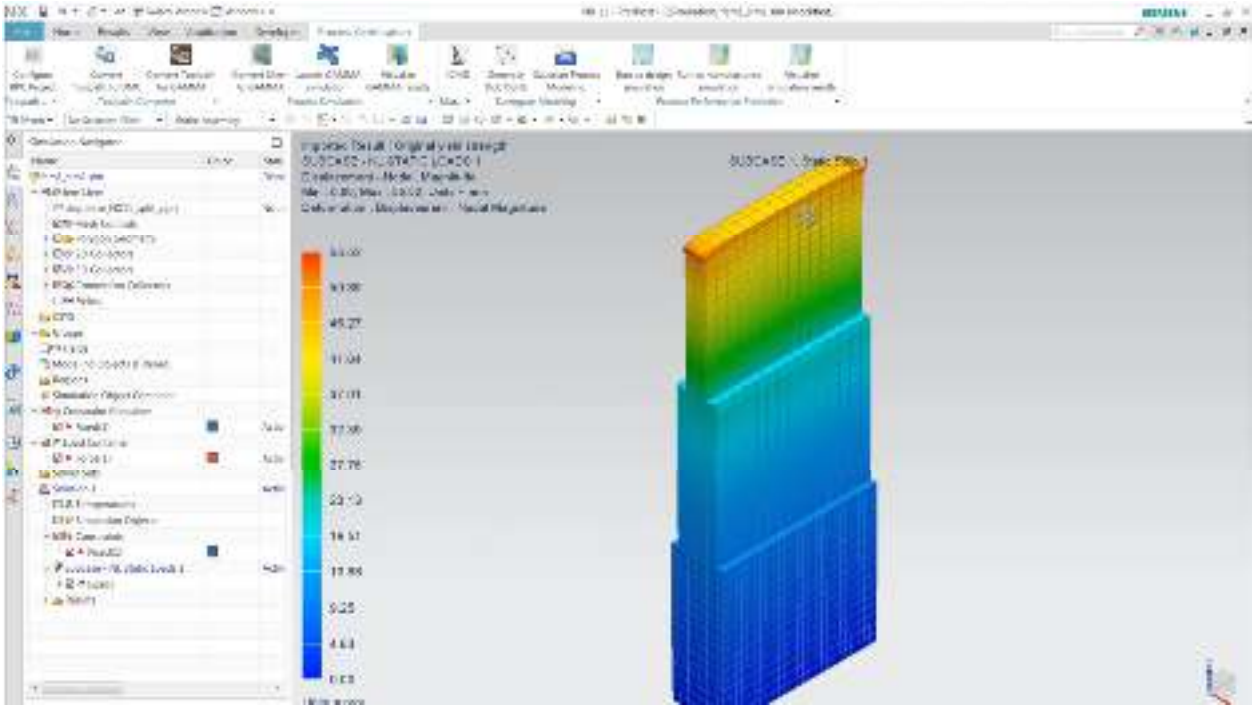

Figure 72 - Visualization of the as-designed simulation results.

Then, the user can click on “Run as manufactured simulation” (*Figure 73*). In this case, the as-manufactured mechanical properties computed using the GPM (specifically, the first value of the predicted output, which represents the yield strength) is retrieved for all the elements in the mesh and utilized in the setup of the NX Nastran non-linear static analysis. When performing this step, the data is automatically sent to the virtual machine and populates the voxel database. Before performing this step, the user has to specify variables X2 through X9 in the script extractGAMMAresults.py to input the raw material composition (see information provided in the Gaussian Process Modeling section). Instead, the first variable X1 will be automatically read from the output of the GAMMA simulation.

The results of the as-manufactured analysis can be visualized in comparison with the as-designed analysis results by clicking on “Visualize simulation results” (*Figure 74*). The results of these analyses are saved in the “CAE” subfolder of the project directory.

In order to retrieve the mesh collector ID of the portion of the model that the user wants to simulate, an inspection of the properties of the mesh needs to be carried out, before triggering the as-manufactured simulation. Specifically, after activating the meshing environment, the user can right click on mesh collector in the Simulation Navigator window (on the left), select “Edit”, (*Figure 75*, left), clock on the edit button next to the Solid Property (*Figure 75*, middle) and then inspect the property “Label” in the windows that appear (*Figure 75*, right). Such label is the one to input in the dialog in *Figure 73*.

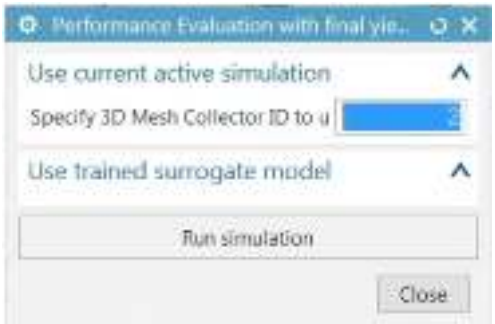

Figure 73 - Dialog box to perform the as-manufactured simulation.

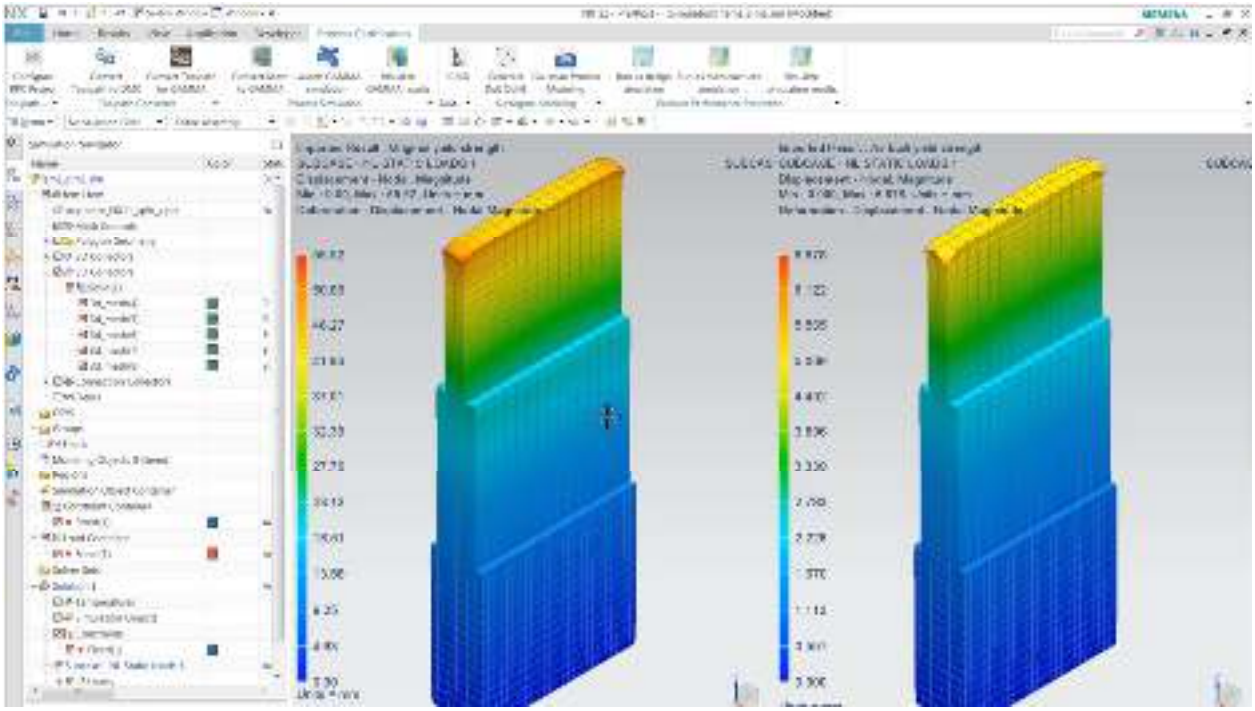

Figure 74 - Example of comparison between as-designed and as-manufactured simulation results.

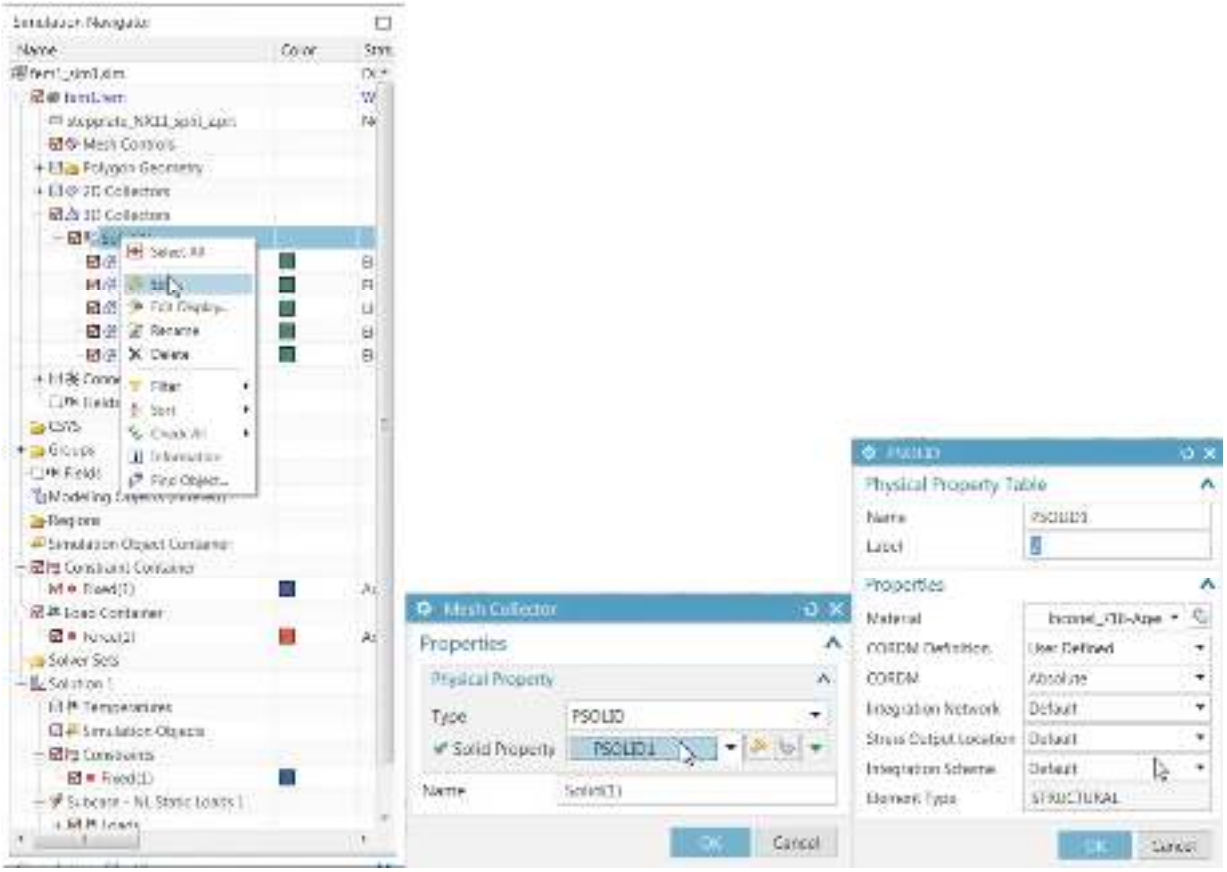

Figure 75 - Steps to retrieve the Mesh Collector ID.

Task 5: Verification and Validation

There were two main objectives in this task, the first was to provide experimental data to Task 1 and 2 so that they could validate their models. This experimental data came in the form of the thermal history via thermocouples and IR data as well as information from the power measurement calorimetric system. It should be noted that all the data collected for this task is part of the deliverables so that other DMDII members that would like to validate their model can use this information. The other objective was to build the validation samples using metal additive manufacturing via direct energy deposition with the LENS process. These samples were to verify that the process could yield a repeatable microstructure that had acceptable microhardness. It also served as a way to validate and verify the models being developed in Task 2.

Initially, NIU, NU, Siemens, PDA, and QuesTek discussed the development of a "standard test article" design and opted for the sample as created by Penn State University work entitled "Anisotropic tensile behavior of Ti–6Al–4V components fabricated with DED AM" [1] it is a simple format, which was given the name "cruciform" that can be utilized both in AM as well as casting for comparative purposes. Figure 76 shows a sketch of the "cruciform" sample along with corresponding dimensions. The casting analysis was later handled by PDA and is discussed later in the report.

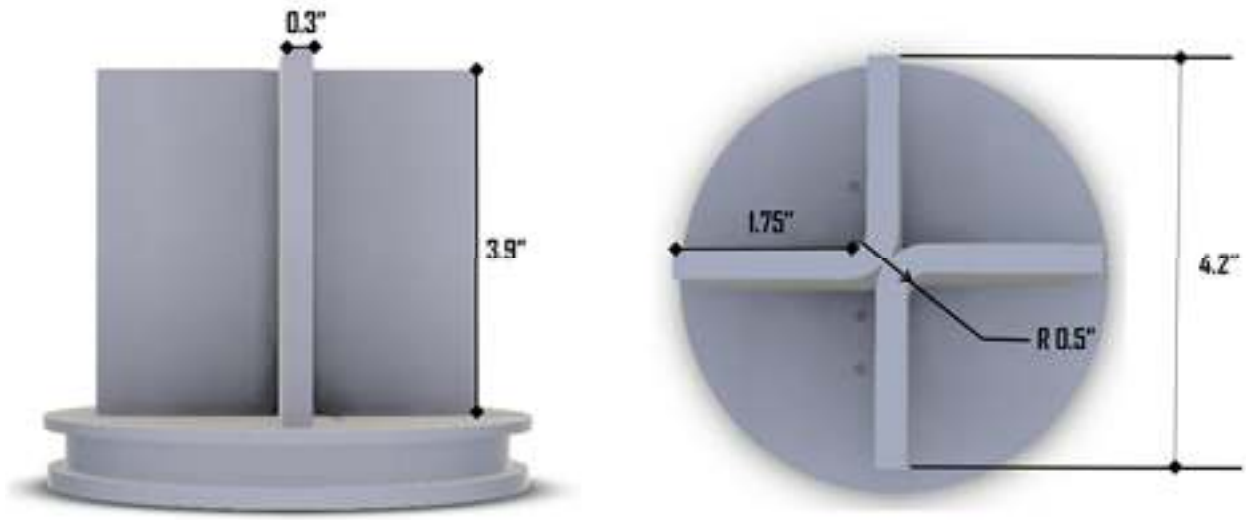

Figure 76. Sketch of "cruciform" build that will be used for Task 5 for validation and verification all dimensions are in inches

In order to build the "cruciform" it is necessary to have process parameters that are well established and can provide repeatable results. This aspect is critical because with that repeatability it makes the work in Task 2 (modeling & simulation) easier to validate and work with. Fortunately, NIU had spent the past several years developing a better understanding of the process parameters for laser metal additive manufacturing of 316L and results are shown in [2]. This knowledge base served as the starting point for the work to be done in Task 5. While the ultimate goal was to use a new material PH 48S, since the delivery was going to take time and 316L was very similar in chemistry we began with this data set.

A. Initial Data Development

At this stage it was critical to work closely with Task 2 and find ways to ensure our data would be easy to use and understand. Therefore, using the optimized parameters from [2] NIU built its first "cruciform" to provide the modeling team in Task 2 some initial data as collected from the various in-situ monitoring systems with the minimum amount of heat input that can easily be validated numerically. Shown in Figure 77 the sample was not built to complete height after 10hrs we only managed to build 2" (half the total height ~3.9") and there were some problems with the collection of our experimental data. Below Table 9 shows the parameters that were utilized for this build.

Table 9: Processing parameters utilized for first "cruciform" build based on data from [2]

	Measured Laser Power (W)	Travel Speed (in/min)	Powder flow (g/min)	P_f/T_s Ratio (g/in)
316L -55	470	30	8.55	0.29

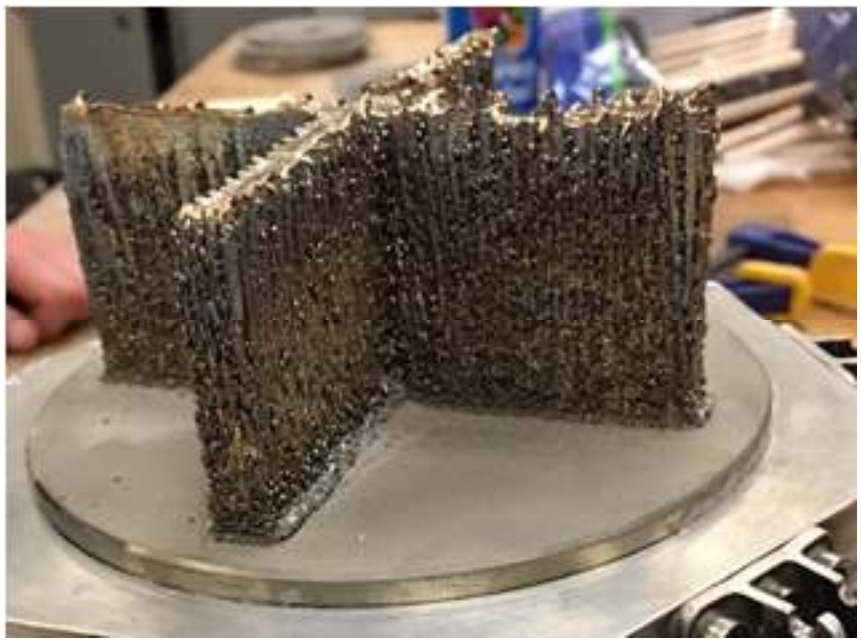

Figure 77 – View of cruciform build height was ~2" and it took 10 hrs. to build

There were some key lessons learned in this initial trial. The first and most critical was that while our chosen process parameters yielded good results, the bead size that results from these settings was too small for Task 2 to model and would take a lot of computation time and obviously took a long time experimentally to build (10 hours to build 2 inches of height). As such the next section will highlight some of the experimental work done to achieve the appropriate bead size to reduce both experimental and computational build time. The second lesson learned was how to correctly translate the code (i.e. DMC) utilized by the additive manufacturing machine that details the build path for simulation purposes. Here both NIU and NU worked on ensuring the code used in the DMC file to operate the AM system was able to be translated so that NU could simulate the build path. The final lesson learned was that on the curved portions of the samples some further analysis would be required as there was large pores found and therefore they need to be eliminated. Figure 78 shows the schematic of the cruciform as built and the sections that were cut for microstructural analysis. Measurements were made in the top and bottom and there was no major differences were seen. The microstructure of the builds from this initial cruciform are taken both at the straight area (section B-B) and the curved area (Section C-C) and is compared to the previous microstructure obtained in the work done in [2]. It is clear that the results from the straight piece and half Charpy sample are very similar. The bottom curve shows some of the large pores mentioned. It seems that some further energy analysis will be required to compensate for the issues occurring.

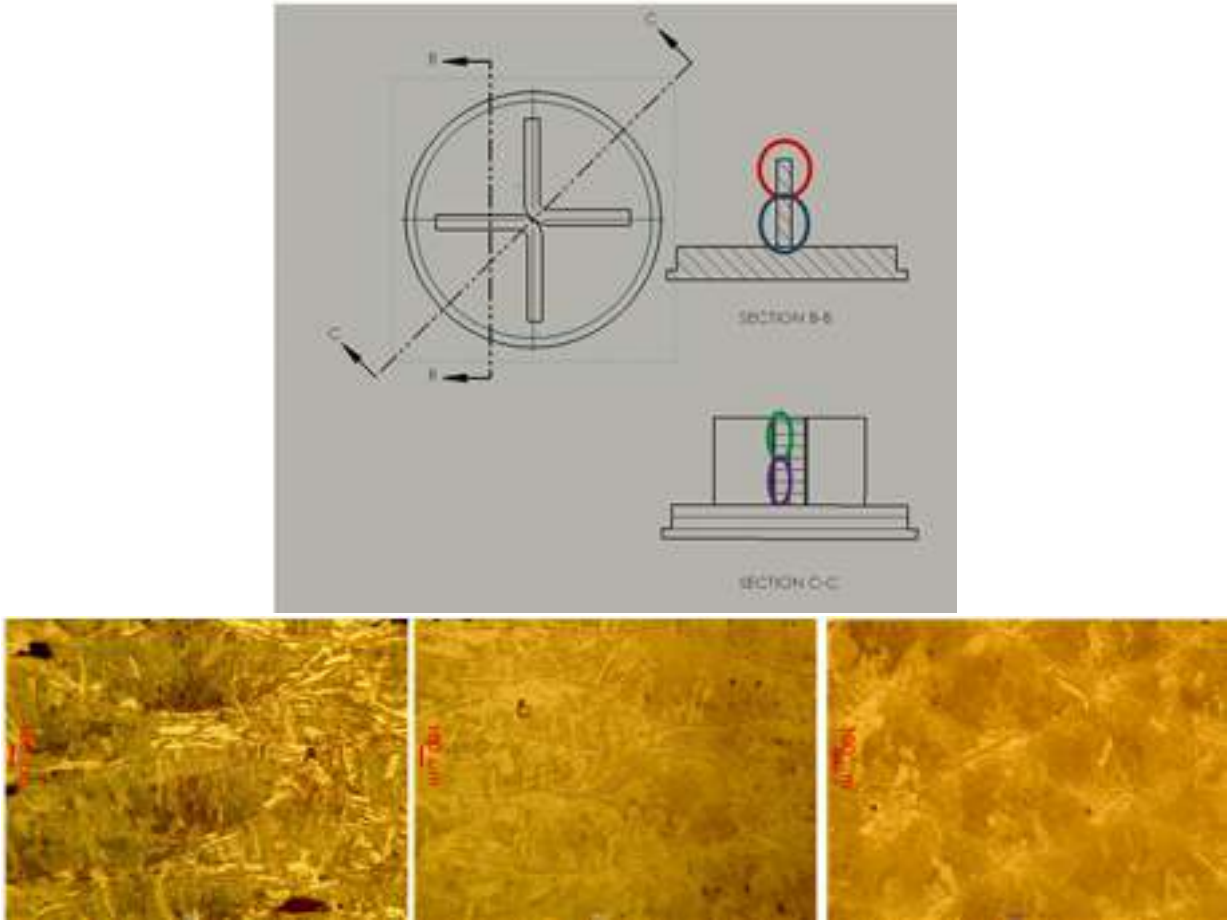

Figure 78- (Top) schematic of "cruciform" and areas section for analysis. (Bottom) representative microstructure from left to right (left) section C-C top curve portion of cruciform, (middle) section B-B straight bottom portion of cruciform, (right) Half-Charpy from previous work done in [2].

B. Process parameter improvement for numerical and experimental optimization

As stated in the previous section the process parameters utilized from our research in [2] yielded good microstructure and mechanical properties but it would take close to 20 hours to build one "cruciform" sample which is ~3.9 inches in height. This is not efficient from the standpoint of manufacturing. As such through our discussions we wanted to at least double our bead size and get to ~ 1mm. In order to do this we went back and looked at our data and plotted our ideal powder flow to travel speed ratio and the power that was measured (see Figure 79). From this we saw there was a linear trend and realized that if we wanted to have larger beads it would require more powder and as such higher power ~ 800 Watts.

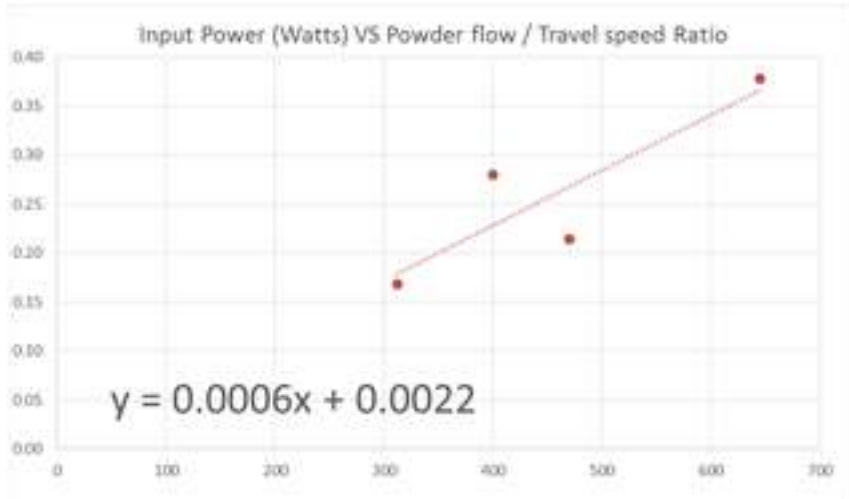

Figure 79. Plot of the input power (W) vs the powder flow/Travel speed ratio as detailed in [2]

Table 10 shows the parameters used both in the initial 316L and then the PH48S analysis to develop larger beads. It was important to re-write the DMC file so that we could accomplish the build with a multiple of hatch spacing to match the layer width. This ensured there were no finishing issues that was also encountered during experimentation. Table 11 shows the corresponding bead dimensions that were obtained with the process parameters utilized in Table 10. As such our initial goal of developing parameters for a larger bead were met, it was now critical to ensure that the overall build of the "cruciform" would have a repeatable quality.

Table 10: optimized process parameters for larger beads

Material	Power $_{LENS}$ (W)	Travel speed (in/min)	Powder flow (g/min)
SS 316L	**825**	**15**	**8.24**
PH48S	**825**	**15**	**8.36**

Table 11: Single Bead characteristics with new process parameters

Material	Height (m)	Depth (m)	Length (m)	overall height (m)
SS 316L	452.1	563.3	1828.3	1013.9
PH48S	530	419.6	1888.7	945.5

To ensure the cruciform would be built properly, it was important to ensure we had the proper hatch spacing for our selected layer height of 700 microns. A series of 10 layer builds were performed with the layer height at 700 microns and by varying the hatch spacing we would see which would yield the closest to the 10mm build height. Results shown in Figure 80 show that hatch spacing between 1000 and 1125 microns would yield the best outcome so after final tests hatch spacing of 1050 microns was chosen.

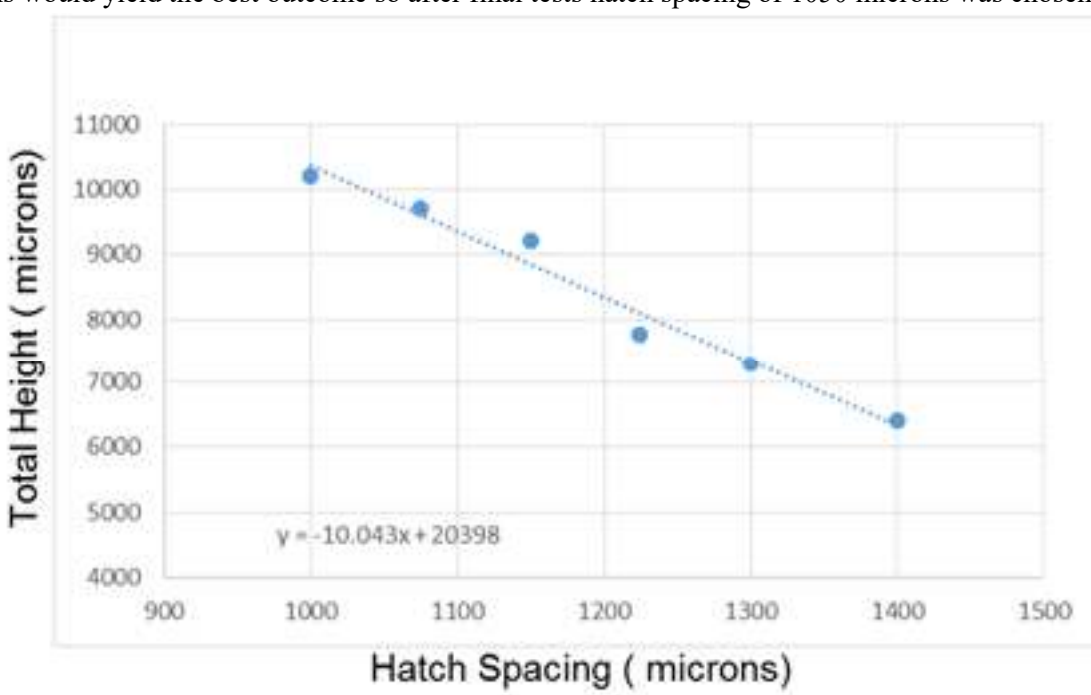

Figure 80 – plot of total build height of 10 layers (bead size ~ 1mm) vs. hatch spacing

Once the single larger bead was carefully vetted and selected based on all these parameters described above, the aim was to see if this relationship would remain for larger multilayered builds and ultimately for the "cruciform". An example of a multilayer sample is shown in Figure 81. For the desired

parameter, a set of three samples of size 12.216.528.6 (WHL) cubic mm's were built and were then analyzed for microhardness and microstructure.

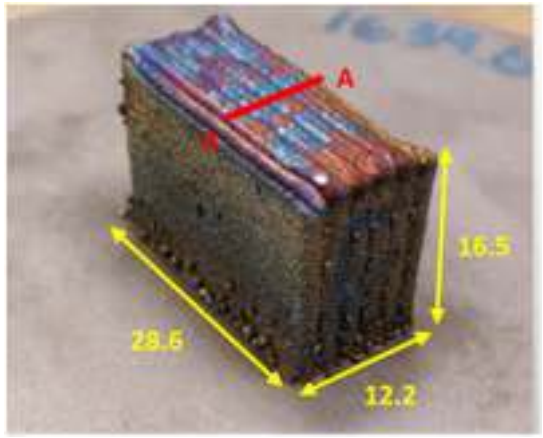

Figure 81. Multilayer builds (measurements in mm)

The microhardness was measured with a Mitutoyo harce of 0.2 Kgf and a 10 second dwell time. It should be noted measurements were taken at other locations along the build direction as part of our larger study, and the results were the same as those presented here in the midsection A-A (see Figure 81). Afterwards, the cross section of the samples were mounted, grinded and etched (see Figure 82). Vickers hardness measurements were carried out on the cross sectional area of each of the three samples built per build number. As shown below (see Figure 82), nine independent microhardness measurements (three in each section – top, middle, and bottom) were taken on the cross section of the as built samples.

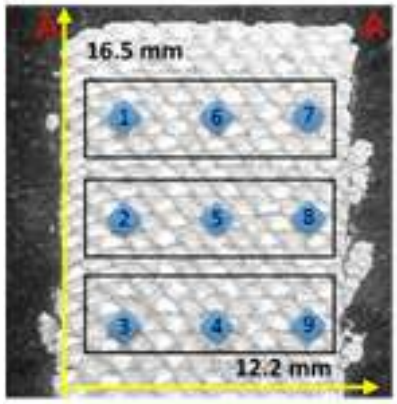

Figure 82. View of cross sectional area (A-A from Figure 79) of samples in which three regions for measurements were selected (top, middle and bottom) and the locations of each individual reading

In addition to the microhardness, the microstructure was also analyzed (see Figure 83) and as compared to Figure 78 it is clear to see that the larger bead size has had an effect and creates larger grains. Furthermore as shown in Figure 83 are the results obtained from the measurements described in Figure 82 and shows the average of the measurements. For the 316L larger bead size we had no underbuilding which means the dimensions matched that of toolpath. That is critical as far as repeatability and that while our values were slightly lower as compared to our smaller bead size (230 HVN) we still had a Vickers hardness

(216 HVN) equivalent to that of wrought 316L (213 HVN) so the process parameters selected are acceptable.

\

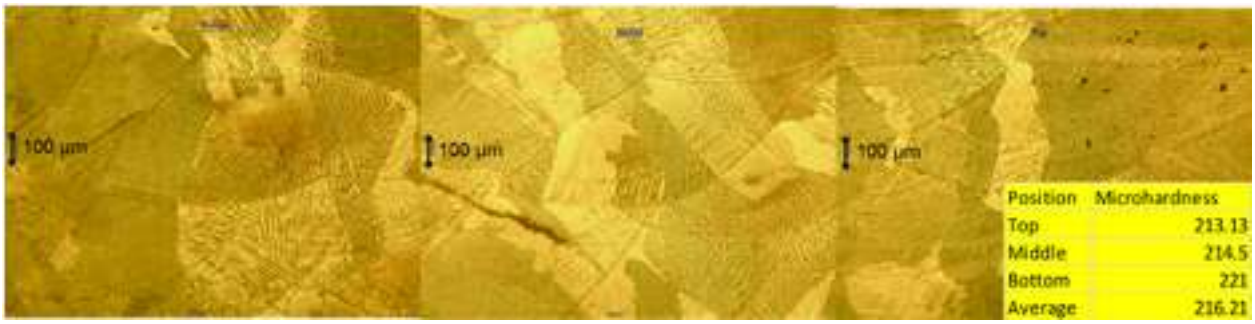

Figure 83 - representative microstructure of 316L with larger bead from left to right (left) bottom of multilayered sample, (middle) middle portion of multilayered sample, (right) top of multilayered sample.

With these process parameters setting the current calculation reduces build time from ~20 hours down to 9 hours which is a significant improvement with the increase of the bead size. The goal is now to see if it is possible to utilize the new beads and processing parameters to reduce porosity and perhaps optimize build path and parameters for further improvement.

The final aspect to be analyzed in process parameter improvement for numerical and experimental optimization is the energy of the process. All the builds for the work performed in this project were done on a LENS 850 M system in which the deposition head moves in x and y and the build plate moves in the z direction (see Figure 84). Two custom built, in-situ process monitoring devices were utilized for this work, one has capability to measure powder flow in real time [3], the other can monitor the energy density during builds [4]. These devices were part of a larger study taking place at NIU's Advanced Research of Materials and Manufacturing (ARMM) Lab on process monitoring and property control for MAM [2] which was sponsored by NIST MSAM. An in-situ acoustic emission sensor in the LENS monitored the powder flow as a function of time (Figure 84), in this way the mass flow rate can be independently tracked during the build [3]. The presence of the sensor is critical to determine the appropriate powder flow since the powder flow has a strong influence on the balance of the available energy.

As described in [4], the power measurement calorimetric system (PMCS) has the ability to measure things like net power (P_{net}) or average power as we call it in the graph (see top right corner of Figure 84) and the energy transferred during MAM processing which allows for a very accurate calculation of energy of the build process. Furthermore, efficiencies of the MAM processes can be calculated as in [2], which can contribute to a greater understanding of the resultant metallurgical properties of various build parameters. This data was helpful for TASK 2 in enabling them to have real data sets of energy to validate their models.

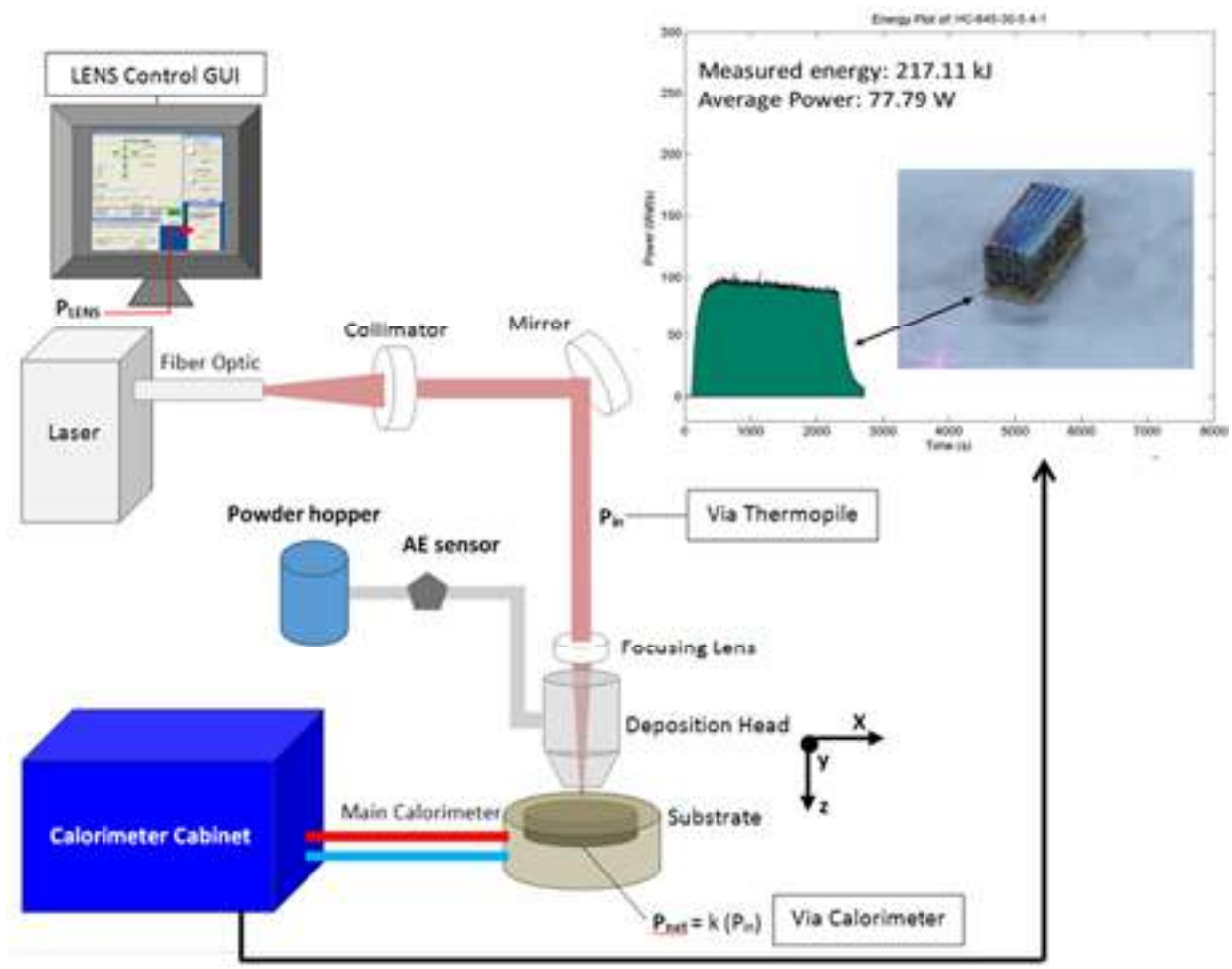

Figure 84- Schematic of LENS set up with AE sensor for powder flow and power measurement calorimetric system (PMCS) utilized to monitor net heat input among other things. Deposition head moves in X and Y and build plate moves in Z. Top right is the output data from the power measurement calorimetric system (PMCS) which provides the integrated energy (kJ) as the sample is being built. This information provides a metric for future process control.

Looking at the energy plots for 316L of parameter sets utilized in Table 1 and Table 2 (see Figure 85) shows a difference in the average power from 80W to ~90W. There is an increase of 10 W of power may explain for the larger grain sizes seen in the microstructures of the build using parameter set in Table 2 that yielded the larger bead.

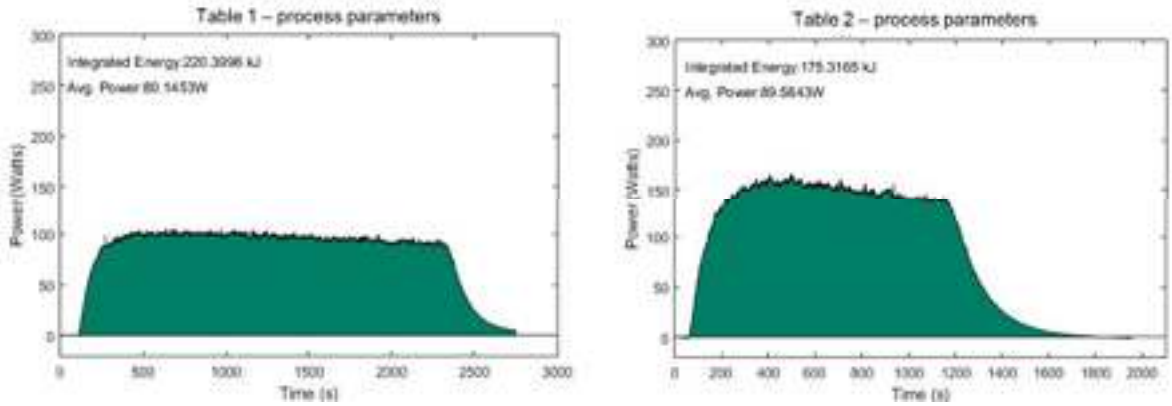

Figure 85 – Calorimeter outputs from (Left) Table 1 process parameters (Right) Table 2 process parameters

C. Validation of process parameters for PH48S

Since extensive work was performed on the 316L to develop the process parameters for the larger bead the next step was to perform the builds utilizing the PH48S which we received at the time of the final parameter development. With that we took these parameters as shown in Table 2 as our starting point for the multi-layer sample build and then the cruciform build analysis.

Once the powder was received from QuesTek we started with the powder flow analysis. The powder flow analysis was performed using the sensor which is described in detail in [3] and the schematic is shown in Figure 84. The results shown in Figure 86 show that the powder flow of the PH48S was similar to that of the 316L and that it would be possible to start with the prescribed powder flow of 316L. After a few preliminary trials the optimized parameters were obtained and are shown in Table 12.

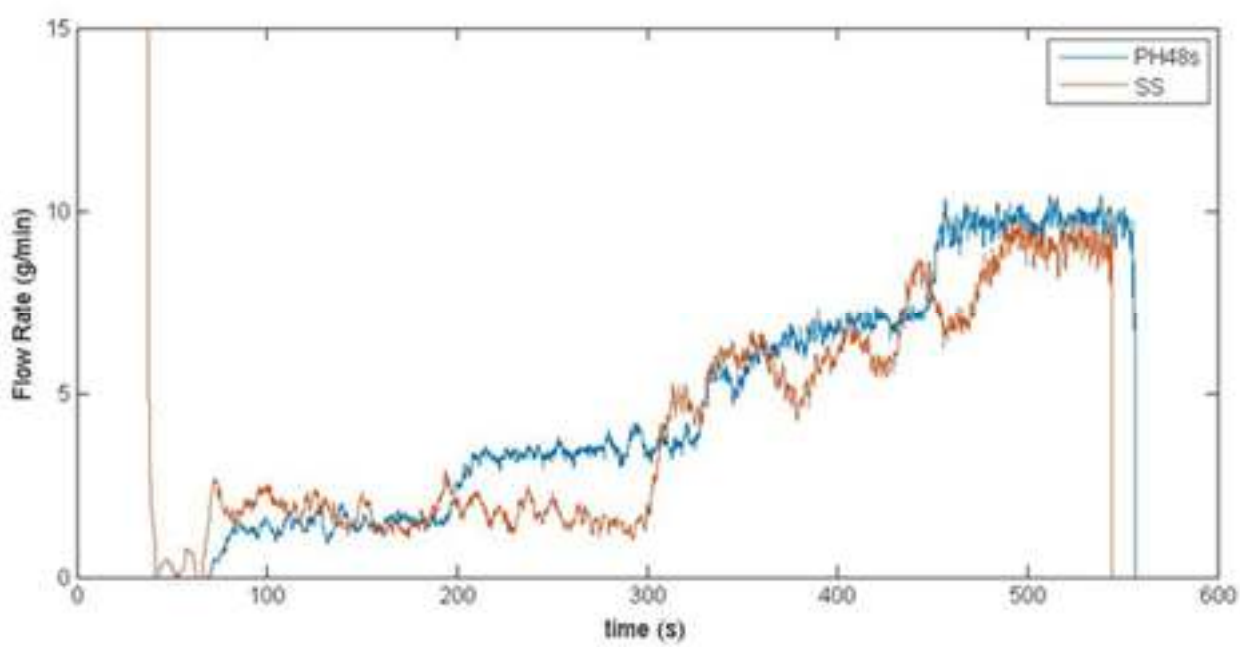

Figure 86 – Powder flow analysis of 316L and PH48S utilizing AE sensor described in [3]

Table 12: updated process parameters for PH48S builds

Actual power (W)	Travel speed (in/min)	Powder flow (g/min)	Hatch spacing (m)	Layer height (m)
710	25	10.4	1050	700

With the parameters described in Table 12 the process of building three multilayered samples was repeated. Figure 87 shows the corresponding microstructure obtained in the multilayer sample. Table 13 shows the microhardness values for the various regions described in Figure 82. Looking at the microstructure small micro pores can be observed. The microhardness values showed a similar trend to that of 316L in that hardness increased from top to bottom. One important thing to note is that the build time was reduced by 3× as the build time declined from 45 minutes to 15 minutes.

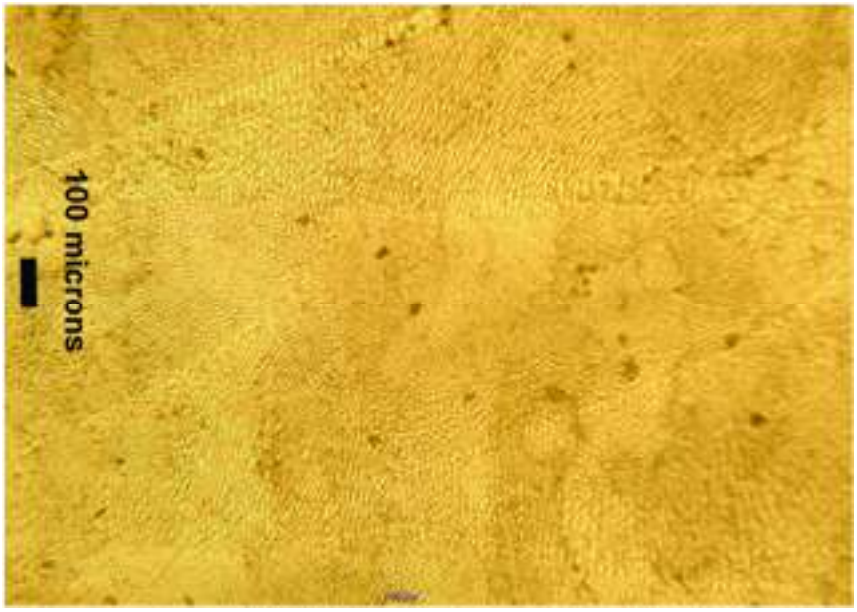

Figure 87 – representative microstructure on the top of the multilayered sample with PH48S.

Table 13: Vickers hardness values from PH48S multilayered samples

Location	Vickers Microhardness (HVN)			Average (HVN)
Top	**309.5**	**310.8**	**332.0**	**317.4**
Middle	**316.0**	**311.9**	**339.0**	**322.3**
Bottom	**330.4**	**362.9**	**347.8**	**346.9**

With the new process parameter settings a preliminary 0.25" tall cruciform build to validate toolpath with larger beads. The build time for 0.25" cruciform build was 22:43 minutes as such for full size build cruciform would be approximately 6 hours (on target to what was predicted). Figure 88 shows two cruciform that were built using the new parameter settings the left is the 0.25" and the right is a 2" cruciform that was built which took 3 hours so time was validated. The issue with the new build was the low powder efficiency, in that a large amount of powder was not captured and started to fuse on the bottom of the cruciform. From a production standpoint this would not be acceptable to lose so much powder during production.

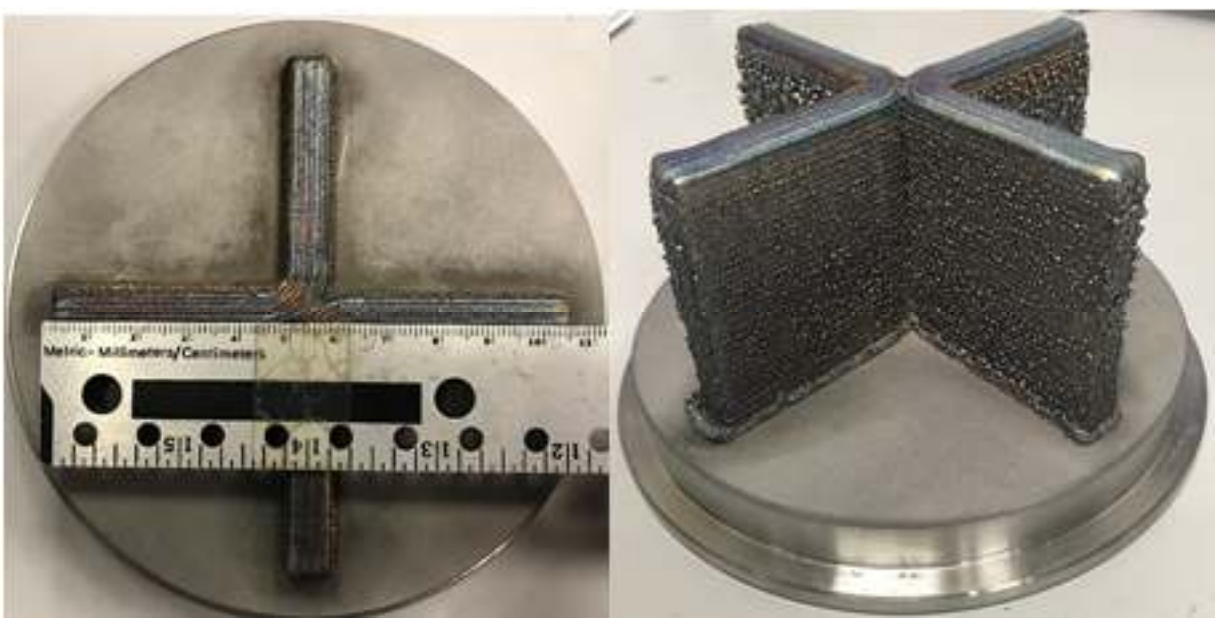

Figure 88 – New cruciform builds (left) 0.25" build, (right) 2" build, notice bottom of cruciform where excess powder was sitting and fused to the sample

A microstructural and microhardness analysis was performed on the 2" build to compare with the values obtained in the PH48S multilayered samples. Figure 89 shows the region where the analysis was performed on the front facing arm of the cruciform. Analysis 1 is looking at the straight portion of the cruciform arm and Analysis 2 was carried out on the curved portion of the cruciform.

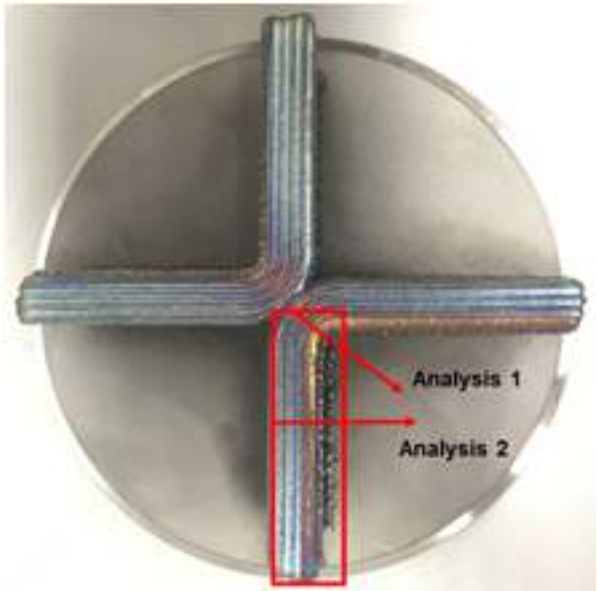

Figure 89 – top view of cruciform showing where analysis was performed

Figure 90 shows a close up view of the arm that was sectioned and utilized for the analysis. This is the front facing arm with respect to the build chamber and is shown in Figure 89. The sample was cut into 12 pieces and are labeled accordingly. Analysis 1 are the regions labeled 4, 8 and 12 which are the curved portion of the arm. Analysis 2 are the regions labeled top (1-3), middle (5-7), and bottom (9-11).

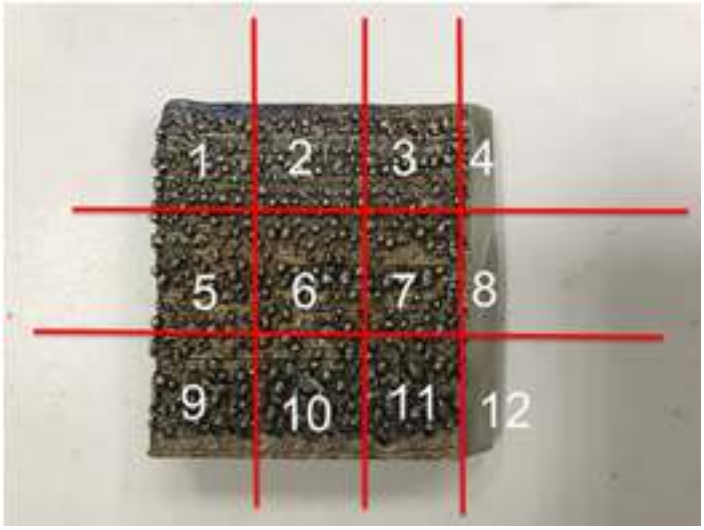

Figure 90 – view of cruciform arm that was cut into sections for metallurgical and microstructural analysis

Table 14 shows the Vickers microhardness measurements taken in each region, again like in the multilayered samples at least three measurements were taken in each region and the average value is shown for that corresponding region. The cruciform arm analyzed here shows that there is not a similar trend with regards to hardness from top to bottom as in the 316L. Here the bottom region (9-11) on the straight portion have the lowest hardness and the middle and top are similar. On the curved potion the bottom region (12) has the highest hardness and the middle is lower than the top. More work is needed.

Table 14: Vickers hardness for the regions shown in Figure 90

Vickers Microhardness (HVN)				
1	**2**	**3**	**AVG**	**4**
337	320	316	324	334
5	**6**	**7**		**8**
321	356	324	334	291
9	**10**	**11**		**12**
274	333	310	305	353

Looking at the microstructure we noticed a few differences compared to what was seen in the 316L cruciform. These show some consistencies with the microhardness values. Figure 91 shows representative microstructures from the bottom region (10&11) which has more porosity than previously obtained with the 316L samples. This could explain the lower hardness values measured. Figure 92 shows microstructures from the curved portion regions (4&12), when comparing to the 316L cruciform builds there seems to be a reduction in pore size and amount from those previous builds.

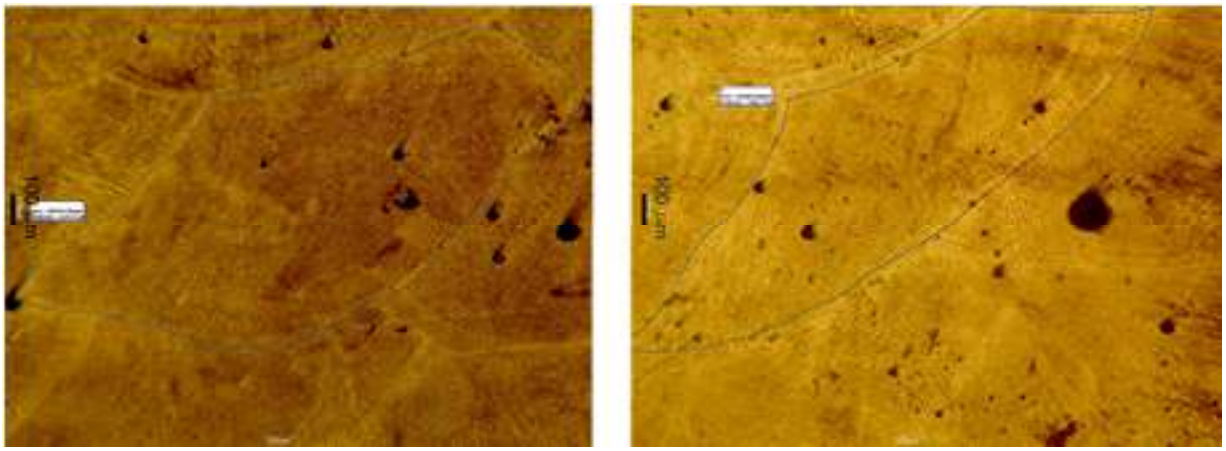

Figure 91 – microstructure of bottom regions in cruciform, (left) 10 and (right) 11 showing porosity

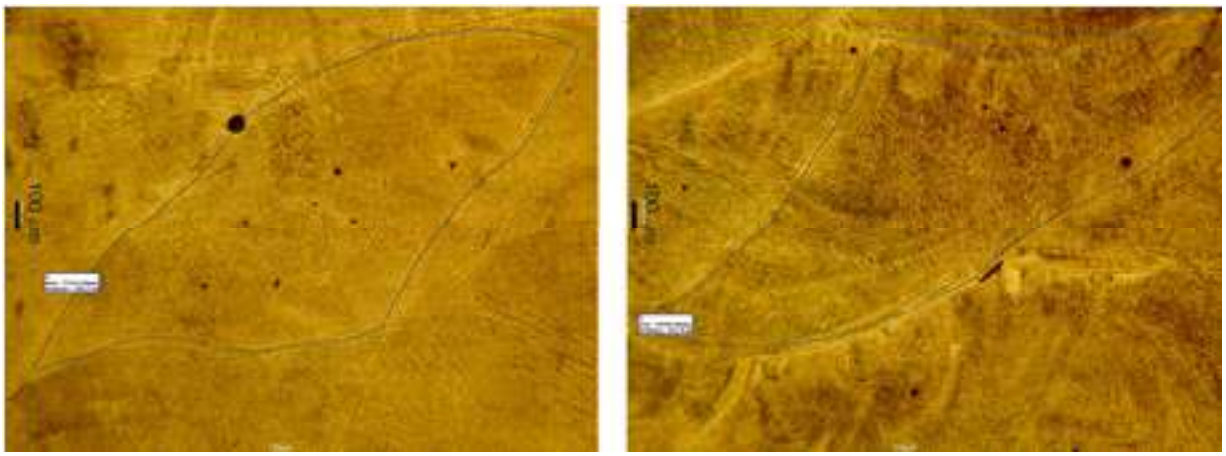

Figure 92 – microstructure of curved regions in cruciform, (left) 4 and (right) 12 showing little porosity

This shows that while improvements were made as desired on the curved regions, however there were some issues with regards to the straight portions that had not been seen in the 316L. If we recall Figure 87 from the multilayered samples where we did see some porosity and thus further investigation on this is required. The first thing was to investigate the powder flow and the spread that may be occurring during delivery of powder. Spread is shown in Figure 86 and corresponds to the delta at a given powder flow. Table 15 shows in fact that the flows are similar and that the spread for PH48S is lower than that of the 316L. During this analysis it was discovered that center purge in the main nozzle has an effect on porosity to some degree but also assisted with removing excess powder. In order to come up with the appropriate reduction of porosity a DOE was carried out to optimize the powder flow as it pertains to center purge flow and gas assist in nozzles. With this work is was possible to eliminate the porosity issues as a result of these changes. The modification was to increase the center purge pressure from 25 L/min to 30 L/min.

Table 15: Powder flow and spread for 316L and PH48S respectively

Material	**Average (g/min)**	**Spread (g/min)**
316L Cruciform	8.24	3.29
PH48S Cruciform	8.36	2.86

The final analysis carried out on validating the process parameters for PH48S was to look at the calorimeter data. Figure 93 shows the calorimeter data for the multilayered sample built with PH48S the average power for this is 126W compared to 90W for the 316L. If we look at the average power for the 0.25” and the 2” cruciform they are 142W and 166W respectively which shows they are in the same range.

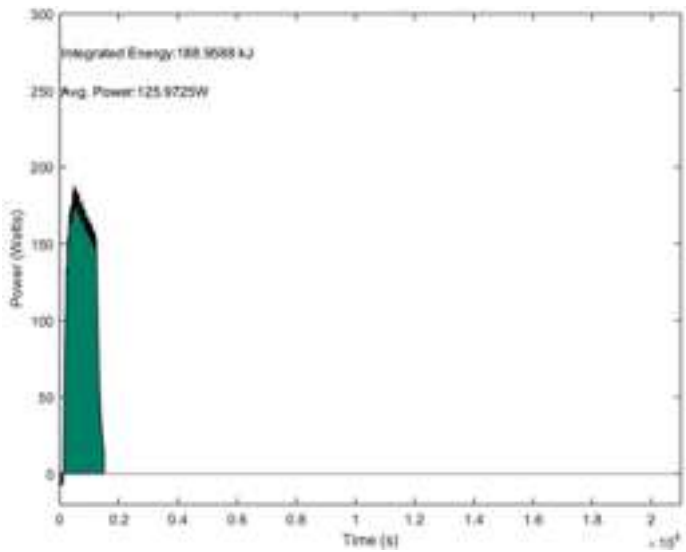

Figure 93 – calorimeter output obtained for multilayered sample using Table 12 process parameters

D. Thermal analysis of cruciform build

As mentioned one of the main objectives in this task was to provide task 1&2 with enough experimental data so that they could validate their models. We have already provided microstructural and mechanical properties and some information from the calorimeter we also wanted to provide thermal data in the form of thermocouple and IR data so that Task 1 & 2 could validate their thermal models. Figure 94 shows the build chamber as well as top view schematic to show where thermocouples were placed to record ambient temperatures in various parts of the chamber to monitor the thermal conditions during the builds.

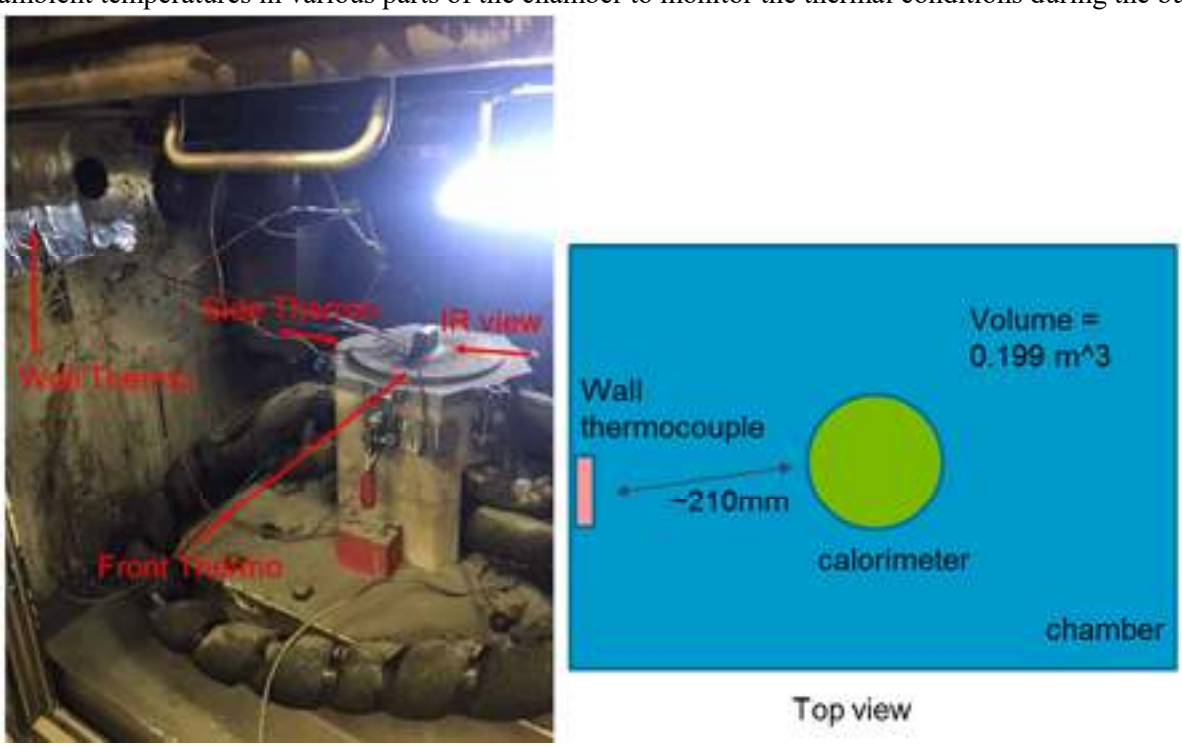

Figure 94 – (left) view of build chamber with thermocouple placement, (right) top view schematic of chamber

There were three thermocouples placed near the build zone of the multilayered sample in order to track thermal profiles during the build. Table 16 lists the positions of all the thermocouples used for this thermal analysis and it should be noted that these are relative to the center of the build plate surface. For this experiment the optimized build parameters provided in Table 12 except for the build height which was changed to 800 microns were utilized. For this experiment an additional PH48S multilayered sample was built. Figure 95 shows the sample built with positions of the thermocouples that recorded the information. It is important to note that the results (microstructure and microhardness) of the multilayered samples were exactly the same as those described above and so the thermal profile would now allow the members of Task 1&2 to have needed data to validate our experimental findings. In addition to the thermocouple, IR data was also collected and provided to the other tasks.

Table 16: position of all thermocouples used for thermal profile collection

Thermocouple	T 1 (mm)	T 2 (mm)	T 3 (mm)	Front (mm)	Side (mm)	Wall (mm)
X from plate center	-15.875	-23.8	0	12.7	66.4	-270
y	-7.14	-5.16	-26	-66.4	0	-126
z	0	0	0	30.5	30.5	105

Figure 95 – view of build and locations of thermocouples

The thermal data obtained was very consistent across the build plate as well as those recording the ambient temperature. This data was then sent to the task 2 to help validate their thermal models. Looking at Figure 96, it can be seen that Thermocouple 2 which is closest to the build and also perpendicular to the laser travel direction showed the highest temperatures (~470ºC). Thermocouple 1 maxed out at ~140ºC. Thermocouple 3 which was parallel with the laser travel direction and showed a more constant temperature that hovered around ~90ºC. All of these had very similar cooling trends. Looking at Figure 97, it can be seen the ambient temperatures closest to the build plate did reach a max of 70ºC however the one furthest away only increased by 3ºC from 26.5-29.5ºC over the span of the build. This enables the models to know that there is minimal effects on the environment. Again looking at the cooling trends a similar pattern is seen as those on the build plate.

At the request of Task 2 and additional test was run with thermocouples on the plate but further from the build again to develop a more comprehensive picture of the thermal profiles. Figure 98 shows the location of the thermocouples as well as the results. Again it can see that the trends are very similar to the previous build and that this data was very useful for Task 2 to build there thermal models.

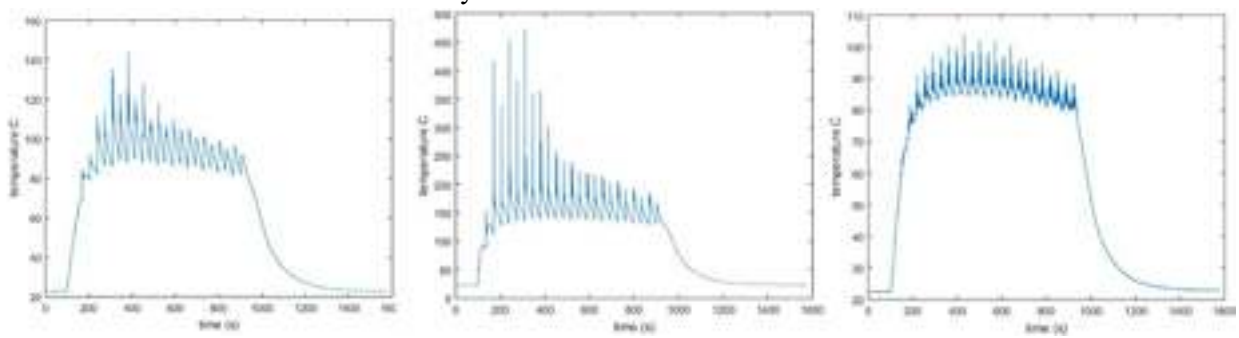

Figure 96 – Thermal data from left to right of Thermocouples 1-3

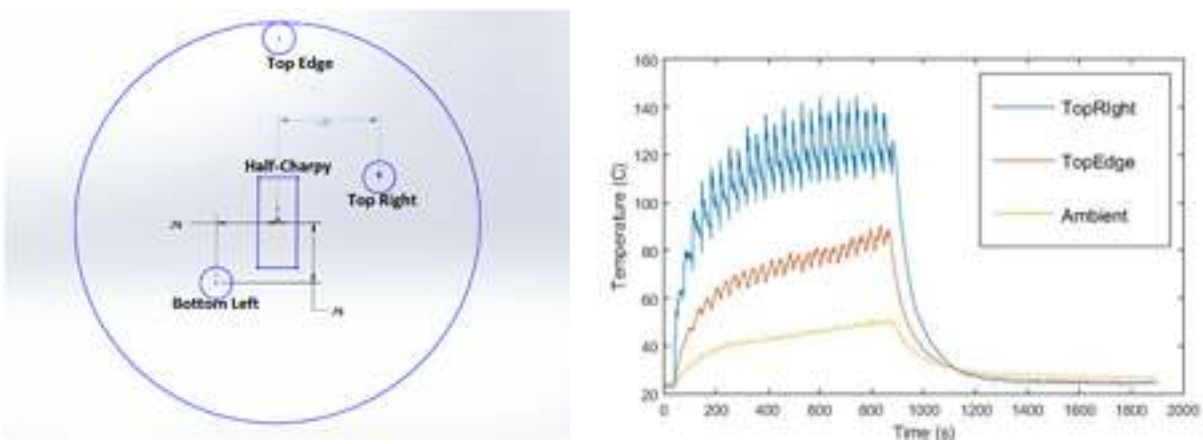

Figure 98 – (left) schematic of location of thermocouple for additional test (right) Thermal data from experiment showing similar results from previous test. It should be noted that bottom left detached and the data was removed

As mentioned previously in addition to the thermocouple data, we also utilized a FLIR A320 IR camera which has a high sensitivity of <50mk to spot minor temperature differences, and an image quality of 320 x 240 pixels. The threshold temperatures need to be adjusted and so two different set of experiments were done. One at a lower temperature to confirm cooling rate and the other at higher temperature to see the overall thermal history of the build. All this data is available as part of the deliverable items. Figure 99 shows a screen capture of the video taken during one of the builds when measuring the cooling rates. In

fact there were 9 virtual locations taken (see Figure 99) and the corresponding plots of those locations. Through previous experimentations the emissivity of 0.79 was utilized. Looking at Figure 99 the cooling trends are very consistent from each of the 9 locations. In fact the cooling rate at the top was measured to 214 K/s and Task 2 had obtained a cooling rate in the same region of about 300 K/s so it seems there was good agreement and that experimental data provide beneficial to their work.

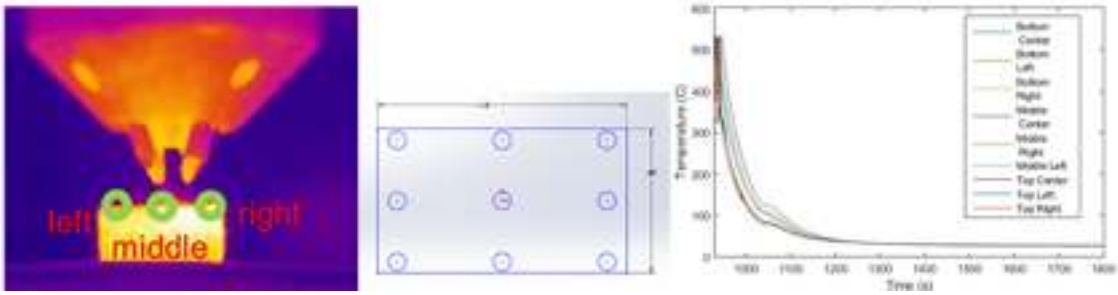

Figure 99 – (left) screen capture from IR video (middle) the 9 regions were temp data was extracted over time (right) plot of the data extraction from the 9 regions over time.

With the second trial the higher temperature range was utilized to see how the overall thermal history for the build was. It was now possible to track thermal history layer by layer. Here referring to Figure 99 a thermal profile from the middle region is shown in Figure 100 along with a close up view of the time that shows the thermal history for each layer built. This kind of data was very critical for reviewing the results obtained in Task 2. It shows the sharp peaks as the laser approaches the side of the build in which our camera is looking.

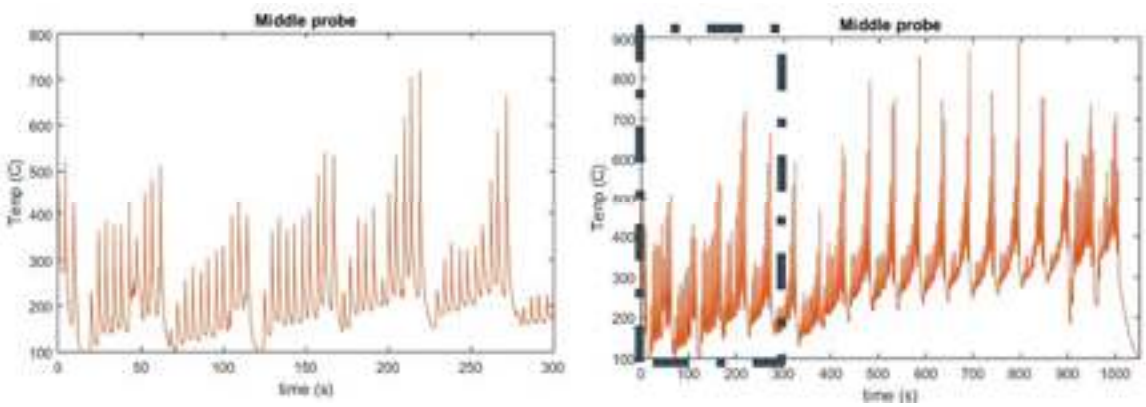

Figure 100 – (right) close up view of the thermal profile shown left (box region) that indicates each layer and the breaks in between as the thermal profile changes.

E. Final Validation and Verification of PH48S Cruciform

With all the work accomplished the final goal was to ensure we have the ability to repeatedly build the "cruciform" sample with the consistent properties. Prior to full build we managed to build a half sized cruciform with full data available (calorimeter, thermal and IR). Table 17 shows that the entire cruciform has very consistent data throughout build. The data was taken as similar to Figure 90. Here we can see on the bottom row that the average Vickers hardness was top: 350 HV, middle: 361 and bottom: 352HV. The build time is within specified time frame (8 hours total build time if completed). Each arm of cruciform shows consistent results (average pore size less than 30 microns). See Table 17 below for full results on representative arm of cruciform. We have therefore found best process parameters for repeatable results

and they are given in Table 18. IN addition to the settings through our work with TASK 2 team it was realized that best build path was to outline the cruciform first and then perform an interior raster of the cruciform with 90 degree rotation of raster during each layer.

Table 17: full data set of cruciform arm for final parameter settings

Sample	Bead Area			Bead Perimeter			Bead Height			Pore radius				Microhardness		
	Top	Middle	Bottom	Top	Middle	Bottom	Top	Middle	Bottom	Top	Middle	Bottom	d spacing	Top	Middle	Bottom
1B	785371.0	619064.0	511484.0	4319.0	4227.0	4202.0	660.0	530.0	506.0	18.3	17.0	20.0	7.1	396.9	481.6	408.4
2B	592291.0	595570.0	810411.0	4360.0	4236.0	4378.0	485.0	570.0	646.0	30.0	32.0	32.0	7.4	298.3	304.2	299.9
3B	588076.0	606667.0	677797.1	4365.3	4265.3	4366.7	507.0	546.0	575.3	23.8	29.2	33.2	6.5	257.0	244.7	253.2
4B	644427.2	655463.2	677588.6	4302.2	4220.3	4212.0	548.3	548.1	582.5	23.4	22.8	26.5	5.3	427.9	491.4	505.0
5B	562284.0	681750.0	592578.0	4140.0	4487.0	4216.0	484.0	544.0	521.0	24.0	28.0	16.0	4.5	332.7	326.3	330.8
6B	[illegible]	[illegible]	[illegible]	[illegible]	[illegible]	[illegible]	[illegible]	[illegible]	[illegible]	[illegible]	[illegible]	[illegible]	[illegible]	[illegible]	[illegible]	[illegible]
7B	[illegible]	[illegible]	[illegible]	[illegible]	[illegible]	[illegible]	[illegible]	[illegible]	[illegible]	[illegible]	[illegible]	[illegible]	[illegible]	[illegible]	[illegible]	[illegible]
8B	[illegible]	[illegible]	[illegible]	[illegible]	[illegible]	[illegible]	[illegible]	[illegible]	[illegible]	[illegible]	[illegible]	[illegible]	[illegible]	[illegible]	[illegible]	[illegible]
9B	[illegible]	[illegible]	[illegible]	[illegible]	[illegible]	[illegible]	[illegible]	[illegible]	[illegible]	[illegible]	[illegible]	[illegible]	[illegible]	[illegible]	[illegible]	[illegible]
10B	[illegible]	[illegible]	[illegible]	[illegible]	[illegible]	[illegible]	[illegible]	[illegible]	[illegible]	[illegible]	[illegible]	[illegible]	[illegible]	[illegible]	[illegible]	[illegible]
11B	[illegible]	[illegible]	[illegible]	[illegible]	[illegible]	[illegible]	[illegible]	[illegible]	[illegible]	[illegible]	[illegible]	[illegible]	[illegible]	[illegible]	[illegible]	[illegible]
12B	[illegible]	[illegible]	[illegible]	[illegible]	[illegible]	[illegible]	[illegible]	[illegible]	[illegible]	[illegible]	[illegible]	[illegible]	[illegible]	[illegible]	[illegible]	[illegible]

Table 18: final process parameters for repeatable PH48S cruciform build

Actual power (W)	Center purge (L/min)	Gas assist (L/min)	Travel speed (ipm)	Powder flow (g/min)	Hatch spacing (m)	Layer height (m)
750	30	3.5	25	7	1050	700

In the end it was possible to build two full sized cruciform (see Figure 101). One was delivered to QuesTek for further analysis the other is being analyzed here at NIU. All the data related to this thermal profile was delivered to the team in Task 2.The build was within the anticipated time of 8 hours. We expect that both builds will be similar and should have all requisite data to demonstrate the repeatability. We also plan on putting all the data together for final delivery as data sets.

Also in Figure 101 it is possible to see the locations of the thermocouple positions that provided the thermal data for Task 2. Figure 102 shows the thermal profiles obtained for the build the peak in the build was a glitch with the calorimeter but as can be seen there was no issue with overall data, this information should provide useful for task 2.

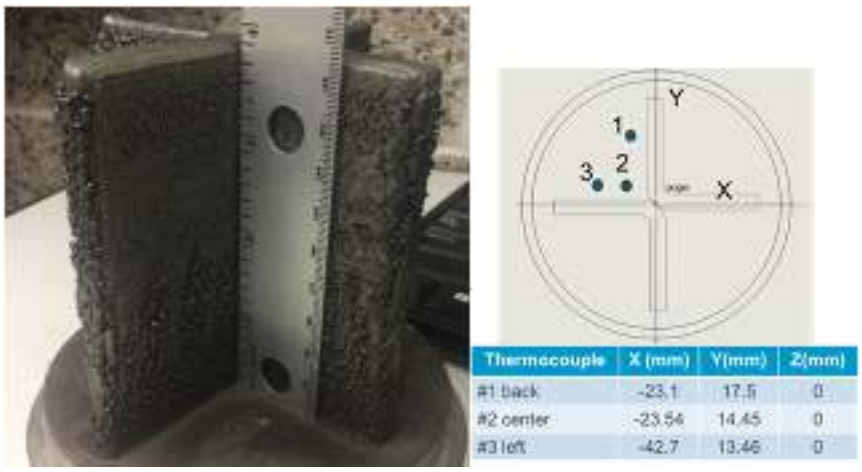

Thermocouple	X (mm)	Y(mm)	Z(mm)
#1 back	-23.1	17.5	0
#2 center	-23.54	14.45	0
#3 left	-42.7	13.46	0

Figure 101 – (left) full cruciform build done in 8 hours which is a drastic improvement from the initial 20 hours (right) location and position of thermocouple for final build

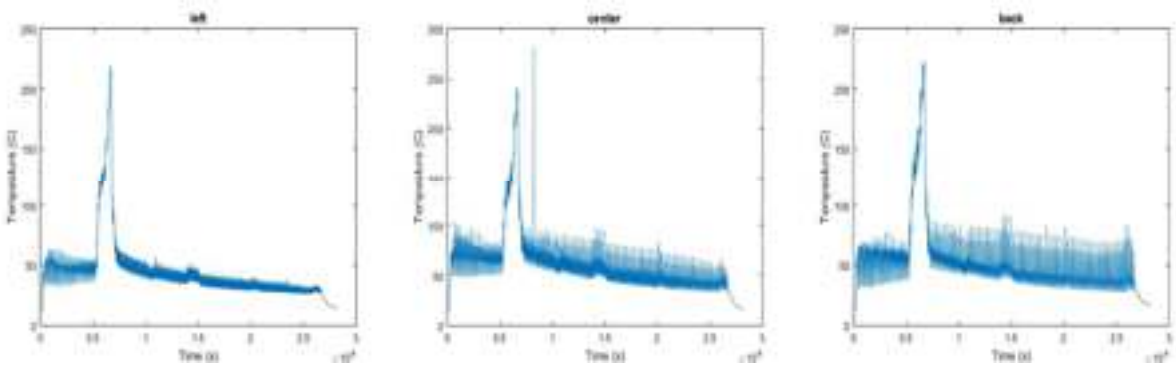

Figure 102 – thermal profile of the cruciform build over the 8 hour period (glitch seen at 0.6 sec. (left) TC#1, (center) TC#2, (right) TC#3.

Task 5 was able to develop a repeatable sample that originally took over 20 hrs. to build in under 8 hours. Additionally, it found the appropriate processing parameters by using both physical and digital meta models of the AM processing parameters. These models can be run for a wide range of data sets to economically build a response surface to identify local maximum and minimum and quickly identify process tolerant production parameters. Future work will need to focus on design for process optimization metrics.

References

[1] B.E. Carroll et al. / Acta Materialia 87 (2015) 309–320
[2] Sciammarella, F.M., "Development and Validation of Physics-Based AM Models for Process Control and Quality Assurance", Final Report for National Institute of Standards, COA 70NANB13H194, 2016
[3] Whiting J.,Springer A., Sciammarella F.M., "Real-Time Acoustic Emission Monitoring of Powder Mass Flow Rate for Direct Energy Deposition", under review, Additive Manufacturing Journal.
[4] Malin V., Sciammarella F.M., "Controlling Heat Input by Measuring Net Power", Welding Journal, pp. 44-50, July 2006

V. ACCESSING THE TECHNOLOGY

A. Background Intellectual Property

Siemens NX software is a proprietary software. It will be licensed to some of the Project Team members during the project performance period, in order to enable the development of the project deliverables. However, Siemens NX software will not be part of the deliverables.

GAMMA (Generalized Analysis for Multiscale Multiphysics Applications) is early stage software that has been developed by Northwestern. It will be licensed as needed to Project Team members during the performance of this project, in order to enable the development of project deliverables. GAMMA will not be part of the deliverables.

Optimal Design of Experiments, Gaussian process modeling, and Bayesian calibration and bias correction software tools were developed previously at Northwestern by Professor Wei Chen's group under the support from NSF. These tools are currently integrated into the Siemens NX software. Access to these tools will be subject to the restriction of "government purpose license rights from a prior contract".

B. Technical and Systems Requirements

Availability of input/output functionalities from each software component or database that need to be connected with the software framework (e.g. Material and Process Data Structures, Manufacturing Process Simulator, Model Calibration). These functionalities need to be able to import/export the data needed by the other software components in a documented format.

Availability of methods/modules to translate predicted microstructural material properties into macrostructural material data, usable by the chosen CAE software package for virtual mechanical testing. NX software and interface formatting provided by Siemens to the entire team.

Ongoing small manufacturing business support and recruitment as well as workforce training and certification.

VI. INDUSTRY IMPACT & POTENTIAL

Company Type: Any manufacturer or low-volume or one-of-a-kind metallic parts
User Position: Manufacturing Engineer
Industry Segment: Aerospace, Tool and Die, Energy, Medical, Oil & Gas
Technology: Additive manufacture or casting of low-volume metallic parts

Source: http://www.metal-am.com/introduction-to-metal-additive-manufacturing-and-3d-printing/growth-areas-and-market-potential/

Figure 103: Additive manufacturing market share globally.

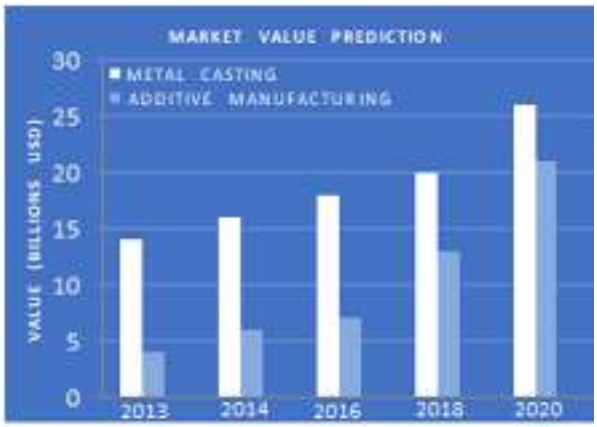

Sources: https://www.3ders.org/articles/20160509-3d-printing-industry-to-reach-21-billion-by-2020-ups-and-cta-report-shows.html
http://www.gordonbrothers.com/insights/industry-insights/machinery-and-equipment-die-casting

Figure 104: Market values of metal casting and additive manufacturing from 2013 to predicted marked value in 2020.

This technology establishes the potential for **guiding future advanced manufacturing** to adaptive Bayesian inference algorithm to quantify process uncertainty

- Extend the method **to other manufacturing processes** to integrated workflow for material microstructural evolution and its influence on mechanical properties
- Increase the **awareness of GPGPUs for numerical modeling**, and their ability to reduce computational performance bottleneck
- Equip SMEs with advanced and integrated simulation tools to **low the barrier for incorporating** advanced manufacturing processes in the early design stage

VII. TECH TRANSITION PLAN & COMMERCIALIZATION

A. Future Plans

- Integrate the structure-property metamodels to GAMMA
- Add more design optimization capability to GAMMA
- Investigation potential for commercialization as an NX add-on
- Document the database and create user manuals
- Organize workshops to disseminate the fundamentals and the package
- Finalize the publications
- Case studies to further test technology
    - Expand virtual model to include optimization of process parameters to achieve desired final part properties
- Further develop technology outcomes (advance TRL)
- Utilize DMDII Partner Innovation Projects platform
- Commercialization partner
    - Work with DMDII industrial members to license this as a software solution to users for testing

B. Identified Barriers to Adoption

- Availability of input/output functionalities from each software component or database that need to be connected with the software framework (e.g. Material and Process Data Structures, Manufacturing Process Simulator, Model Calibration). These functionalities need to be able to import/export the data needed by the other software components in a documented format.
- Availability of methods/modules to translate predicted microstructural material properties into macrostructural material data, usable by the chosen CAE software package for virtual mechanical testing.
- Ongoing small manufacturing business support and recruitment as well as workforce training and certification.

VIII. WORKFORCE DEVELOPMENT

The workforce development and education activities were led by Dr. Federico Sciammarella along with the NIU EIGERlab team of Dr. Rena Cotsones, Mr. Mike Cobert and Ms. Sherry Pritz. The main focus was to leverage the strong network EIGERlab has established over the past decade and ensure the workforce was aware of the digital thread and the advantages of participating in the ensuing activities. A survey was sent out in early September of 2017 (see appendix section 5). The goal was to capture the current status of digital manufacturing among SMEs in terms of their knowledge and comfort with regard to digital manufacturing. The plan was to invite survey respondents to a subsequent series of workshops to better prepare leaders of SMEs for the future.

Survey results: From the survey we were able to determine a significant level of concern about the potential cost of digitalization and a belief that digital marketing was more in the domain of large companies. From this we then sent out an invite to correspondents for a workshop on Digital manufacturing (see appendix section 5) that we held in collaboration with then-Director of Operations Colette Buscemi from DMDII, to provide an opportunity for attendees to see a demonstration of the Digital Manufacturing Commons (DMC).

The event was not well attended and it was the understanding that there had been a tremendous amount of "DMDII fatigue" or skepticism and thus it was difficult moving forward to find ways to re-engage this network of SME's to participate in DMDII events. Unfortunately, there was a perception that previous DMDII meetings had been focused on selling memberships to manufacturers and some of those perceptions have been difficult to shake. Those that were in attendance did have a chance to review the DMC and provided positive feedback. It had been discussed to roll out some Beta version to select EIGERlab member to solicit further feedback on the DMC. A few months later we were informed that DMDII was going to delay any testing of DMC and thus this program was scrapped.

Additional outreach and events: EIGERlab hosted 12 events related to digital manufacturing and facilitated interactions with several other partners. Specifically in support of this project, EIGERlab organized a few follow on events in an attempt to bring in SME's and provide digital awareness (visit https://www.eigerlab.org/events/). On April 20, 2017, more than 100 area manufacturers participated in an event hosted by the Rockford Area Aerospace Network (RAAN), a key EIGERlab partner. Both QuesTek and NIU presented on digital manufacturing (see appendix section 5) and showed the outline of the project and solicited and received some feedback from the audience. EIGERlab opened a slot for the DMDII team to participate in their monthly Innovation Tuesday event in February (see appendix section 5) where there were over 20 participants and the team (Dr. Shah from PDA LLC and Dr. Sciammarella from NIU) provided an update on the project and some of the digital tools developed and how it can help companies expand their capabilities. This event was recorded and is available on the web. The local news channel out of Rockford also did a piece an aired some of the content (see https://www.mystateline.com/news/made-in-the-stateline-eigerlab/976282441). One of the last events was at the RAAN 2018 Aerospace Symposium & Networking Event (see appendix section 5). Here Dr. Saboo from Questek and Dr. Sciammarella from NIU gave a presentation on the accomplishments and capabilities developed during this project. There was additional discussion and exchanges with many interested parties after the presentation. Dr. Sciammarella was the keynote speaker at the Rockford Chamber of Commerce's Manufacturers Dinner(see appendix section 5) , and raised awareness of the DMDII project in his remarks on the future of manufacturing in the U.S. and around the world. There were 400 attendees at this event.

Educational: Please provide any mention of this project in any classes at Northwestern or any correlation to thesis work. A course on additive manufacturing was taught in the spring of 2018 and there were 42 undergraduate and 3 graduate students. They were exposed to digital materials and design (from the work that Northwestern and QuesTek were doing on the DMDII project) as well as the additive process. One of the labs included the examination of several of the PH48S samples we had created for the project. The student's exposure to this project was critical in understanding both the importance of virtual certification and validation and the challenges that these areas still face. Many have expressed interest in pursuing research in the areas of additive, digital design and materials. In addition to this there were seven total students helping out in the ARMM Lab during the course of this project. 5 undergraduates and 2 graduates (one of which started as an undergraduate), the two graduates will finish their master's degree in fall of 2018 and spring 2019 based on the work done in Task 5. One of the graduates directly interacted with PDA LLC on determining key process variables for the experimental work and cruciform demonstration article design and 3D modeling which was initiated by PDA LLC. There are an additional two undergraduates committed to starting their Master's as well in the coming year once they graduate. None of this would have been possible without the support of this program.

IX. CONCLUSIONS/RECOMMENDATIONS

Software developed in this project was embedded within Siemens NX to virtually build parts. Northwestern and QuesTek Innovations LLC integrated different models from process to microstructure with the prediction of mechanical properties. This comprehensive virtual manufacturing toolkit provides linkage among process, structure and properties. This module will quantify the quality of the manufactured part in terms of geometric fidelity and predicted mechanical property based on chosen build head path and other AM variables. The interface with the DMDII's Digital Manufacturing Commons (DMC) shall be explored by working with General Electric (see support letter). This virtual certification tool is of particular value for small and medium enterprises, with limited resources for developing process insensitive efficient approaches to meet OEM requirements. User manual and tutorials were developed for workforce development and tested at DMDII's beta site, EIGERlab. This work is further leveraged through the Chicago-regional NIST-funded CHiMaD (Center for Hierarchical Materials Design) for education and outreach infrastructure already in place. This research will enable quick qualification of components, increase the process autonomy, truly integrate design and manufacturing, and ultimately release this technology from the hands of a few to the hands of many.

X. LESSONS LEARNED

- In calibrating the oxide distribution simulation, difficulty measuring experimental solidification cooling rates in additive processes meant that a more sophisticated calibration method was required. Thus, the training data for the oxide distribution metamodel was generated from the physics-based simulations. This was validated by comparing its predictions to the solutions of full-fidelity physics-based simulations.
- Due to the difficulties obtaining experimental cooling rates for LENS samples and resolving PrecipiCalc simulations for casting, Task 1 and Task 3 decided to put aside the Bayesian calibration for the interfacial energy in oxide formation. Instead, Task 3 gathered several values from existing literature and found an approximate linear relationship between temperature and interfacial energy.
- Comparisons with measured data have highlighted the sensitivities of thermal simulations to parameters including material absorptivity and boundary conditions.

XI. APPENDICES

A. How to Install the NX-based Prototype

The following software packages are prerequisites for the correct installation and functioning of the NX add-on for integrated process certification, as well as the other project deliverables on which the NX add-on depends.

- NX 11.0.2.7, with NX CAM Hybrid Manufacturing Beta Release.
- Python 3.6, with Python packages: paramiko (2.4.0), PyYAML (3.12)
- pip install vtk for Python 3
- Matlab runtime R2016a (9.0.1) (https://www.mathworks.com/products/compiler/mcr.html)
- Oracle VirtualBox 5.2 (needed to utilize the Virtual Box with GAMMA executable)

To perform the software installation, the following steps need to be performed:

1. Unzip the given software archive to the desired installation directory, i.e. C:\rpc_bin.
2. Set environment variable UGII_USER_DIR to the installation directory.
3. Download the folder containing the linux virtual machine with GAMMA and the Voxel database software and start the virtual machine by opening the folder from the VirtualBox manager.

4. Log into the GAMMA virtual machine using login “gamma” and password “gamma”, open a terminal and obtain the IP address by running command “ifconfig”. The expected value is 19288.56.101 but a different address may be assigned on the host-only network if that address is already in use.

Edit the file “gamma.yaml” in the installation directory and set the value for the key “server” to the virtual machine’s IP address.

NIU EIGERlab through our partnership with DMDII would like to help area manufactures implement Digital Manufacturing (DM) in their shops. To do this, we would like you to answer the following questions and return them to Tina Leombruni at tleombruni@eigerlab.org. We will review each questionnaire and put your organization in one of three categories:

- Little to no experience with DM.
- Are using DM in some areas of the organization.
- Are using DM in most of the organization.

We will then invite you to a presentation that will explain how each group can advance the use of DM.

1. Have you heard of digital manufacturing (DM)?

2. How do you define DM?

3. Do you feel it is critical for you to enter into the DM space? Please explain why or why not.

4. Are you doing anything with DM? If so what?

5. Do you feel DM makes you more competitive and in what way it helped?

6. How long did it take you to implement your DM system/operations?

7. What have been the biggest roadblocks to adopting DM if you have already done so and or if you have not implemented it?

8. Are you aware of DMDII? Have you worked with them? If so what was the experience?

9. If you could receive free training in areas of DM what would they be?

10. If at no cost to the company, you could hire qualified employees and or extra help with skills to implement DM within your company would you bring them on board?

11. Have you ever worked with academic institutions/other agencies to aid in the area of R&D?

Innovation, Acceleration and Product Development

Free Workshop on Digital Manufacturing (DM)

Learn from National DM Leaders

NIU EIGERlab through our partnership with DMDII would like to help area manufactures implement Digital Manufacturing (DM) in their companies. On September 21, 2017, we are [illegible]

[illegible]

- [illegible]
- [illegible]
- [illegible]
- [illegible] solutions.

1:00 PM

- Participate in an interactive usability workshop and provide feedback and input on the value of the tools and capabilities available on the Digital Manufacturing Commons (DMC).

Date:	September 21, 2017
Time:	1:00PM
Location:	NIU-Rockford 8500 E. State St. Rockford, IL 61108

Please RSVP to Tina Leombruni at tleombruni@eigerlab.org

The Digital Manufacturing and Design Innovation Institute (DMDII) is the nation's flagship research organization for applying cutting edge digital technologies to reduce the time and cost of manufacturing, strengthen the capabilities of the U.S. supply chain, and reduce production costs. The DMDII will develop, demonstrate, display and commercialize digital design and manufacturing technologies across key industries. The primary channel for DMDII to achieve this goal and attract, engage and impact small and mid-sized manufacturers across the U.S. will be through the Digital Manufacturing Commons (DMC), an on line, open-source platform designed to connect manufacturing communities and enable easy sharing of content, apps and services that help manufacturers achieve new levels of productivity by helping small manufacturers quickly identify and implement digital manufacturing solutions that will either increase revenue or reduce costs.

Innovation, Acceleration and Product Development

Rockford
ILLINOIS USA

Helping Employers Retain & Create Quality Jobs

Look forward to seeing you at the RAAN Aerospace Networking & Symposium April 20, 2017

ROCKFORD AREA AEROSPACE NETWORK
RAAN
EVERY SYSTEM. EVERY AIRCRAFT.

2017 Aerospace Networking & Symposium

Thursday, April 20, 2017

2:00 - 7:00 pm

Franchesco's Ristorante
7128 Spring Creek Rd
Rockford, IL 61107

Event Highlights

Special Guest U.S. Congressman Adam Kinzinger
Great Networking
Door Prizes
Make Key Contacts
Learn from Top Aerospace Companies
Hear From Industry Leaders
Experience Aviation Simulator First-Hand

1

This year's Aerospace Networking and Symposium Event will be a combination of informative presentations/panel discussions and great networking opportunities; and this year in addition to our networking and symposium, UTC Aerospace Systems is offering a facility tour the following morning.

Event Agenda:

2:00 - 2:30 p.m. Welcome & Introductions

RAFDC President & CEO Nathan Bryant
RAAN Chair Khai Vu with GE Aviation
RAAN Co Chair Ron Soave with Kelley Aerospace
Congressman Adam Kinzinger

2:30 - 3:45 p.m. OEM/MRO Panel Discussion

Panelists confirmed to include:

Woodward, Inc.: Jay Viswanathan, Global Supply Chain Leader and Cheryl Brown, Sourcing Supervisor - Supplier Quality Engineering

UTC Aerospace Systems: Larry Palmer, Supply Chain Manager, New Products Introduction and Eric Cunningham, Senior Director Supply Systems Operations

GE Aviation: Kevin Wiele, Plant Leader and Theresia Becker, Quality Leader
AAR: Darren Siegel, OEM Aftermarket Solutions - Commercial

3:45 - 4:00 p.m. Networking Break

4:00 - 5:15 p.m. Process & Strategy Professional Services: Bob Gurt, "Talent Pipeline Management"

SME Speakers: Novel Technologies Discussion

Speakers confirmed to include:

QuestTek: Karem Iosen, "Innovations on New Metals for Aerospace"

Comply 365: Tom Samuel, "Digital Benefits to Aerospace Companies"

Forest City Gear Co.: Fred Young, "Innovation on the Shop Floor"

N.J.: Dr. Federico Scammacca, "Additive Mfg in the Aviation Industry"

5:15 - 7:00 p.m. Informal Networking

Questions? Contact information@RockfordIL.com or call 815.987.4253.

2

Innovation Tuesday

February 2018 | "Latest Tools for Manufacturing"

During February's Meetup, leading experts in this field will introduce you to the latest tools to virtually test materials and manufacturing processes such as casting and additive manufacturing. This Meetup is your chance to see how these tools can assist you with growing your business or help to improve your existing business. Determine how to partner with these leaders to help to assess your needs and determine how to begin. As always, EIGERlab is positioned to assist with your success. February's Meetup will be the first in a series regarding development capabilities so don't miss out.

NIU College of Engineering | Federico Sciammarella
NIU EIGERlab | Mike Cobert
Product Development & Analysis | Jiten Shah
Questek | Abhinav Saboo

Video link to presentation: https://youtu.be/0_G9F4Ww_08

Aerospace Networking and Symposium

2018 Aerospace Symposium & Networking

Aerospace Symposium & Networking
Thursday, April 26 from 2:30 – 7:00 pm
Stewart's Restaurant & Convention Center
210 N. Bell School Road, Rockford
Stock Keeping Unit

Woodward, Inc. – Rock Cut Campus Tour
Friday, April 27 from 9:00 – 10:00 am.
1 Woodward Way, Loves Park
Stock Keeping Unit (Limited Availability)
Recognition and participation in RMM Aerospace Symposium is required to attend the tour.

The President's Aerospace Network (PAN) will sponsor the 2nd annual Aerospace Networking & Symposium event on Thursday, April 26th at Stewart's Restaurant & Convention Center, Rockford. The Engineers & Manufacturers will learn about the latest innovations happening in Aerospace.

Thursday, April 26

RMM Aerospace Symposium & Networking

2:30 – 2:10 pm

Welcome & Introductions

Hybrid Innovation

2:10 – 2:40 pm

Daniel Sasan, PE, PhD of Zunum Aero will speak about future-proofing hybrid electric aircraft.

Advanced Manufacturing Innovation

2:40 – 3:05 pm

Brandon Fabiano of Woodward discusses how robots and advanced materials are changing the world of manufacturing. Federico Scarmanella, PhD from MIT and Andrew Sobco, PhD from Quantek highlight Rapid Process Certification & Verification for High-Value-Added & Low Volume Production as a result of their work with DARPA. While understanding how to leverage the digital thread to quantify and certify OEM parts.

Networking

3:05 – 4:05 pm

Sponsor & Exhibitor Radio

4:05 – 4:15 pm

Boeing: Our Next Century of Aerospace Innovation

4:15 – 4:45 pm

Travis Sullivan discusses how Boeing is continuously inventing new products, process, and incorporates disruptive technology.

Additive Manufacturing Innovation

[illegible] – [illegible] pm

Advancements in Additive Manufacturing are changing everything from prototypes to final products. Electro Optical Systems, Stratasys, GE/TI, and 3D Platform discuss the intersection between with additive metals and manufacturing, highlighting the use of additive manufacturing to improve printing aircraft interiors for fly-away ready qualified parts, manufacturing slide tooling, and high-performance printing with CNC repeatability.

Networking

[illegible] – [illegible] pm

Representatives from GE Aviation, UTC Aerospace, and Woodward, Inc. will be present to connect with attendees interested in becoming suppliers to Tier-1 companies. Companies who have gone through the process of become suppliers will also be available to provide perspective and answer questions.

Speakers

Brandon Bohnens, Engineering Manager – Secondary Automated Line from Woodward, Inc.
Mark Fuller, Aerospace Segment Leader from Stratasys
John Pendleton from Electro Optical Systems
Roger Bannerman from GE/TI
Dr. Daniel M. Quinn, BS MSO, Chief Engineer from Sunny Jess
Dr. Fernando Gomez-Marello, PhD from NIA
Dr. Alkiviadis Kalaos, PhD from Chemnitz
Tanda Gulliver, VP Enterprise Strategy from Boeing

Friday, April 27th

Woodward, Inc. – Rock Cut Campus Tour

9:00 – 10:30 am

REGISTRATION IS CLOSED.

The deadline for registration has passed.

PLATINUM SPONSORS

GE Aviation UTC Aerospace Systems WOODWARD

GOLD SPONSORS

APA American Standard Circuits CHEM PROCESSING, INC. *Platings & Coatings for Industry*

---

* Speakers and topics subject to change without notice.

[illegible]

[illegible] – CELEBRATION OF MANUFACTURING EXCELLENCE

[illegible]

[illegible]

[illegible]

[illegible]

[illegible]

[illegible]

Sponsors

Presenting Sponsor

QPS

Gold Sponsor

FMA

Gold Sponsor

Gold Sponsor

WIPFLI

Manufacturing Awards Sponsor

United Way

Silver Sponsor

Thayer

Video Sponsor

Reinhart

[illegible]

[illegible]

[illegible]

[illegible]

[illegible]

[illegible]

Dinner Menu:

Garden Salad with Ranch Dressing

Fillet of Salmon with Salsa Sauce - Roasted wild mushrooms & black truffle cream gravy

Potatoes Au Gratin Boulanger

Lime Cheesecake

Vegetarian Option: Stuffed Acorn Squash Bowl - Quinoa Pilaf, Sage Brown Butter Sauce

Sponsors

Presenting Sponsor

QPS

(http://www.qpsmaintenance.com)

Gold Sponsor

FMA

(http://www.fmaonline.org)

Gold sponsor

ROCKFORD BANK & TRUST

(http://www.rdbandt.com)

Gold Sponsor

WIPFLi

(http://www.wipfli.com)

Silver Sponsor

Thayer

(http://www.thayerlighting.com)

Manufacturing Awards Sponsor

United Way

(http://www.unitedwayrk.org)

Video Sponsor

Reinhart

(http://www.reinhartfilms.com)

Leadership Rockford - 2018/2019
(http://web.rockfordchamber.com/events/eventdetail.asp?eventid=2069)
Jun 14, 2018

View All Events (http://web.rockfordchamber.com/events)

CHAIRMAN'S CLUB

FOX 39 WQRF 17 WTVO 23 WIFR 13 WREX SCHMELING CONSTRUCTION CO. Schmeling BUILDING ON PRINCIPLES SINCE 1903 NORTHE